

RIGOROUS ANALYSIS AND DESIGN OF DIFFRACTIVE OPTICAL ELEMENTS

by

JIANHUA JIANG

A DISSERTATION

**Submitted in partial fulfillment of the requirements
For the degree of Doctor of Philosophy in the
Optical Science and Engineering Program
Of
The School of Graduate Studies
Of
The University of Alabama in Huntsville**

HUNTSVILLE, ALABAMA

2000

Copyright by
Jianhua Jiang
All Rights Reserved
2000

DISSERTATION APPROVAL FORM

Submitted by Jianhua Jiang in partial fulfillment of the requirements for the degree of Doctor of Philosophy in Optical Science and Engineering.

Accepted on behalf of the Faculty of the School of Graduate Studies by the dissertation committee:

Committee Chair

Department Chair

College Dean

Graduate Dean

ABSTRACT
School of Graduate Studies
The University of Alabama in Huntsville

Degree Doctor of Philosophy College/Dept Optical Science and Engineering Program

Name of Candidate Jianhua Jiang

Title Rigorous Analysis and Design of Diffractive Optical Elements

Analysis and design of complex diffractive optical elements (DOE's) with rigorous electromagnetic diffraction models is very challenging because of the mathematical complexity of these models. In this dissertation, a novel rigorous analysis method for stacked rotated grating structures (SRGS's), the SRG-RCWA algorithm, is developed for the first time. It is based on a new implementation of the standard three-dimensional rigorous coupled-wave analysis (RCWA) algorithm that utilizes improved numerical techniques for better convergence and stability of the algorithm. The new concept of sampling frequency theory is developed to permit the 3-D RCWA algorithm to be applied to a particular class of SRGS's. The resultant SRG-RCWA algorithm has been successfully applied to the characterization of two fabricated SRGS's as circular polarization filters for an infrared imaging polarimetry system. The agreement between numerical SRG-RCWA results and experimental measurements demonstrates its validity and usefulness.

The second effort of this dissertation is to develop a rigorous design tool for finite aperture aperiodic DOE's (FADOE's) with feature size comparable to the optical wavelength. A micro-genetic algorithm (μ GA) is used for global optimization with a 2-D finite-difference time-domain (FDTD) method as the rigorous electromagnetic diffraction computations. With some latest FDTD techniques such as the perfect matched layer absorbing boundary conditions (PML

ACKNOWLEDGEMENTS

There are so many whose encouragement and support have made this work possible and to whom I owe thanks. First, I thank my advisor, Dr. Greg Nordin, for his invaluable and consistent guidance throughout this effort. Secondly, the other members of my committee have been helpful with comments and suggestions. I thank some graduate students, Steve Mellin, Lou Deguzman, Diana Chambers, and Jeff Meier, in the Diffractive Optics group for their enlightening conversations and collaboration.

Very special thanks go to my dear family, my wife Lixia and my lovely daughter Alice. Their endless patience and support made this happen. I thank also my parents who have always stressed the importance of high quality education.

TABLE OF CONTENTS

	Page
LIST OF FIGURES.....	ix
LIST OF TABLES	xiii
LIST OF SYMBOLS	xiv
Chapter 1 INTRODUCTION	1
1.1 Motivation.....	1
1.2 Overview of the dissertation	3
1.3 New contributions.....	5
Chapter 2 BACKGROUND	6
2.1 Refractive versus diffractive optics	6
2.2 Analysis methods for diffractive optics	8
2.3 Design methods for diffractive optics.....	15
Chapter 3 ANALYSIS OF STACKED ROTATED GRATING STRUCTURES	23
3.1 Stacked rotated grating structure as circular polarization filters.....	23
3.2 Three-dimensional RCWA algorithm.....	27
3.3 Adaptation to 3-D RCWA for analysis stacked rotated gratings (SRG-RCWA)	31
3.4 SRG-RCWA Performance analysis of two fabricated circular polarization filters	37
Chapter 4 RIGOROUS DIFFRACTION MODELS FOR FINITE APERIODIC DOE'S.....	45
4.1 Boundary element method (BEM).....	45
4.2 Finite element method (FEM).....	47
4.3 Finite-difference time-domain method (FDTD)	49
Chapter 5 OPTIMIZATION METHODS	74
5.1 Simulated annealing (SA).....	75
5.2 Genetic algorithms (GA's).....	76

Chapter 6 FORMULATION OF μ GA-FDTD RIGOROUS DESIGN TOOL FOR FADOE'S	90
6.1 Formulation of the μ GA-FDTD rigorous design tool.....	90
6.2 Test of the μ GA-FDTD on a diffractive microlens design	97
Chapter 7 FADOE DESIGN EXAMPLES AND APPLICATIONS	106
7.1 Design scenario.....	107
7.2 Focusing beam fanners	108
7.3 Novel multi-functional elements.....	122
Chapter 8 DISCUSSION AND CONCLUSIONS	128
8.1 Summary	128
8.2 Recommendations for future research	131
APPENDIX A: STANDARD THREE-DIMENSIONAL RIGOROUS COUPLED-WAVE ANALYSIS ALGORITHM FOR MULTI-LAYER TWO-DIMENSIONAL GRATING STRUCTURES	133
APPENDIX B: MATHEMATICAL MODIFICATIONS TO THREE-DIMENSIONAL RCWA ALGORITHM FOR SRG-RCWA ALGORITHM	150
REFERENCES.....	152

LIST OF FIGURES

Figure		Page
2.1	Ease of fabrication for DOE's by a) blazing and b) phase quantization process	8
2.2	Geometry of the scalar diffraction theory	9
2.3	Illustration of the general geometry for DOE design problems	15
2.4	Flowcharts of two optimization algorithms (a) bi-directional algorithm and (b) unidirectional algorithm	17
2.5	Illustration of the iterative Fourier transform algorithm (IFTA) for DOE design	20
3.1	Schematic illustration of the stacked rotated grating structure.....	24
3.2	Classic setup of a circular polarization filter	25
3.3	Three-dimensional RCWA algorithm convergence of the diffraction efficiency of reflected zero-th order as a function of the number of orders retained in one direction on an extreme thick metallic grating	31
3.4	Three-dimensional RCWA diffraction order lattice in Fourier space	32
3.5	Frequency sampling lattice of SRG-RCWA and three sample grating \vec{K} - vectors	33
3.6	Coordinate system of sandwich grating stack	35
3.7	Comparison of three algorithms on sandwich grating stack.....	36
3.8	SEM images of the cross sections of two SRG sample devices as circular polarization detectors (a) device 1 and (b) device 2.....	38
3.9	(a) Transmittance and (b) extinction ratio of SRGS sample device 1	43
3.10	(a) Transmittance and (b) extinction ratio of SRGS sample device 2	44
4.1	Geometry of boundary element method on analysis of DOE structures	46
4.2	Two-dimensional TE diffraction geometry for FEM method	48

4.3	General two-dimensional TE scattering geometry with FDTD sampling grid.....	52
4.4	Unit cell of Yee's FDTD algorithm for TE illumination.....	53
4.5	Space-time diagram of the Yee's algorithm for a one-dimensional wave propagation example showing the use of central differences for the space derivatives and leapfrog for the time derivatives	55
4.6	Implementation of Berenger PML ABC for two-dimensional FDTD algorithm in the TE case	61
4.7	FDTD total/scattered field formulation schematics	63
4.8	Field components in the two-dimensional TE lattice at or near the interface of total and scattered fields used for generating incident wave source.....	65
4.9	Geometry of the FDTD near-to-far field transformation algorithm for FADOE modeling.....	68
4.10	Schematic representation of FDTD geometry on FADOE analysis.....	70
4.11	Geometry of a dielectric circular cylinder scattering under TE illumination.....	72
4.12	Comparison between the FDTD and analytical results on a dielectric circular cylinder scattering problem.....	73
5.1	Structure of a typical simple conventional GA	86
5.2	Structure of a typical μ GA	86
5.3	2-D image plot of a modified De Jong F3 function.....	87
5.4	Comparison of binary and float encoding methods on the sample function with 100 variables.....	88
5.5	Comparison of three types of crossover operations for float encoding on the sample function with 100 variables.....	89
6.1	μ GA encoding geometry for FADOE's design.....	91

6.2	Sample of target and weighting function of μ GA for a microlens design (a) target function (exact desired intensity distribution on the observation plane) (b) weighting function.....	94
6.3	Pseudo-code of the μ GA-FDTD rigorous design tool for FADOE design.....	96
6.4	Analytically designed microlens (a) lens profile (b) intensity distribution on the local plane.....	98
6.5	Convergence curves of the μ GA-FDTD on a microlens design case (target function approach) (a) combination of arithmetical and heuristic crossover and (b) arithmetical crossover.....	101
6.6	Microlens optimized by μ GA-FDTD with target function approach (a) the analytical and μ GA optimized lens profiles and (b) their intensity distributions on the focal plane	102
6.7	Microlens optimized by μ GA-FDTD with weighting function approach (a) analytical and two optimized lens profiles and (b) their intensity distributions on the focal plane	104
6.8	Convergence curves of μ GA-FDTD with weighting function approach	105
7.1	Geometry for the numerical design examples	107
7.2	Two μ GA-FDTD optimized 1-to-2 beam fanners with 25 μ m peak separation	112
7.3	Two μ GA-FDTD optimized 1-to-2 beam fanners with 50 μ m peak separation	113
7.4	μ GA convergence curves for 1-to-2 beam fanner designs with different peak separations (a) 25 μ m and (b) 50 μ m	114
7.5	μ GA-FDTD optimized 1-to-2 beam fanners with 100 and 200 μ m peak separations using same maximum etch depth and minimum feature size as those of the 25 and 50 μ m peak separation cases.....	117

7.6	Two improved μ GA-FDTD optimized 1-to-2 beam fanners with 100 μm peak separation with deep etch depth	118
7.7	Improved μ GA-FDTD design for 1-to-2 beam fanners with 200 μm peak separation with deeper etch depth and smaller feature size (a) DOE profile and (b) the intensity distribution on the focal plane.....	119
7.8	μ GA-FDTD optimized 1-to-3 beam fanners with 50 μm peak separations (a) DOE profile and (b) its intensity distribution on the focal plane	121
7.9	Results of μ GA-FDTD design on a focusing 1-to-2 beam fanner/quarter-wave plate multi-functional FADOE element	124
7.10	A μ GA-FDTD optimized focusing TE/TM polarization beam splitter (a) DOE profile and (b) intensity distributions on the local plane	126
7.11	Two extinction ratio functions of the TE/TM polarization beam splitter.....	127
A.1	Geometry of three-dimensional RCWA algorithm for multi-layer stack with two-dimensional gratings and homogeneous layer in arbitrary order	136

LIST OF TABLES

Table		Page
3.1	Detail structural layer parameters of two SRG sample devices as circular polarization detectors	39
3.2	SRG-RCWA sampling frequencies and sampling numbers for simulation of two SRGS sample devices.....	40
3.3	Input elliptical polarization parameters to SRG-RCWA simulation.....	41

LIST OF SYMBOLS

<u>Symbol</u>	<u>Definition</u>
$\mathbf{a}_\ell, \mathbf{b}_\ell, \mathbf{F}_\ell, \mathbf{g}_\ell$	Matrices, representing subsets of matrix products
A	Aperture of the diffractive optical element on the object plane
$A_{\ell,gh}$	Amplitude of gh^{th} harmonic component of inverse permittivity
\mathbf{A}_ℓ	Inverse permittivity matrix constructed by $A_{\ell,gh}$
$B_i(x, z)$	Base functions of finite element method
\mathbf{B}	$\mathbf{K}_x \boldsymbol{\varepsilon}_\ell^{-1} \mathbf{K}_x - \mathbf{I}$
c	Speed of light
C	Geometry boundary of the DOE
C^∞	Integration boundary in the infinity
$c_{\ell,i}^+, c_{\ell,i}^-$	Unknown constants to be calculated
$\mathbf{C}_\ell^+, \mathbf{C}_\ell^-$	Matrices of unknown constants
C_{pq}	Expanding coefficients of the phase function
CER	Circular extinction ratio
d_ℓ	Thickness of ℓ^{th} layer (along z) in a grating stack
$d(x, y)$	Local grating period of DOE's
DE_r, DE_t	Diffraction efficiency of reflected/transmitted diffraction order
\mathbf{e}	Matrix of electric field values on the sample points
E	Electric field amplitude
\vec{E}	Electric field vector

\vec{E}_{inc}	Electric field vector incident on SVDOE
$E_{\text{I}}, E_{\text{III}}$	Electric field amplitude in Region I/Region III
$\vec{E}_{\text{I}}, \vec{E}_{\text{III}}$	Electric field vector in Region I/Region III
f_{sx}	Sampling frequencies of SRG-RCWA for x-axis
f_{sy}	Sampling frequencies of SRG-RCWA for y-axis
F_i	Fitness value of an individual
$F(\mathbf{k})$	Spatial Fourier transform of a function
g	Index of spatial harmonics in x-direction
\mathbf{G}_ℓ	Diagonal matrix with elements $\exp(-k_0\gamma d)$
h	Index of spatial harmonics in y-direction
$h(x, y, z)$	Impulse response function of the scalar field propagation process
H	Magnetic field amplitude
\vec{H}	Magnetic field vector
$H(k_x, k_y, z)$	Propagation kernel of the scalar field propagation processes
i	Integer number
I	Intensity constraint terms of the fitness function
\mathbf{I}	Identity matrix
j	Square root of negative one
k	Propagation number in a medium
\vec{K}	Grating vector
k_0	Free space wave number
k_{I}	Wavevector of wave in the incident media of a grating stack
k_{III}	Wavevector of wave in the exit medium of a grating stack

$k_{I,zmn}, k_{III,zmn}$	Wavevector of mn-th diffracted order in Region I/Region III, z-component
$\mathbf{K}_I, \mathbf{K}_{III}$	Diagonal matrices with diagonal elements of $k_{I,zmn}, k_{III,zmn}$
k_x	Wavevector x-component
k_{xm}	Wavevector of mn-th diffracted order, x-component
\mathbf{K}_x	Diagonal matrix with diagonal elements of k_{xm}/k_0
k_{yn}	Wavevector of mn-th diffracted order, y-component
\mathbf{K}_y	Diagonal matrix with diagonal elements of k_{yn}/k_0
k_z	Wavevector z-component
ℓ	Designation for layer number
m	Integer number
M	Integer number
\mathbf{M}	System matrix of finite element method
n	Refractive index of a medium
\hat{n}	Normal direction of a surface
N	Integer number
n_x	Sampling number in x-axis
n_y	Sampling number in y-axis
n_I	Refractive index in incident region
n_{III}	Refractive index in exit region
$O[]$	Higher order terms in the Taylor expansion
p	Integer number
P	Phase constraint terms of the fitness function

$P()$	Probability distribution function
q	Integer number
r	Position distance between the source and the observation points
R	Radial distance from the coordinate origin
\vec{R}_{mn}	Electric field of mn-th reflected diffracted wave
\mathbf{R}	Vector with elements \vec{R}_{mn}
\mathbf{R}_x	Vector with elements R_{xmn}
\mathbf{R}_y	Vector with elements R_{ymn}
$\text{Re}\{\}$	Real part of an imaginary number
$S_{\ell,xmn}, S_{\ell,ymn}, S_{\ell,zmn}$	Amplitude of space harmonics of electric field
$\mathbf{S}_{\ell,x}$	Vector with components of $S_{\ell,xmn}$
$\mathbf{S}_{\ell,y}$	Vector with components of $S_{\ell,ymn}$
S_z	Z-component of the complex Poynting vector
t	Time variable
\hat{t}	Tangential direction of a surface
t_{\max}	Maximum thickness of a diffractive optical element
\vec{T}_{mn}	Electric field of mm-th transmitted diffracted wave
\mathbf{T}	Matrix with elements T_i
\mathbf{T}^{-1}	Inverse propagation operator
TM	Transverse magnetic field polarization mode
TE	Transverse electric field polarization mode
\hat{u}	Unit vector giving electric field direction

u_x, u_y, u_z	Components of vector \hat{u}
U	Uniformity constraint terms of the fitness function
$u(x, y, z)$	Complex amplitude field distribution in $Z=z$ plane
$U(k_x, k_y, z)$	Fourier transform of $u(x, y, z)$
$U_{\ell, xmn}, U_{\ell, ymn}, U_{\ell, zmn}$	Amplitude of space harmonics of magnetic field
$\mathbf{U}_{\ell, x}$	Vector with components of $U_{\ell, xmn}$
$\mathbf{U}_{\ell, y}$	Vector with components of $U_{\ell, ymn}$
$\mathbf{V}_{\ell, i}$	Matrices representing products and sums of eigenvalues/eigenvectors
W	Width of a FADOE
\mathbf{W}	Signal window on the observation plane
$W(x)$	Weighting function
$\mathbf{W}_{\ell, i}$	Eigenvector matrices
$w_{\ell, i, mn}$	Elements of eigenvector matrices $\mathbf{W}_{\ell, i}$
x	Rectangular coordinate axis (x-axis)
\bar{x}	Individuals of a GA population
$\mathbf{X}_{\ell, i}$	Diagonal matrix with elements $\exp(-k_0 \sigma_{\ell, i} (z - Z_\ell))$
$\mathbf{X}'_{\ell, i}$	Diagonal matrix with elements $\exp(-k_0 \gamma_{\ell, i} (z - Z_\ell))$
y	Rectangular coordinate axis (y-axis)
z	Rectangular coordinate axis (z-axis)
Z_i	Etch depth at center of each cell location
Z_{II}	Diagonal matrix with elements $k_{II, zi} / (k_0 n_{II}^2)$
Z_L	Total thickness of a grating stack

α	Profile parameter for SRG-RCWA
β	Orientation angle of the grating vector
$\gamma_{\ell, mn}$	Z-component of wavevector of mn-th order in a homogeneous layer
δ	Thickness of a PML region
$\delta_{i,0}$	Kronecker delta function
ΔE	Change of the objective function
Δx	Sampling step of FDTD in x-direction
Δz	Sampling step of FDTD in z-direction
Δt	Sampling time interval of FDTD
ε	Permittivity of a medium
ε_0	Permittivity of free space
$\varepsilon_{\ell, gh}$	Amplitude of gh^{th} harmonic component of permittivity modulation
$\mathbf{\varepsilon}_{\ell}$	Permittivity matrix constructed by $\varepsilon_{\ell, gh}$
σ	Electrical conductivity of a material
σ^*	Magnetic loss of a material
$\sigma_{\ell, i}$	Positive square roots of the eigenvalues
Σ	Diagonal matrix with diagonal elements of $\sigma_{\ell, i}$
θ	Incidence angle of wave on DOE
λ	Wavelength
λ_0	Freespace wavelength
Λ	Grating period
ρ	Depth of a PML region
μ_0	Permeability of free space

π	Physical constant pi
φ	Azimuthal angle of wave incident on gratings
$\Phi(x, y)$	Phase function of DOE's
ψ	Polarization angle
ω	Angular optical frequency
Ω	Computational domain of finite element method (FEM)
$\partial\Omega$	Outer boundary of the computational domain of FEM
**	Convolution operation

Chapter 1

INTRODUCTION

1.1 Motivation

There is a consistent trend towards miniaturization and integration of components and systems in many fields of engineering, in order to significantly reduce the size, weight, power consumption and cost. This trend is particularly apparent in optics, where recent years have seen rapid growth in such new or renewed fields as microoptics [1], integrated optics [2] and micro-opto-electro-mechanical systems (MOEMS) [3]. In each of these areas, diffractive optics plays an important role. With advances in micro-fabrication technologies, diffractive optical elements (DOE's) can be made very compact, lightweight and inexpensive, which is ideal to miniaturize and integrate conventional optical systems.

The grating period or feature size of today's DOE's has been continually decreasing. When the feature size of DOE's is of the order of or less than the optical wavelength, the classical scalar diffraction theory is no longer valid and cannot be applied to the analysis and design of such elements. In general, rigorous electromagnetic diffraction models must be used to accurately predict the performance of such DOE's. Rigorous diffraction models solve Maxwell's Equations without arbitrary approximations, which generally involve complex mathematical manipulations and hence are very challenging.

As discussed by Deguzman [4], there are a variety of applications for which stacked rotated grating structures (SRGS's) are highly attractive, which consist of multiple one-

dimensional grating layers with different grating periods and orientations. Since the different grating layers can perform different functions, it is expected that SRGS's should have many potential applications in component and system integrations. Also, recent experiments [5], [6] have demonstrated that SRGS's can be constructed as photonic crystals, which is an interesting field to many researchers. However, these applications haven't been fully explored because of the lack of rigorous diffraction models for SRGS's. In this dissertation, a novel rigorous coupled-wave analysis (RCWA) algorithm [7], [8], the SRG-RCWA algorithm, is developed to address the diffraction problem associated with SRGS's. The SRG-RCWA is based on the standard three-dimensional RCWA algorithm and employs a new concept, sampling frequency theory. Two simple SRGS's designed to function as circular polarization filters and fabricated by Deguzman [4] have been successfully characterized by it.

On the other hand, it is now also feasible to fabricate finite aperture aperiodic DOE's (FADOE's) with feature size comparable to the optical wavelength. The rigorous electromagnetic models [9], [10], [11] for FADOE's are much more complicated than those for infinite periodic gratings [12]. The crucial point in rigorous analysis and design of FADOE is to make the diffraction models as efficient as possible. In this dissertation, an efficient two-dimensional finite-difference time-domain (FDTD) [13] algorithm has been implemented with the latest improvements in FDTD algorithms. For physically symmetric DOE design problems, i.e., the required DOE profiles are symmetric with normal illuminations, the FDTD algorithm can be applied to only half of the DOE profile so that FDTD computation is reduced to half.

Global optimization of DOE's is also a challenging task because the solution space has a lot of structures, i.e., many local minima and maxima (multi-modal solution space). Although genetic algorithms (GA's) [14] are very powerful and well suited for such complex problems, the large population size of the conventional GA's results in prohibitive computational load even for modern workstations. This difficulty is avoided in this dissertation by utilizing an advanced genetic algorithm, the micro-GA (μ GA) [15], in which a small population size is used. In

conjunction with the two-dimensional FDTD algorithm, a rigorous design tool, the μ GA-FDTD, has been developed and some FADOE elements have been designed and optimized.

1.2 Overview of the dissertation

This dissertation is organized as follows. Chapter 2 provides background information about diffractive optics. First, the diffractive optics are compared to the refractive optics. Then both classical scalar diffraction theory and various rigorous diffraction methods for gratings are reviewed. This is followed by the review of various DOE design methods.

Chapter 3 focuses on the rigorous analysis of SRGS's. The physical structure of SRGS's is first introduced with a specific application, a circular polarization filter for an infrared imaging polarimetry system. The difficulty of applying standard RCWA algorithm to the diffraction of SRGS's is then analyzed. From this analysis, a novel RCWA algorithm, the SRG-RCWA, is proposed. Since the SRG-RCWA is based on the standard three-dimensional RCWA algorithm, a new implementation of the standard three-dimensional RCWA with some improved numerical techniques is presented. Then it is adapted to the SRG-RCWA through the concept of sampling frequency. Finally, measurements from two fabricated SRGS's are compared to SRG-RCWA results.

In Chapters 4 through 7, we develop a unidirectional rigorous design tool for FADOE's. This involves two major tasks: (1) developing a rigorous diffraction model for FADOE's, by which the performance of the FADOE's can be evaluated; and (2) implementing a global optimization method so that optimum designs can be achieved.

Chapter 4 is dedicated to the rigorous modeling of FADOE's. Through the review and comparison of several available models, the FDTD method is selected as the rigorous diffraction model for FADOE's. The detailed FDTD algorithms are then thoroughly discussed with some modifications to accommodate the unique features of one-dimensional FADOE's. The FDTD

implementation is validated by the scattering of a two-dimensional dielectric cylinder for which there is a known analytical solution.

Chapter 5 focuses on genetic algorithms, which serves as the global optimization method in the FADOE design tool. Basic concepts and salient features of GA's are first introduced followed by a detailed illustration of some basic genetic operators. The structures of different GA's, namely the conventional GA and μ GA, are presented in forms of pseudo-code. Also in this chapter, another commonly used optimization method, simulated annealing, is briefly reviewed for the sake of completeness.

After the completeness of FDTD and μ GA, the desired rigorous FADOE design tool can be developed by coupling them through the re-formulation of μ GA particularly for the FADOE design geometry, which is discussed in Chapter 6. A simple encoding method for one-dimensional FADOE's is first established. A sophisticated fitness function is constructed so that multiple design constraints can be imposed on both intensity and phase distributions and their uniformities in the observation plane. Then the overall structure of the μ GA-FDTD rigorous design tool is illustrated. The performance of the design tool is tested on a microlens design case with two different constraint approaches: the target function and weighting function approaches.

Numerical FADOE design examples of μ GA-FDTD are presented in Chapter 7, where some common FADOE elements such as 1-to-2 and 1-to-3 beam fanners are optimized and compared. Additionally, two novel multi-functional elements, a focusing 1-to-2 beam fanner/Quarter-wave plate and a focusing TE/TM polarization beam splitter have also been designed.

The dissertation is summarized in Chapter 8 with some recommendations for future research.

1.3 New contributions

Major new work that is presented in this dissertation is in the following list:

1. Extension of Moharam's enhanced transmittance matrix method for one-dimensional gratings [16] to the two-dimensional grating case.
2. Development of the SRG-RCWA for rigorously analyzing diffraction from SRGS's using the sampling frequency concept.
3. Development of the rigorous design tool μ GA-FDTD for the design of FADOE's.
4. Implementation of a 'creeping' operator to enhance the local search capability of μ GA.
5. Design of some multi-functional FADOE elements.

Chapter 2

BACKGROUND

Diffractive optics has been proven to be a viable technology for a wide variety of applications. In this chapter, the advantages of diffractive optics are first illustrated with the comparison of traditional refractive optics. Brief reviews on both analysis and design methods of diffractive optics are then presented, which establishes the research stage of the dissertation. The review starts from the re-derivation of the classical scalar diffraction theory with Fourier transformation and linear system approaches. A short historical review of the rigorous electromagnetic theory on diffraction gratings follows, in which some popular diffraction methods are compared. Also, the basic concepts of DOE design are introduced and various design methods are reviewed.

2.1 Refractive versus diffractive optics

The use of refractive optical elements (ROE's), such as lenses and prisms, dominates the history of optics, while the use of diffractive optical elements (DOE's), mainly gratings, has a relatively short history (about two centuries) and is only for specific applications (mostly in spectroscopy). However, as claimed by George R. Harrison, "No single tool has contributed more to the progress of modern physics than the diffraction grating." the diffraction grating has been the best-established diffractive optical element and may be regarded as the equivalent of the prism in function of spectral dispersion but is far superior to prism in many important regions of the spectrum. Diffraction grating is the basis of the majority of spectroscopic analysis which has

had very profound influence on modern science and technology. In recent decades, great advances in fabrication technologies, especially optical microlithography [17], and computer modeling techniques have led to an explosion of applications of diffraction in optics, which makes diffraction optics one of the most rapidly advancing areas of current research in optics. Not only the gratings are now found to be useful in many non-spectroscopic fields such as ultra-fast optics [18], optical photolithography [19], optical communications [20], but also new kinds of diffractive optical elements like finite aperture and aperiodic DOE's [21] are emerging and finding their places in various industrial applications [22]. It is for these reasons that so much effort has been devoted to the analysis, design and fabrication of gratings and other non-conventional DOE's, some of which will be briefly reviewed in Section 2.2 and Section 2.3.

Since the light is manipulated by analog surface in ROE's, considerable thickness (compared to the optical wavelength) is therefore necessary to implement them, even for microoptical ROE's. The required smooth surface quality and amount of thickness make it very challenging or impractical to fabricate microoptical ROE's with microlithography technologies. However, In DOE's the thickness can be significantly reduced by so-called blazing process [23], which is based on the periodic nature of the electromagnetic wave that there is no difference between a 2π and a $N \cdot 2\pi$ phase delay. For example, as shown in Figure 2.1(a) the maximum thickness of a microlens can be reduced to $t_{\max} = \lambda_0 / (n - 1)$, where n denotes the refractive index of the substrate. For a wavelength $\lambda_0 = 633$ nm and a fused silica glass substrate ($n = 1.457$), the maximum thickness t_{\max} is about 1.4 μm , which is readily fabricated with standard lithographic techniques. The fabrication task for DOE's can be further eased by the phase quantization of continuous phase profile (Figure 2.1(b)). By quantization, the continuous phase profile can be replaced by a set of features of small lateral extension which is periodically replicated. Such a multi-phase level DOE profile can be fabricated by a series of same microlithography process. As soon as a microlithography process is developed, the DOE profile

can be put into massive production with a very low cost. Because of their ease of replication, DOE's can offer significant technological and economic advantages over ROE's.

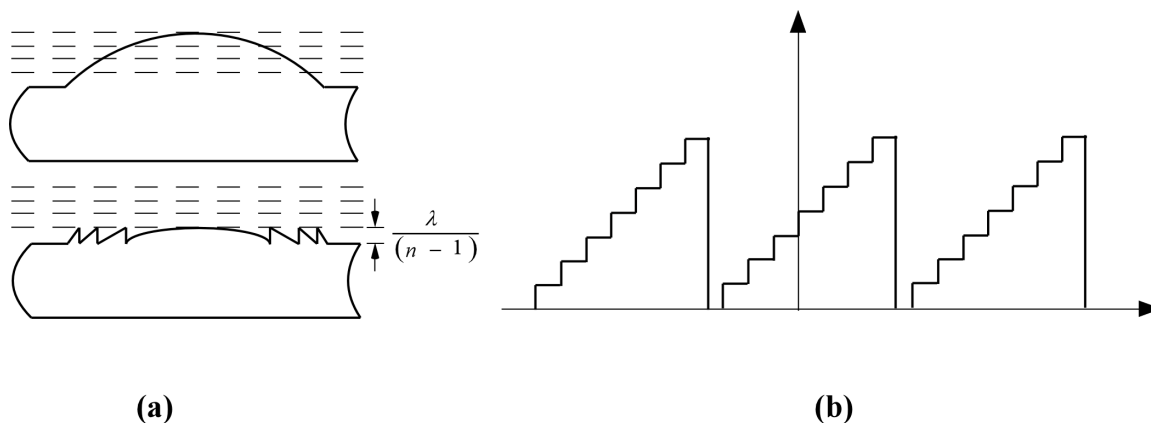


Figure 2.1 Ease of fabrication for DOE's by a) blazing and b) phase quantization process

2.2 Analysis methods for diffractive optics

The analysis of diffractive optical elements has achieved a stage of maturity. Many models and algorithms have been developed. Scalar diffraction theory [24] is valid for a large variety of diffractive elements and is mathematically efficient so that it is the most widely used diffraction theory. Some important scalar diffraction models are reviewed in Section 2.2.1. However, rigorous diffraction algorithms are necessary to accurately predict the performance of diffractive optics with feature size comparable to the optical wavelength. In Section 2.2.2, various rigorous diffraction algorithms for gratings with infinite extent are briefly compared without

going into mathematical details. Rigorous diffraction algorithms for finite aperture DOE's are discussed in Chapter 4.

2.2.1 Scalar diffraction theory

In scalar diffraction theory, the vector characteristic of electromagnetic field is ignored so that the wave field can be treated as a scalar field. As shown in Figure 2.2, the function of the DOE structure is modeled by a transfer function and the field distribution just after the DOE (object plane) can be expressed by its complex amplitude $u(x, y, 0)$.

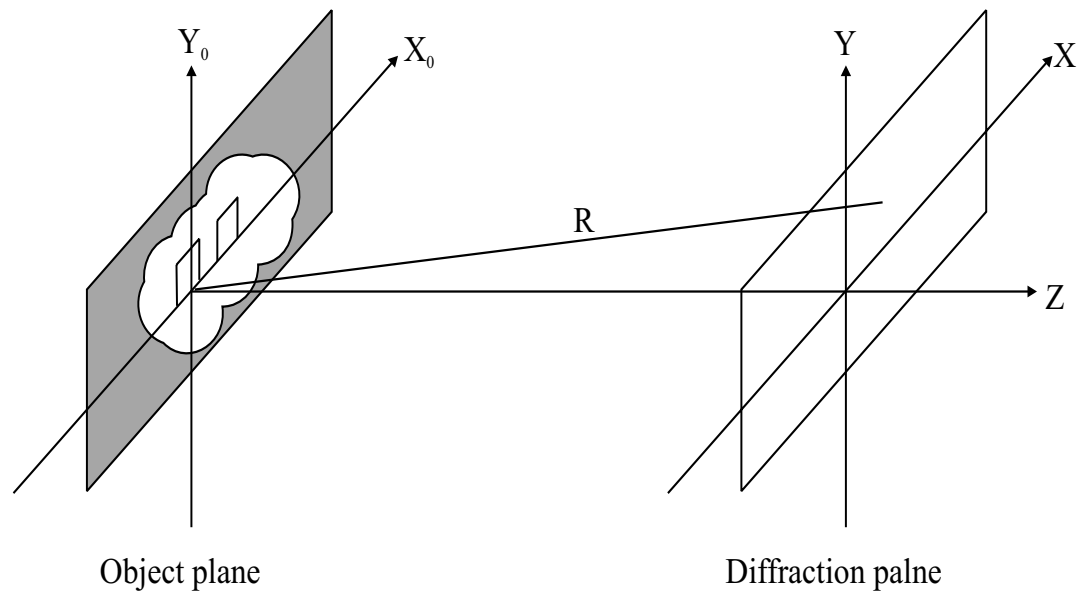


Figure 2.2 Geometry of the scalar diffraction theory

The field propagation in free space from object plane to diffraction plane is governed by the scalar Helmholtz equation

$$\nabla^2 u(x, y, z) + k_0^2 u(x, y, z) = 0. \quad (2.1)$$

in which k_0 is the free space wave number. It is well known that the field can be decomposed into its plane wave spectrum by means of a Fourier transformation [24], [25]

$$u(x, y, z) = \iint U(k_x, k_y, z) \exp(j(k_x x + k_y y + k_z z)) dk_x dk_y, \quad (2.2)$$

in which k_x , k_y , and k_z denote the wave vector components of the plane wave. Substituting Equation 2.2 into Equation 2.1, one can derive a differential equation for $U(k_x, k_y, z)$

$$\frac{\partial^2 U(k_x, k_y, z)}{\partial z^2} + k_0^2 \left[1 - \frac{(k_x^2 + k_y^2)}{k_0^2} \right] U(k_x, k_y, z) = 0. \quad (2.3)$$

This differential equation can be easily solved and a general equation for light propagation in free space can be obtained

$$U(k_x, k_y, z) = U(k_x, k_y, 0) \exp\left(-jk_0 z \sqrt{1 - \frac{(k_x^2 + k_y^2)}{k_0^2}}\right), \quad (2.4)$$

in which $U(k_x, k_y, 0)$ is the Fourier transform of $u(x, y, 0)$. It is evident from Equation 2.4 that the field propagation process can be treated as a linear system with a systemic transfer function

$$H(k_x, k_y, z) = \exp\left(-jk_0 z \sqrt{1 - \frac{(k_x^2 + k_y^2)}{k_0^2}}\right). \quad (2.5)$$

This equation is also known as forward propagation kernel for both propagating and evanescent components of the plane wave spectrum of the field. Propagating components are spectrum modes with

$$k_x^2 + k_y^2 < k_0^2, \quad (2.6)$$

whereas evanescent components are given by

$$k_x^2 + k_y^2 \geq k_0^2. \quad (2.7)$$

One of the important features of the propagation kernel approach is that it is easy to adapt to back propagation of the field and back propagation kernel is simply the phase conjugate of the forward propagation kernel

$$H(k_x, k_y, z) = \exp\left(jk_0 z \sqrt{1 - (k_x^2 + k_y^2)/k_0^2}\right). \quad (2.8)$$

Equation 2.5 and Equation 2.8 are foundations of the most iterative DOE design algorithms in scalar domain, which will be reviewed in Section 2.3.

With the definition of transfer function (or propagation kernel) as Equation 2.5, Equation 2.4 can be rewritten as

$$U(k_x, k_y, z) = U(k_x, k_y, 0)H(k_x, k_y, z). \quad (2.9)$$

To get the field distribution on the diffraction plane $u(x, y, z)$, the transfer function of Equation 2.5 must be inverse Fourier transformed to get the impulse response function for the field propagation process. This inverse Fourier transform is difficult. However, Lalor [26] analytically proved that the impulse response function should be

$$h(x, y, z) = \frac{1}{2\pi} \frac{\exp(-jk_0 R)}{R} \frac{z}{R} \left(jk_0 + \frac{1}{R} \right), \quad (2.10)$$

in which $R = \sqrt{x^2 + y^2 + z^2}$. Now the field distribution $u(x, y, z)$ can be expressed as a convolution operation

$$\begin{aligned} u(x, y, z) &= u(x, y, 0) ** h(x, y, z) \\ &= \frac{1}{2\pi} \iint_{\mathbf{s}} u(x_0, y_0, 0) \frac{\exp(-jk_0 r)}{r} \frac{z}{r} \left(jk_0 + \frac{1}{r} \right) dx_0 dy_0, \end{aligned} \quad (2.11)$$

in which $r = \sqrt{(x - x_0)^2 + (y - y_0)^2 + z^2}$ and the region of the integration is over the source area in the $x_0 y_0$ plane. This integral is known as the famous Rayleigh Sommerfeld diffraction formula, which is the exact in scalar domain and is valid for any region $z > 0$.

Rayleigh Sommerfeld diffraction formula can be approximated to describe the two most familiar formulas in scalar diffraction theory. First Fresnel diffraction formula for near field diffraction can be derived by paraxial approximation of Equation 2.5. If

$$(k_x^2 + k_y^2)/k_0^2 \ll 1, \quad (2.12)$$

then Equation 2.5 can be approximated by

$$H(k_x, k_y, z) = \exp\left(-jk_0 z \left(1 - \frac{k_x^2 + k_y^2}{2k_0^2}\right)\right). \quad (2.13)$$

Inverse Fourier transform Equation 2.13 to get impulse response function for Fresnel diffraction:

$$h(x, y, z) = \frac{jk_0}{2\pi z} \exp(-jk_0 z) \exp\left(-jk_0 \frac{x^2 + y^2}{2z}\right), \quad (2.14)$$

and the field distribution on diffraction plane can be written as

$$u(x, y, z) = \frac{jk_0 \exp(-jk_0 z)}{2\pi z} \times \iint_s u(x_0, y_0, 0) \exp\left(\frac{-jk_0}{2z} [(x-x_0)^2 + (y-y_0)^2]\right) dx_0 dy_0. \quad (2.15)$$

This is known as Fresnel diffraction formula.

For the far field diffraction in the sense that

$$z \gg \frac{1}{2} k_0 (x_0^2 + y_0^2)_{\max} \quad (2.16)$$

is valid, Fresnel diffraction formula can be further simplified as

$$u(x, y, z) = \frac{jk_0 \exp(-jk_0 z)}{2\pi z} \cdot \exp\left(\frac{-jk_0 (x^2 + y^2)}{2z}\right) \times \iint_s u(x_0, y_0, 0) \exp\left(\frac{jk_0}{z} (xx_0 + yy_0)\right) dx_0 dy_0. \quad (2.17)$$

Equation 2.17 is known as the Fraunhofer diffraction formula, which relates the diffracted field to the input field by a simple Fourier transformation.

2.2.2 Rigorous diffraction theory for gratings

In rigorous diffraction theory, the vector nature of the electromagnetic field must be considered by exactly solving Maxwell's Equations or vector wave equations without any deliberate approximations as in scalar theory. Unfortunately it is impossible to obtain a general analytical solution to the diffraction problems for all kinds of gratings. Therefore researchers focus on numerical solutions. Due to the diversity of grating types, there is no single numerical method that can be used for all gratings. However, for any specific type of grating, there is at least one numerical method available that can provide satisfactory solutions. In general, according to which form of Maxwell's Equations they are based on, rigorous grating models can be grouped into two major categories: integral approaches and differential approaches. To avoid tedious mathematical derivations associated with all rigorous grating models, only a brief historical review and a comparison of some of the most widely used models are presented. The purpose is to provide an overall picture of the development and status of the rigorous numerical modeling of gratings.

Historically, the development of the rigorous diffraction theory of gratings can be divided into three stages. The first stage spanned from the early 1960s to the late 1970s, in which the electromagnetic theory of gratings was established. Two of the most basic rigorous numerical methods for gratings, the integral method [27] and the differential method [28], were developed during this period. These two methods, while accurate and elegant, are difficult to intuitively interpret and to implement. Both rely on complicated numerical algorithms. An excellent reference to these methods is available in textbook form [29].

The second stage of the development occupied the years between the late 1970s and early 1990s. It featured the development of new numerical methods and expanding their realm of application. In fact, most of the presently existing methods had been known by the end of this stage. The achievements of this stage are collected in a volume of the SPIE milestone series [30].

The last stage of the rigorous grating theory started in the early 1990, and continues today. The main focus of the research in this stage is to improve the existing methods in areas of numerical stability and convergence speed.

Although there are presently more than a dozen rigorous numerical methods for different types of gratings, rigorous coupled wave analysis (RCWA) [7], [8], [31], [32], [33] and the modal method [34], [35] are the two that are most widely used. It has been shown that these two approaches are totally equivalent in their full rigorous form [36]. They both rely on Fourier expansion of the permittivity of the grating medium, but differ in the expansion of the electrical field in the grating medium. Associated with each expansion is a different physical perspective of the total field of the grating.

RCWA was first formulated by Moharam and Gaylord for planar gratings and then extended to surface relief gratings and crossed-gratings. In RCWA, the field inside the grating medium is expanded in terms of the space harmonic components of the field in the periodic structure. These space harmonics inside the grating are phase matched to diffracted orders outside of the grating. The individual space-harmonic fields do not satisfy the vector wave equation (and thus Maxwell's Equations). But the sum of all space harmonic fields, of course, satisfies the wave equations. However, in the modal method, the fields inside the gratings are expanded in terms of the allowable modes of the periodic medium. The fields can be visualized as waveguide modes in the grating region. The total electric field is expressed as a weighted summation over all possible modes. In contrast to RCWA, each mode does satisfy the wave equation by itself and each mode consists of an infinite number of space harmonics.

Though RCWA and the modal method are equivalent in nature and are closely related, the RCWA method has two advantages compared to the modal method. First, the mathematical background required is much less demanding. Most math libraries and software packages such as LINPACK and MATLAB contain the necessary linear algebra algorithms. Second, RCWA gives diffraction results in terms of the diffraction efficiency of each order, which is the standard form

of analytical theory. The modal method expresses the results in terms of the electric field mode coefficients. To get the diffraction efficiency of the different orders, further calculations are needed.

2.3 Design methods for diffractive optics

2.3.1 Basics of DOE design problem

Figure 2.3 illustrates general design geometry for diffractive optics. A is the aperture of the diffractive optical element on the object plane. W , the signal window, is the area on the observation plane where at least some properties of the optical field must be realized in order to achieve desired DOE function for specific applications. For example, in focusing problems W is a single focal point; in 2-D array illumination W is a rectangular region in which $N \times N$ uniform spots in a regular 2-D grid must be generated; in beam shaping applications W is a bounded region in which a certain intensity distribution of the diffracted field is required.

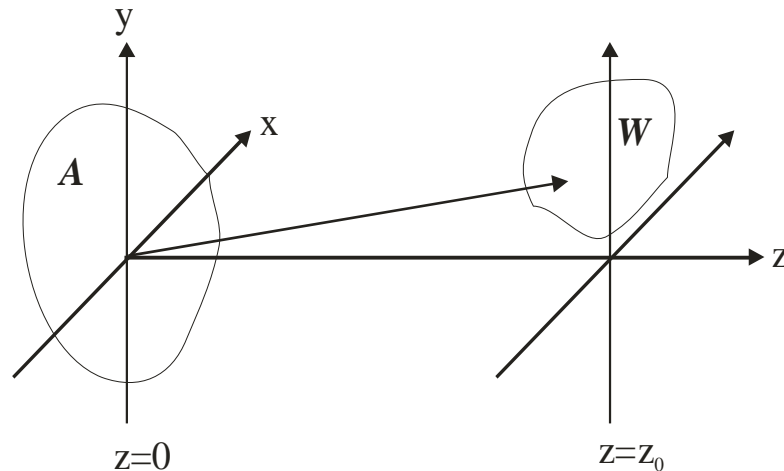


Figure 2.3 Illustration of the general geometry for DOE design problems

The basic design problem in diffractive optics is to find a DOE structure in aperture A that can generate, in the signal window W , a field that approximates the field specified by the particular application. One of the basic tasks in the design of diffractive elements is to ensure that a significant fraction of the incident power within A ends up inside W , though noise may be allowed to appear outside it. This fraction is known as the diffraction efficiency of the DOE, which is an important parameter for evaluating the performance of the DOE.

To attempt a mathematical solution of the design problem, we must have two things: an analysis scheme to relate the incident field at A to the diffracted field in W , and an optimization method to find a suitable DOE profile. Generally the diffraction design methods can be classified into two groups [37]: direct design or indirect design. Direct designs are those that try to optimize the desired DOE performance directly, within the constraints of fabrication. In contrast, indirect methods are those that first seek to find a best solution without fabrication constraints and then impose the constraints of fabrication onto the unconstrained solution.

In general, the design procedure of DOE's can be divided into three basic stages [37]. The first stage is the analysis of the DOE design problem, in which the designer must understand the physics of the function of the DOE and the required fabrication process. Also, one must select models both for the DOE and the fabrication process. The choice of diffraction analysis model affects not only the complexity of the design algorithm but also the definition of the performance measure. In selecting a fabrication model, the designer should address how much detail of fabrication to be included.

The second design stage is synthesis, the main task of which is to translate the physical understanding of the problem and to define an appropriate optimization problem. By doing so, it actually casts the design problem into an optimization problem. Based on the physical parameters that determine the performance of the DOE, some design metric (a measure of the performance of DOE) is defined. The design metric may be expressed in terms of physical parameters such as diffraction efficiency.

The third stage of DOE design is implementation so that the design is carried out and the optimized element is fabricated. In this stage, an optimization algorithm must be selected. Two kinds of algorithms are available in the literature: unidirectional or bi-directional. Examples of the former one are gradient search [38], simulated annealing [39], genetic algorithm [14] and one example of the latter is iterative Fourier transform-based algorithms [40]. In the unidirectional algorithm, the field distribution in the desired observation plane is not used explicitly to calculate the new object after each iteration of optimization. However, in the bi-directional algorithm, the observation plane field distribution is employed to calculate the object after each optimization. The flowcharts of these two kinds of algorithm are shown in Figure 2.4.

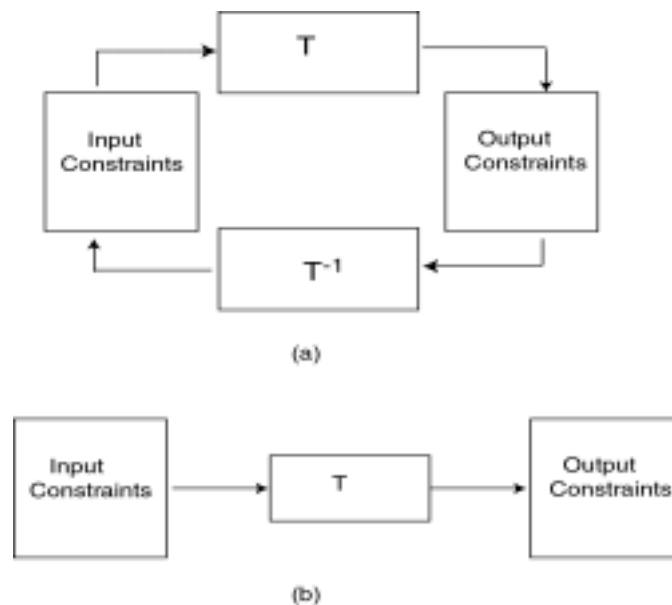


Figure 2.4 Flowcharts of two optimization algorithms (a) bi-directional algorithm and (b) unidirectional algorithm

2.3.2 Design methods based on geometric optics

It seems strange that the design of diffractive optical elements can be accomplished by techniques based on geometrical optics because the effect of diffraction is totally ignored in geometrical optics. In fact, geometrical optics based design methods are very efficient tools and are widely used in designing simple diffractive elements such as diffractive microlenses. Almost all major optical design programs familiar to optical engineers have the capability of ray-tracing analysis for diffractive optical elements.

Ray-tracing through diffractive elements [12] is based on local use of the grating equation, where the local grating period of any (modulo $N \times 2\pi$) diffractive element with a smoothly varying phase function is given by

$$d(x, y) = 2\pi N \left| \nabla \Phi(x, y) \right|^{-1}. \quad (2.18)$$

The diffractive ray-tracing equations take the form [41]

$$n_2 \sin \theta_{m,x} = n_1 \sin \theta_x - \frac{m}{k} \frac{\partial}{\partial x} \Phi(x, y), \quad (2.19)$$

$$n_2 \sin \theta_{m,y} = n_1 \sin \theta_y - \frac{m}{k} \frac{\partial}{\partial y} \Phi(x, y), \quad (2.20)$$

in which θ_x and θ_y are the propagation angles of the incident ray with respect to x and y axes and $\theta_{m,x}$ and $\theta_{m,y}$ denote the corresponding angles associated with the m th-order diffracted ray.

Ray-tracing-based optimization of systems that consist of diffractive optical elements is quite similar to the optimization of conventional refractive lens systems. First the phase function of the diffractive element $\Phi(x, y)$ is expanded into a power series

$$\Phi(x, y) = k \sum_p \sum_q C_{pq} x^p y^q, \quad (2.21)$$

in which C_{pq} are the free coefficients that will be optimized. Then one of the standard lens system optimization methods, such as the damped least-square method or simulated annealing, is employed to minimize the system merit function.

2.3.3 Iterative design methods based on scalar theory

In addition to the geometrical optics approaches, scalar theory based iterative DOE design methods [42] are also very popular, among which the most successful and the most widely used DOE design algorithm is the iterative Fourier transform algorithm (IFTA) [43] for the far-field diffraction problems.

Historically, IFTA was initiated by Gerchberg and Saxton [44] and was designed for the solution of image phase retrieval problems. Essentially the same method was discovered independently by Gallagher and Liu [45] and was applied to the design of phase only DOE's for the first time. The basic IFTA design algorithm is illustrated in Figure 2.5. The algorithm starts from either a random or pre-designed initial phase distribution $U(x, y, 0)$ in aperture A at $z=0$ (in Figure 2.3). The diffraction pattern $U(x, y, z_0)$ of this distribution in signal window W is calculated by means of a Fourier transform and compared to the desired field pattern so that the fidelity of the field pattern within W is evaluated. After enforcement of design constraints, the field $U'(x, y, z_0)$ is propagated back to the aperture A by an inverse Fourier transform. The resulted field distribution $U'(x, y, 0)$ is then modified by introducing fabrication and/or amplitude constraints. The modified field $U(x, y, 0)$ is propagated again to get another diffraction pattern. The iteration is continued until a phase distribution is found which can generate a diffraction pattern sufficiently close to the desired one.

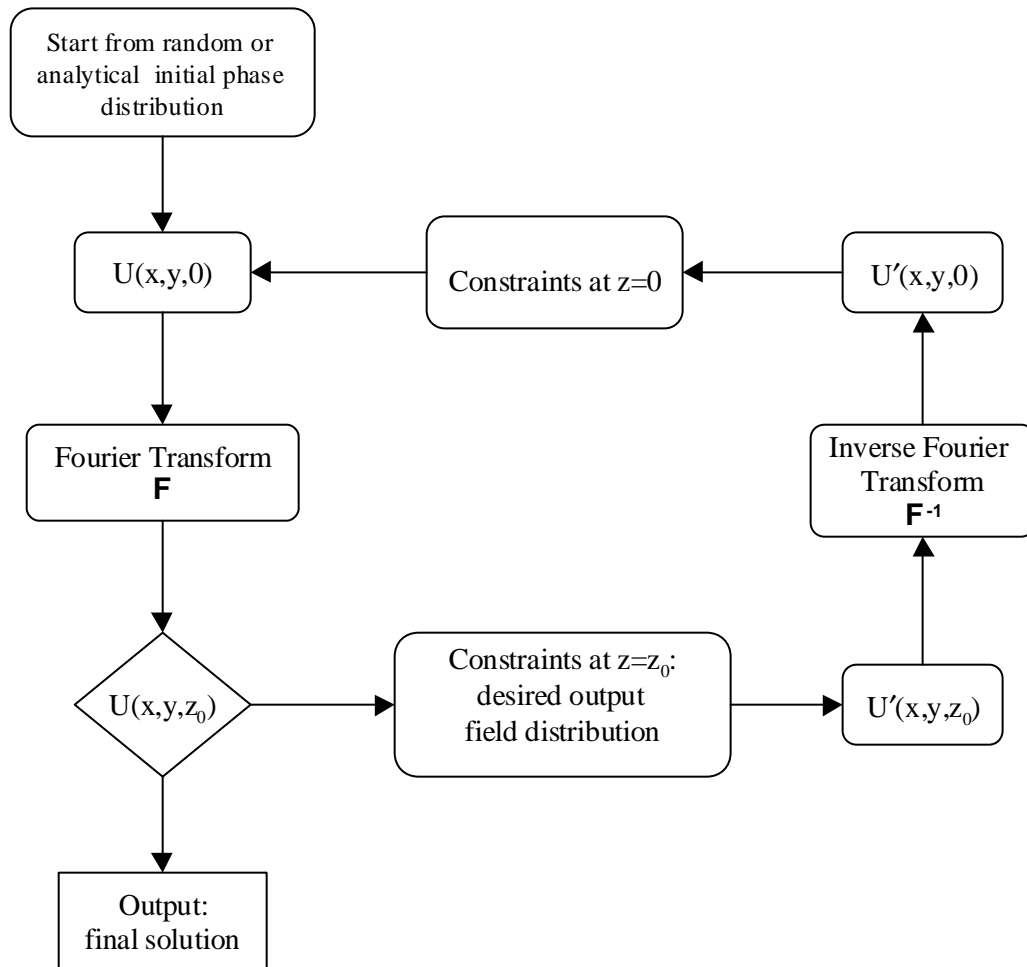


Figure 2.5 Illustration of the iterative Fourier transform algorithm (IFTA) for DOE design

There are several advantages of IFTA. First, it can optimize any desired intensity diffraction pattern. If a sufficient number of free design parameters are available, it is also possible to generate diffraction patterns with predetermined phases. Furthermore, IFTA algorithm

is usually computationally very efficient because it can employ fast Fourier transform (FFT) as the field propagation core. However, the biggest problem associated with IFTA is its tendency to stagnate in local optimum of the solution space. In other words, it is a local optimization algorithm. Thus the choice of the initial phase distribution is critical to the success of the final design. Efficient quantization algorithms that can ease stagnation problems have been developed [46], [47].

Beside IFTA, iterative design methods can also be applied in other DOE design regimes. For example, in the regime of Fresnel diffraction, an iterative Fresnel algorithm can be applied [48]. Also iterative angular spectrum design algorithm for designing sub-wavelength DOE's has been proposed [49].

2.3.4 Design methods based on rigorous electromagnetic diffraction theory

Generally speaking, scalar diffraction theory breaks down if the minimum feature size of the diffractive elements is of the order or less than the optical wavelength so that rigorous electromagnetic diffraction theory is required for the analysis and design of such elements. Nevertheless, the mathematical complexity of the rigorous diffraction theory results in two difficulties for design methods based on them. First, this complexity makes it impossible to invert these rigorous diffraction models. As shown in Figure 2.4(a), without the inverse operator T^{-1} , it is unable to develop bi-directional design methods so that the unidirectional methods are the only option for rigorous diffraction theory based design methods. Secondly, the computational cost associated with rigorous diffraction models is very high. Since unidirectional design methods usually require an additional global optimization method, which is also computationally expensive, the overall computational cost of the design methods can be prohibitively high. So when attempting to develop rigorous diffraction theory based design

methods, one must always keep this issue in mind and make every effort to improve the computational efficiency for both the rigorous diffraction model and the optimization method.

Global optimization of infinite periodic diffractive elements based on rigorous electromagnetic grating theory is feasible. Several design methods have been proposed. Johnson [50] optimized some polarization sensitive one-dimensional gratings for various applications by using RCWA as the rigorous diffraction model and micro-genetic algorithm as the global optimization method. Zhou *et al.* [51] employed RCWA in conjunction with the simulated annealing as optimization method for performing optimal design of binary-level surface-relief gratings with sub-wavelength features. Even in the case of two-dimensional gratings, locally optimized design is also possible if the symmetrical property of the grating profile can be fully utilized. For example, Nojonen *et al.* [52] optimized some resonant-domain beam splitters by using a 3-D eigenmode method along with a gradient local search method.

However, the situation is less satisfactory in the case of finite aperture aperiodic DOE design because rigorous analysis of such structures is far more complicated and computationally intensive than the analysis of gratings. At present only simple 2-D DOE structures, such as microlens (or microlens array) and focusing beam splitters, have been optimized. As far as the design method is concerned, recently Prather *et al.* [53] integrated the boundary element method (BEM) with simulated annealing for optimizing finite aperiodic subwavelength DOE's. In this dissertation, an alternative design method, μ GA-FDTD, has been developed, which employs a 2-D finite difference time domain (FDTD) method as the rigorous diffraction model in conjunction with a micro-genetic algorithm (μ GA) as the global optimization method. This rigorous design method will be addressed in detail in later chapters. With this efficient new tool, some novel DOE devices have been successfully designed and optimized.

Chapter 3

ANALYSIS OF STACKED ROTATED GRATING STRUCTURES

In the previous chapter it was mentioned that gratings have many important applications. Thus it is not surprising that stacked or cascaded multi-layer gratings also have numerous applications [50], [54]. In contrast, little attention has been paid to the stacked rotated grating structures (SRGS's). However, recently researchers found that they can be used as photonic crystals [6] and attracted a lot of research interests. The SRGS's considered herein are applied as circular polarization filters for infrared imaging polarimetry [22]. In this chapter, the structure of SRGS is present first and a circular polarization filter is then defined. Because there is no rigorous diffraction model for SRGS's in the literature, a rigorous diffraction model, termed as SRG-RCWA, is developed for certain type configurations of SRGS's for the first time. A three-dimensional RCWA algorithm with enhanced transmittance matrix method is developed first as the foundation to the analysis of general SRGS's, followed by a discussion of adaptations to this algorithm that are necessary to accommodate the unique features of SRGS's. The SRG-RCWA algorithm is applied onto the performance analysis of two fabricated circular polarization filters. Comparison between the SRG-RCWA numerical results and the experimental measurements is present as well.

3.1 Stacked rotated grating structure as circular polarization filters

As illustrated in Figure 3.1, stack rotated grating structures (SRGS's) generally consist of multiple one-dimensional binary gratings, which may be interleaved with homogeneous layers.

Figure 3.1 shows a simple stack with two gratings and a homogeneous layer in between, such simple structure is called bi-grating [55]. Unlike stacked gratings in which all grating layers must have the same grating period and vary periodically along the same direction, the gratings in SRGS's may have different grating periods and their periodic variations may be oriented in different directions. For example, grating 1 in Figure 3.1 has a period of Λ_1 while grating 2 has a period of Λ_2 and rotated angle β is relative to grating 1. As a result, generally the multi-layer stacked rotated grating diffraction problem is a three-dimensional grating diffraction problem as a whole, even though each individual grating layer is one-dimensional.

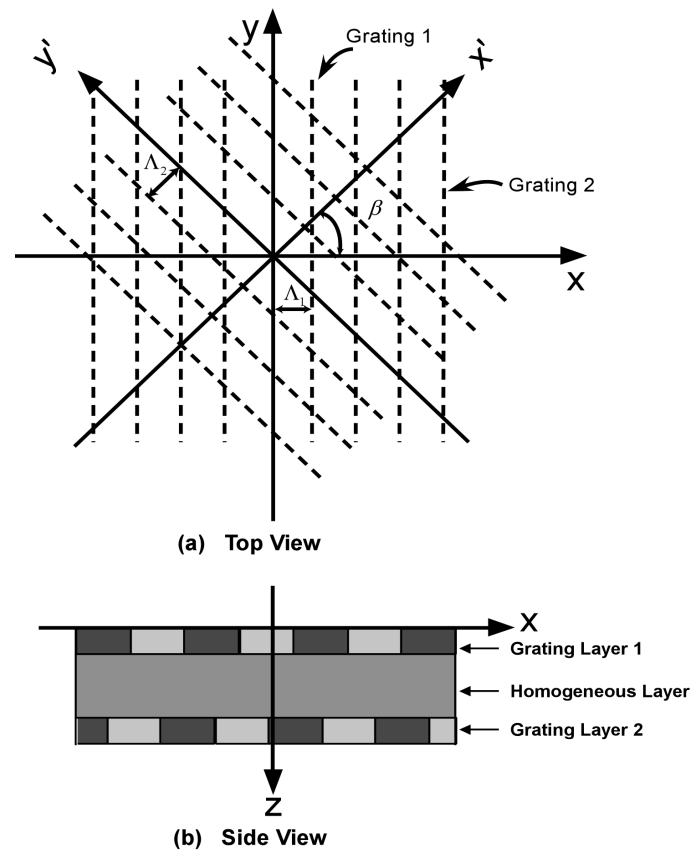


Figure 3.1 Schematic illustration of the stacked rotated grating structure

From the application point of view, the additional freedoms of grating period and orientation may bring some extra benefits so that SRGS's can realize some functions not addressable by stacked gratings. The application considered herein, circular polarization filter in an infrared imaging polarimetry system, is a typical example. Conceptually, to construct a circular polarization filter (which is a reversed circular polarizer) with classical optical components, a quarter-wave plate and a linear polarizer are required to be aligned so that the fast axis of the quarter-wave plate is rotated 45° relative to the polarization direction of the linear polarizer, as shown in Figure 3.2. If the incident light is right-hand circular polarized (RCP), it will be linearly polarized in the direction of 45° with respect to the x-axis after passing the quarter-wave plate and will be passed by the following polarizer. For left-hand circular polarized light (LCP), however, it will be linearly polarized in the direction of 135° with respect to x-axis after the quarter-wave plate and hence will be blocked by the polarizer.

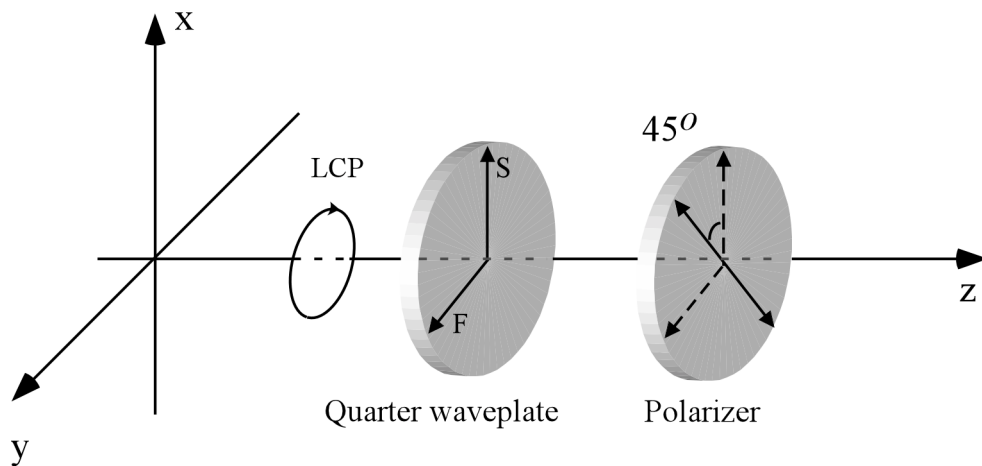


Figure 3.2 Classic setup of a circular polarization filter

It is feasible to achieve the same circular polarization filter by a stacked rotated grating structure. This can be done by the replacement of the quarter-wave plate and the linear polarizer by two sub-wavelength grating layers. The quarter-wave plate can be realized by a form bi-refrigrant sub-wavelength grating [56] and the linear polarizer can be achieved by a metallic grating as wire-grid polarizer [57]. Apparently, the two gratings must be rotated 45° relative to each other in order to pass or block the circular polarized lights. On the other hand, a homogeneous layer is necessary to separate them and to simplify the fabrication process at the same time. The overall SRGS for circular polarization detection is quite similar to that shown in Figure 3.1. Compared with the classic setup in Figure 3.2, the proposed SRGS is much more lightweight and compact, which is critical to the infrared imaging polarimetry application.

It is noticed that the bi-refrigrant quarter-wave plate and the wire-grid polarizer are originally designed individually for independent usage while in the proposed SRGS they are coupled through the homogeneous layer in between. This coupling effect along with the sub-wavelength feature size of the gratings must be rigorously addressed by the theoretical diffraction model in order to accurately predict the performance of the proposed SRGS for circular polarization filters.

Unfortunately no rigorous diffraction model is directly available for the analysis of SRGS's. For a simple bi-grating structure as shown in Figure 3.1, it is doubly periodic in the x direction and singly periodic in the y direction. Based on the multiple reflections of different diffracted orders in the homogeneous layer, Hwang [55] developed a diffraction model for bi-gratings. Though Hwang's method is suitable to the analysis of the proposed SRGS for infrared imaging polarimetry herein, it is not applicable to analyze general SRGS's with more than two grating layers, such as photonic band gap structures.

As previously mentioned, the diffraction problem of SRGS's is a three-dimensional diffraction problem in general, so a potential analysis approach for SRGS's is a three-dimensional RCWA algorithm for multi-layer two-dimensional grating (or crossed grating) structures [58],

[59], [60]. However, a three-dimensional RCWA algorithm requires that all grating layers must have the same periods Λ_x and Λ_y in the x and y direction, which is not usually true in SRGS's. Therefore some modifications to the three-dimensional RCWA algorithm must be made to accommodate the unique characteristics of SRGS's.

3.2 Three-dimensional RCWA algorithm

In this section, a new implementation of a standard three-dimensional RCWA algorithm is discussed as the basis of the rigorous diffraction model for SRGS's. Some new improvements to the existing three-dimensional RCWA algorithm will be discussed whereas the whole new implementation with full details is presented in Appendix A. The modified algorithm for SRGS's, namely the SRG-RCWA algorithm, will be addressed in Section 3.3.

3.2.1 New improvements to the existing three-dimensional RCWA algorithm

All numerical methods for analyzing a layered grating structure face a common difficulty associated with the exponential functions of the spatial variable in the direction perpendicular to the grating plane [61]. This difficulty will cause numerical instability. The numerical instability is exacerbated by the fact that accurate numerical analysis of gratings usually requires a large number of eigenmodes or spatial harmonics. Also the problem becomes more serious for thick grating layers. The most important criterion for achieving unconditional numerical stability is to avoid the exponentially growing functions in the calculation of every grating layer.

For the RCWA algorithm of multiple grating layers, the non-propagating evanescent space harmonics in the grating regions must be properly handled in the numerical implementation to achieve numerical stability. Moharam and Gaylord [7] originally developed a state-variables method for 1-D surface-relief dielectric gratings. They obtained stable results for grating depths up to four wavelengths (4λ) in TE illumination. However, as pointed out by Han *et al.* [62], the

state-variables method encounters numerical difficulties of inversion of a near-singular matrix when applied to 2-D gratings. To avoid this, Han *et al.* utilized a shoot-back method in their implementation of RCWA for 2-D dielectric surface-relief gratings with depth up to one wavelength (1λ). However, for gratings thicker than that, the grating must be divided into finer layers to produce a sufficiently accurate result. Since the computation time is roughly proportional to the number of layers used in the calculation, the shoot-back method obviously requires more computation time for thicker gratings. Furthermore, this method results in relatively large deviations from full conservation of power for dielectric gratings (on the order of 10^{-4}). This indicates that the numerical error of the shoot-back method is larger than other methods such as the state-variables method for 1-D gratings.

Later on, Chateau and Hugonin [63] presented a characteristic formalism and applied it to the analysis of 1-D deep surface relief and volume holographic gratings. Peng and Morris [64] extended the characteristic formalism to 2-D grating cases. However, the characteristic matrix method is more time consuming because more extra matrix operations are involved. Three multiplications and one inversion are needed to reduce the rank of the eigenvalue problem. In addition, many more matrix operations are required to reorder the eigenvalue and eigenvector matrix in growing order after the eigenvalue problem is solved. This reordering procedure must be done in every grating layer calculation. Therefore it is expected that their method will become inefficient for computations involving many spatial harmonics and many grating layers.

Recently, Moharam *et al.* [16] published a stable RCWA algorithm for 1-D gratings, termed as the enhanced transmittance matrix approach. With this approach, they obtained stable and convergent results for very deep (50λ) 1-D dielectric gratings. The method is straightforward and computationally efficient. In this dissertation, this enhanced transmittance matrix approach is extended to 2-D gratings and homogeneous layers for the first time. The extensions to both 2-D gratings and homogeneous layers are so important that it can be applied to the analysis of SRGS's in the future. With these generalizations, results similar to 1-D grating

case are achieved. The new RCWA implementation is stable for 2-D gratings of extreme depth and arbitrary profile, permittivities, and incident polarization. Numerical results for a 2-D metallic grating with 50λ depth are obtained by applying this new implementation, which will be presented later.

Another area of new improvement is in the eigenvalue problem. The second order differential equations derived from Maxwell's Equations are employed in this new implementation. This reduces the eigenvalue problem in standard 3-D RCWA code from rank $4MN$ down to $2MN$, where M and N are spatial harmonics retained in the x and y direction during the calculation. Because the required computation time of the eigenvalue problem of a $m \times m$ matrix is roughly proportional to m^3 , this rank reduction improves the computational efficiency by a factor of 8. The required computer memory is also reduced significantly because of the reduction of the size of the matrices. Though others [64] achieved this by manipulating the eigenvalue matrix resulting from first order differential equations, the method used here is more direct and requires less computation.

Also, the improved formulation of the eigenvalue problem proposed by Lalanne [65] is adopted in the new implementation to further increase the algorithm's efficiency. In this improved eigenvalue formulation, a grating profile dependent parameter α is introduced so that the eigenvalue problem can be optimized so that the convergence speed, i.e., convergence with increasing number of space harmonics retained in the calculation, can be improved.

3.2.2 Verification of the new implementation

Verification of the new three-dimensional RCWA implementation was conducted by applying it to some grating profiles in the literature [64], [65], [66], [67], [68], including the pyramid and checkerboard grating used by many authors. In all cases, the results of the new implementation matched the published ones very well. As it should be, the converging speed is

comparable to that of Lalanne's [65]. Also it successfully passed the criteria of conservation of power. The residual error in the conservation of power was always on the order of 10^{-12} , indicating the excellent accuracy of the new implementation.

There is no published data on extremely deep metallic 2-D gratings in the literature because such a grating is a real challenge for the stability and convergence of a numerical algorithm. Here an arbitrarily designed metallic 2-D grating with a $50\lambda_0$ depth is analyzed. The grating geometry is similar to the one shown in Figure A.1 except it is a single-layer grating with parameters: $\Lambda_x = \Lambda_y = \lambda_0$, $d = 50\lambda_0$, $n_I = 1.0$ (air) and $n_{III} = 1.5$ (glass), $\lambda_0 = 550nm$, $\theta = 30^\circ$, $\varphi = 45^\circ$, $\psi = 90^\circ$. The ridge-width along both the x and y directions is $0.5\lambda_0$. The refractive index of the groove is 1.0 and that of ridge is $(3.18-4.41j)^{1/2}$ (corresponding to chrome at 550nm). The profile-dependent parameter α is set to 0.5.

Several methods have been employed to analyze this thick grating. One approach is to take the grating as a single layer grating while others divide it into different sub-layers to test the extended enhanced transmittance matrix method. 5, 10, 25, 50 layers have been used and the results were found to be the same as that of the single layer case. The convergence curve of the diffraction efficiency of the reflected zero-th order is shown in Figure 3.3. It is evident that the diffraction efficiency converges, and the converging speed is quite fast, even for this extreme case. In fact, it is found that the convergence speed is virtually insensitive to the grating thickness. To achieve the same accuracy, a thin grating and an extremely thick grating require the same number of orders and therefore the same computational load.

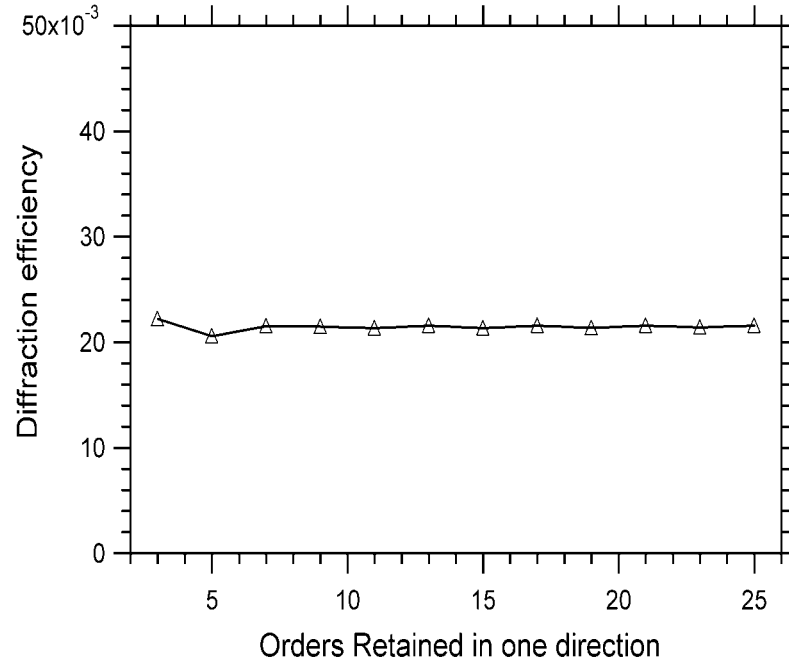


Figure 3.3 Three-dimensional RCWA algorithm convergence of the diffraction efficiency of reflected zero-th order as a function of the number of orders retained in one direction on an extreme thick metallic grating

3.3 Adaptation to 3-D RCWA for analysis stacked rotated gratings (SRG-RCWA)

3.3.1 Basic ideas and implementations of SRG-RCWA

In the three-dimensional RCWA algorithm, the requirement of same periods for all grating layers actually requires a rectangular diffraction order lattice in Fourier space, as illustrated in Figure 3.4. However, the one-dimensional grating layers in SRGS's generally result an irregular Fourier lattice so that the standard RCWA algorithm cannot be applicable to them. If, for some special cases, all diffracted orders generated by all the gratings in the SRGS lie on grids

of equally spaced points in k-space (called a sampling lattice as shown in Figure 3.5), that means all gratings can be expanded into a Fourier series with basic harmonics as f_{sx} and f_{sy} . In such cases, the standard RCWA algorithm will still work, but needs some modification in the Fourier expansion of both the permittivity functions and the electromagnetic fields of the gratings.

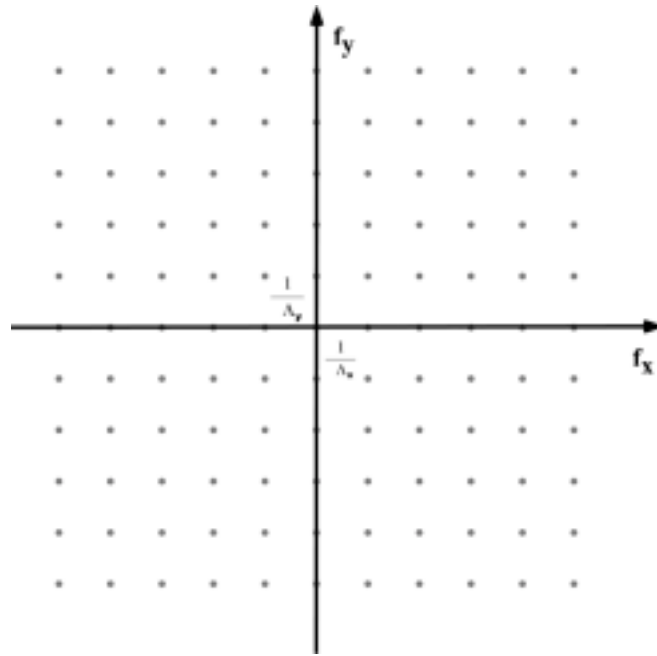


Figure 3.4 Three-dimensional RCWA diffraction order lattice in Fourier space

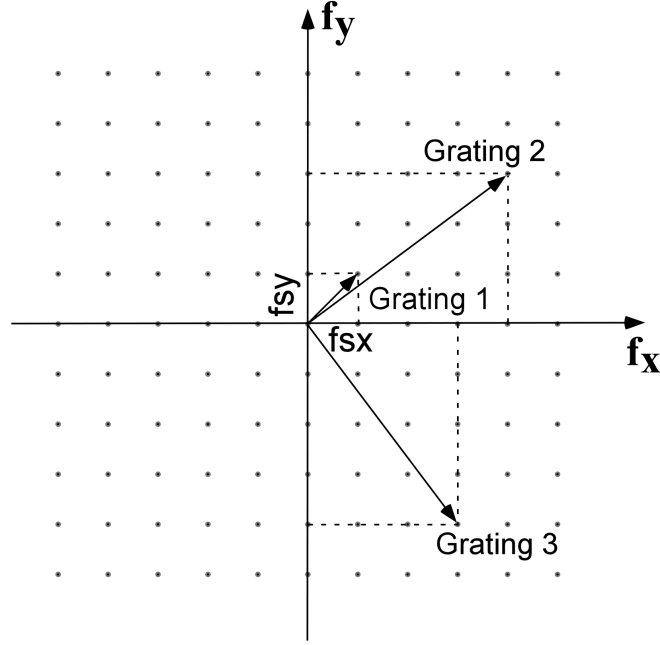


Figure 3.5 Frequency sampling lattice of SRG-RCWA and three sample grating \vec{K} -vectors

The grating parameters, i.e., grating period and angle between the grating \vec{K} vector and the f_x axis, for these special cases can be easily obtained. As shown in Figure 3.5, if the spacings of diffracted orders of a grating in f_x and f_y direction are n_x and n_y (n_x, n_y called sampling numbers for that grating), then the grating period Λ of the grating is

$$\Lambda = \frac{1}{\left[(n_x f_{sx})^2 + (n_y f_{sy})^2 \right]^{1/2}}, \quad (3.1)$$

and the angle between the grating \vec{K} vector and the f_x axis is

$$\sin \beta = \frac{n_y f_{sy}}{\left[(n_x f_{sx})^2 + (n_y f_{sy})^2 \right]^{1/2}} = n_y f_{sy} \cdot \Lambda. \quad (3.2)$$

For instance, in Figure 3.5, if $f_{sx} = f_{sy} = 1\mu\text{m}^{-1}$, then the parameters of the three illustrated gratings are

$$\text{Grating 1: } n_x = 1, n_y = 1; \Lambda = \frac{1}{\sqrt{2}} = 0.707 \mu\text{m}, \beta = 45^\circ, \quad (3.3)$$

$$\text{Grating 2: } n_x = 4, n_y = 3; \Lambda = \frac{1}{\sqrt{25}} = 0.2 \mu\text{m}, \beta = 36.87^\circ, \quad (3.4)$$

$$\text{Grating 3: } n_x = 3, n_y = -4; \Lambda = \frac{1}{\sqrt{25}} = 0.2 \mu\text{m}, \beta = -53.13^\circ. \quad (3.5)$$

The value of β is in the range $(-90^\circ, 90^\circ)$, in which the positive value corresponds to clockwise rotation and the negative values correspond to counter-clockwise rotation.

Practically, for a given SRGS, one can setup the f_x axis into the direction of one of the gratings in the stack, then pick a pair of (f_x, f_y) and calculate n_x and n_y for each grating. If there is no (f_x, f_y) pair that satisfies all gratings, some compromise must be made. This is the limitation of the algorithm. In all cases, a criterion is to minimize n_x and n_y in order to minimize the number of orders that must be retained and hence improve computational efficiency.

Once (f_x, f_y) is fixed, all grating layers can be expanded into the Fourier series of (f_x, f_y) . Similar to three-dimensional RCWA, the fields in incident region, grating region and exit region are also expanded into sampling harmonics in SRG-RCWA. Each sampling harmonic is phase matched on boundaries. The diffraction efficiency of each sampling harmonic is calculated with the same procedure as in the three-dimensional RCWA algorithm. A detailed discussion of mathematical modifications to the three-dimensional RCWA algorithm presented in Appendix A can be found in Appendix B.

3.3.2 Test case for SRG-RCWA algorithm

Since no literature examples on stacked rotated grating are available, an arbitrary three-layer sandwich grating stack is numerically designed to test SRG-RCWA. The sandwich grating stack has two grating layers and a homogeneous layer in between. The two grating layers are two

identical one-dimensional surface-relief gratings with orthogonal grating vectors, as shown in Figure 3.6. The gratings are $1\mu\text{m}$ in period and with 50% fill-factor. The thickness of grating layers is $1\mu\text{m}$. The refraction indices of the ridge region and groove region are 2.5 and 1.5 respectively. The refraction index of the homogeneous layer is 2.5 and the thickness is $2\mu\text{m}$. The indices of refraction of the incident and exit regions are 1.0 and 2.5 respectively. The wavelength of the incident beam is $5\mu\text{m}$.

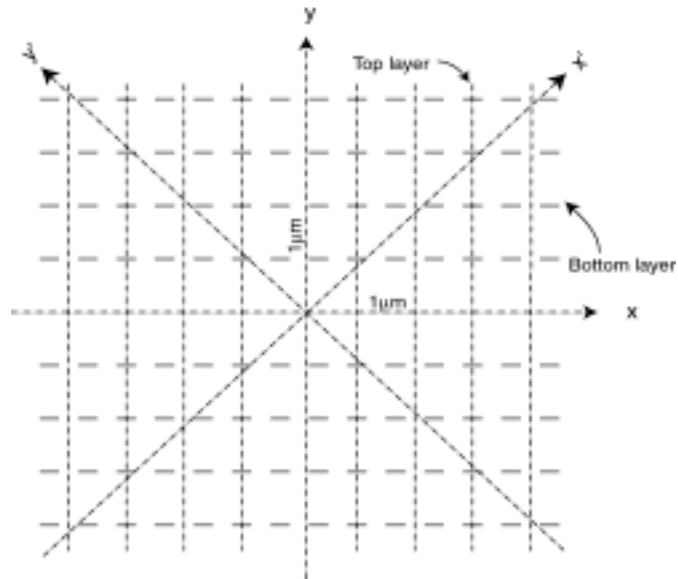


Figure 3.6 Coordinate system of sandwich grating stack

Since the two gratings are perpendicular to each other, the 3-D RCWA can be applied to the stack. In addition, the stack can also be analyzed with SRG-RCWA in two coordinate systems. In one system the x and y axes are parallel to the two grating vectors ($x - y$ system in Figure 3.6); the other is rotated 45° relative to the x - y system ($x' - y'$ system in Figure 3.6). The

sampling frequencies are $f_{sx} = f_{sy} = 1\mu\text{m}^{-1}$ in the $x - y$ system and $f'_{sx} = f'_{sy} = \frac{\sqrt{2}}{2}\mu\text{m}^{-1}$ in the $x' - y'$ system. TE polarization with respect to the $x - y$ coordinate system is studied with these three methods. The diffraction efficiency of transmitted zero order as a function of the number of orders retained in the calculation is compared in Figure 3.7. The results of 3-D RCWA and SRG-RCWA in the $x - y$ coordinate system matched very well, while SRG-RCWA in the $x' - y'$ system converges slightly slower. This is not surprising since the converging speed of RCWA algorithm is highly depended on the profile of the grating [65]. However, the difference of diffraction efficiency between 3-D RCWA and SRG-RCWA in the $x' - y'$ system is less than 0.05% if 441 (21×21) sampling harmonics are retained in both calculations, which is accurate enough for most applications.

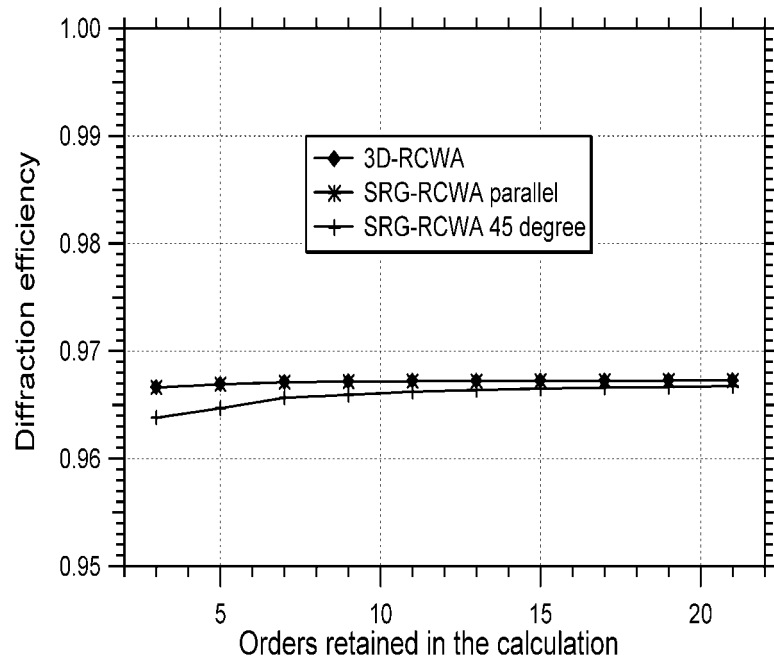


Figure 3.7 Comparison of three algorithms on sandwich grating stack

3.4 SRG-RCWA Performance analysis of two fabricated circular polarization filters

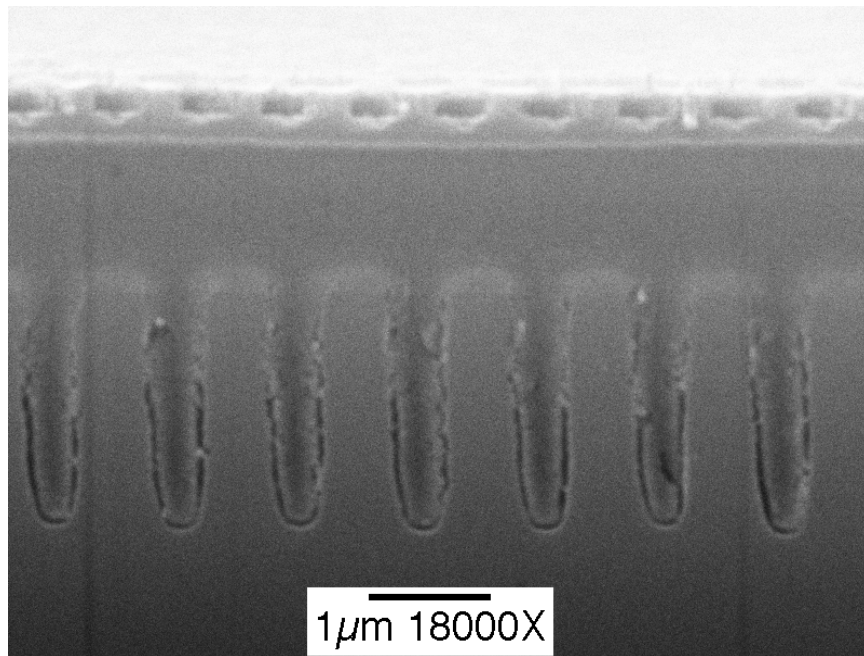
As proposed in Section 3.1, SRGS's can be employed to realize circular polarization filters for infrared polarimetry. Panfilo C. Deguzman, a recently graduated student from our group has successfully fabricated such filters with microlithography technologies for a real-time infrared imaging polarimetry system with wavelength range 3.5~5.0 μm [4]. He designed the wire-grid polarizer and the quarter-wave plate independently with a standard one-dimensional RCWA algorithm and then simply integrated them on top of each other in the fabrication process.

Figure 3.8 shows SEM images of two fabricated sample SRGS devices as circular polarization filters. The detailed structural layer parameters of them are listed in Table 3.1. Note a commercial broadband anti-reflection coating for the 3 to 5 μm wavelength range was applied to the backsides of sample wafers to suppress Fresnel reflections occurring at that interface, which are not shown in the SEM images. The wire-grid polarizers in these two devices are different; device 1 has a grating period of 0.5 μm while device 2 has a grating period of 1.0 μm . Also an additional Cr grating layer is evaporated on top of the Molybdenum layer to protect the polarizer. In device 1, there is an extra SiO_2 homogeneous layer, which serves an etch stop for the RIE etching in the fabrication process.

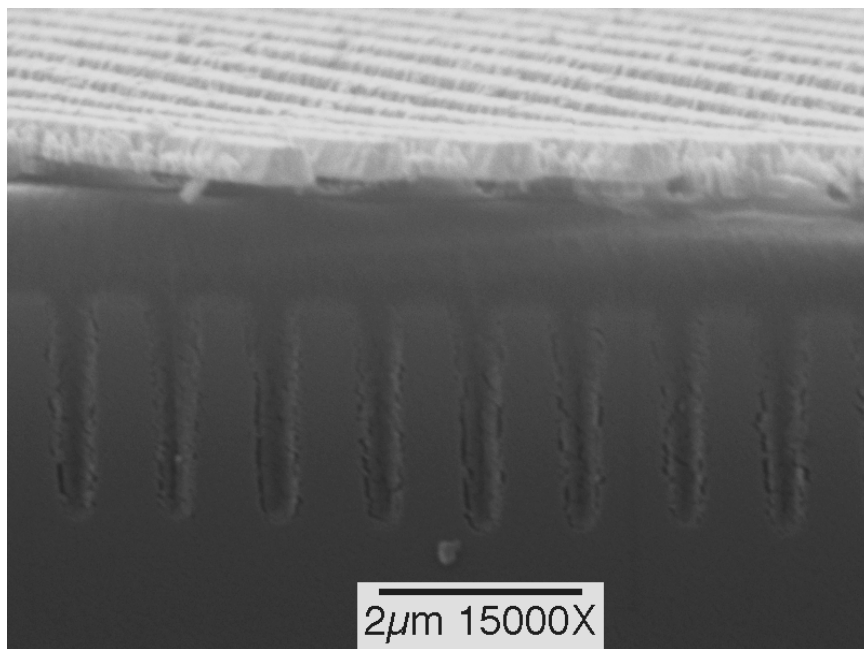
The performance of these SRGS devices as circular polarization filters is experimentally characterized by measuring the transmissions of incident LCP and RCP illumination. A key performance parameter, the circular extinction ratio (CER), can be defined as

$$CER \equiv \frac{T_{RCP}}{T_{LCP}}, \quad (3.6)$$

in which T_{RCP} and T_{LCP} are the transmissions of RCP and LCP respectively. An FTIR spectrometer (FTS-60A from BioRad) and an FTIR spectropolarimeter were used to obtain measurements across the desired wavelength range of 3.5 to 5 μm . The experimental measurements are shown in Figure 3.9 and Figure 3.10 respectively.



(a)



(b)

Figure 3.8 SEM images of the cross sections of two SRG sample devices as circular polarization detectors (a) device 1 and (b) device 2

Table 3.1 Detail structural layer parameters of two SRG sample devices as circular polarization detectors

			Device 1	Device 2
Incident media			Si	Si
Quarter-wave plate	Sub-layer 1	Ridge material	Si	Si
		Groove material	Su-8	Su-8
		Grating period (μm)	1.0	1.0
		Fill factor	62.2%	61.3%
		Thickness (μm)	0.72	0.5
	Sub-layer 2	Ridge material	Si	Si
		Groove material	Su-8	Su-8
		Grating period (μm)	1.0	1.0
		Fill factor	53.4%	54.2%
		Thickness (μm)	1.21	1.53
SU-8 homogeneous layer		Refractive index	Varying	Varying
		Thickness (μm)	1.26	1.47
Sio₂ homogeneous layer		Refractive index	Varying	—
		Thickness (μm)	0.1	—
Polarizer		Ridge material	Molybdenum	Molybdenum
		Groove material	Air	Air
		Grating period (μm)	0.5	1.0
		Fill factor	33%	41%
		Thickness (μm)	0.16	0.16
Cr layer		Ridge material	Cr	Cr
		Groove material	Air	Air
		Grating period (μm)	0.5	1.0
		Fill factor	70%	58%
		Thickness (μm)	0.025	0.27
Exit media			Air	Air

To apply the SRG-RCWA algorithm for the rigorous analysis of these two SRGS sample devices, one must first determine the sampling frequencies and sampling numbers for both the quarter-wave plate and the wire-grid polarizer. Unfortunately, for both sample devices, no pair of (f_{sx}, f_{sy}) can exactly match their structural configurations (grating periods and their orientations). Therefore some compromise must be made in order to apply SRG-RCWA to them. The final selected values for these parameters are listed in Table 3.2. Note for both devices, the x-axis of the coordinate systems is along the grating vector of the wire-grid polarizers. The sampling frequencies and sampling numbers exactly match configurations of the quarter-wave plates while approximations are made for the grating periods of the polarizers. According to Equation 3.1, it is straightforward to calculate their actual grating periods used in the SRG-RCWA analysis, which are $0.4714 \mu\text{m}$ and $1.0607 \mu\text{m}$ respectively.

Table 3.2 SRG-RCWA sampling frequencies and sampling numbers for simulation of two SRGS sample devices

		Device 1	Device 2
Sampling frequency	f_{sx}	$\sqrt{2}/2$	$\sqrt{2}/4$
	f_{sy}	$\sqrt{2}/2$	$\sqrt{2}/4$
Quarter wave plate	n_x	1	2
	n_y	-1	-2
	Grating period (μm)	1.0	1.0
Polarizer	n_x	3	3
	n_y	0	0
	Grating period (μm)	0.4714	1.0607

Another issue in the SRG-RCWA analysis is the imperfect circular polarization of the incident beam caused by the imperfect components used in the measurement to generate

“circular” polarized light. The incident beam is actually elliptically polarized. However, the polarization state information can be determined by the Jones Matrix method [4] combined with the measured performance of the used components. Table 3.3 shows the detailed input elliptical polarization parameters used in SRG-RCWA simulation, in which \mathbf{a} and \mathbf{b} are major- and minor-half-axis of the elliptical polarization and ψ is the angle between the major axis and the x-axis.

Table 3.3 Input elliptical polarization parameters to SRG-RCWA simulation

λ (μm)	\mathbf{b}/\mathbf{a}	Ψ_{RCP} ($^\circ$)	Ψ_{LCP} ($^\circ$)
3.5	0.75	94.38	85.62
3.75	0.75	94.08	85.92
4	0.79	90.40	89.60
4.25	0.85	87.21	92.79
4.5	0.92	86.87	93.13
4.75	0.98	79.93	100.07
5	0.97	30.50	149.50

In the SRG-RCWA simulation, the quarter-wave plate is divided into two sub-layers to approximate the irregular grating profile, as shown in Table 3.1. Overall, six different layers are used to simulate device 1 and five layers are used in device 2 simulation. The SRG-RCWA simulation results for these two devices are illustrated in Figure 3.9 and Figure 3.10, along with the measurement results for direct comparison.

On both devices, the SRG-RCWA results match the corresponding measurements very well for RCP mode. However, the LCP measured values are higher than simulation results, which cause the apparent disagreement between simulation and measurements in the circular extinction ratio (CER) because CER is very sensitive to LCP transmission. Two factors may account for this disagreement. From the numerical simulation side, the selected sampling frequencies and sampling numbers resulted somewhat different grating periods for both polarizers. Also only 15×15 harmonic orders are kept in the simulations. There are some other factors such as wave

plate profile approximation, which may cause some simulation error as well. From the experimental measurement side [4], the broad-band AR coating at silicon-air interface achieves transmission of 95% to 98.5% across the whole wavelength range of interest. The residual reflection may cause multiple reflections in the Si substrate. The LCP mode is affected more than the RCP because the circular polarization filters are designed to block LCP and therefore more light undergoes multiple reflections. On the other hand, the wire-grid polarizer has some defects due to fabrication error. Some regions are missing wire grid gratings and are therefore transparent to any incident polarization.

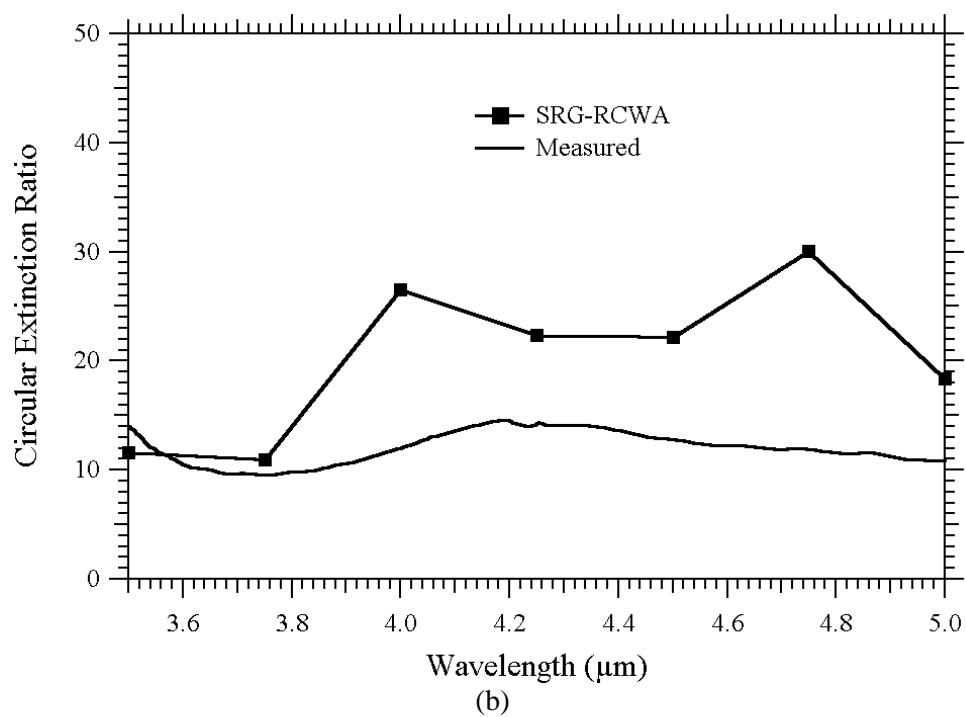
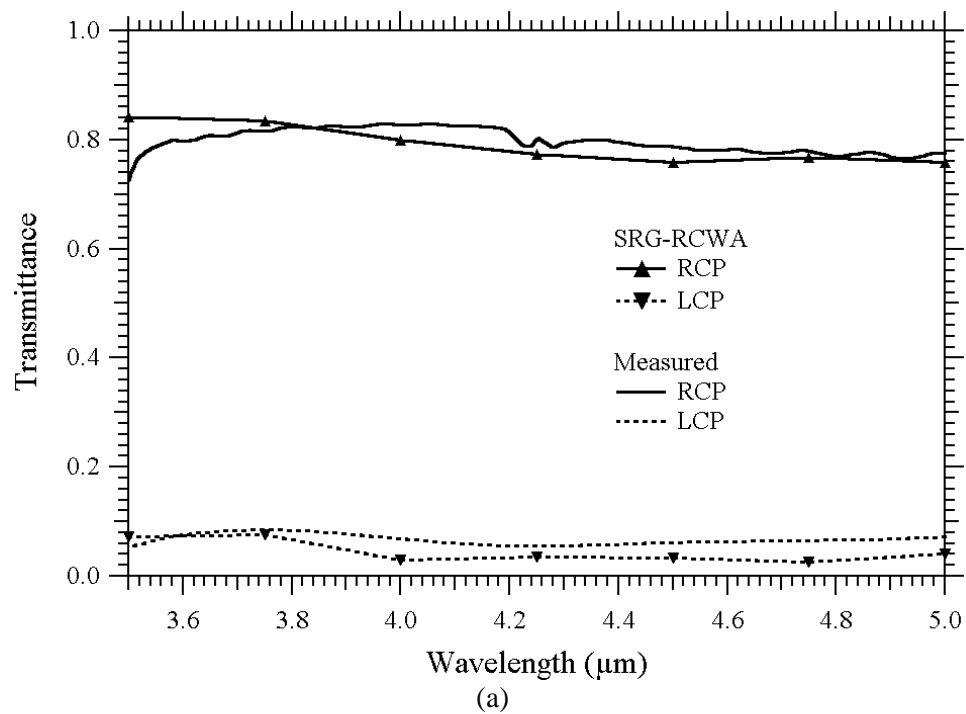


Figure 3.9 (a) Transmittance and (b) extinction ratio of SRGS sample device 1

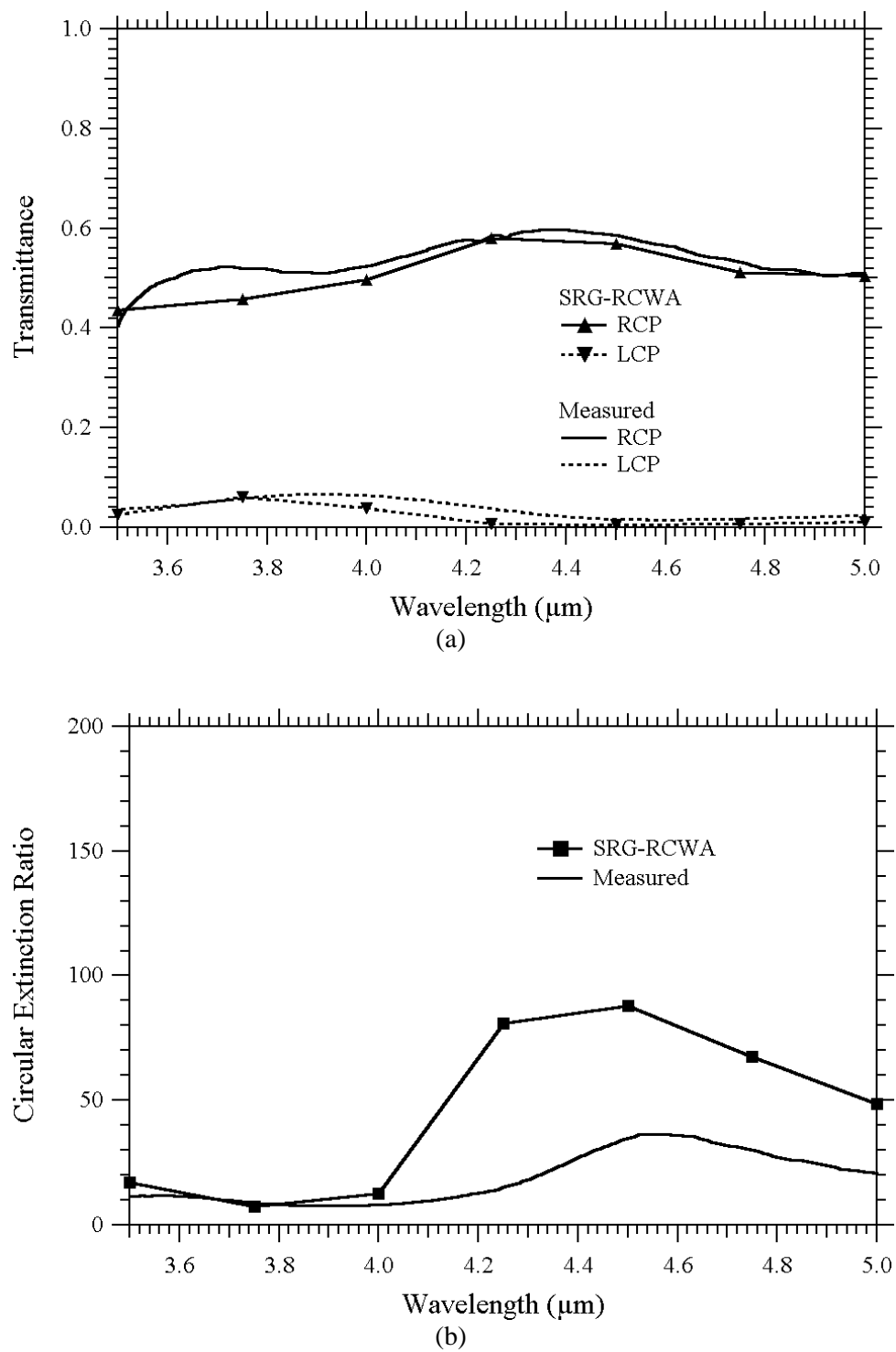


Figure 3.10 (a) Transmittance and (b) extinction ratio of SRGS sample device 2

Chapter 4

RIGOROUS DIFFRACTION MODELS FOR FINITE APERIODIC DOE'S

With advances in micro-fabrication technologies, it is now feasible to fabricate finite aperture aperiodic (FADOE's) with minimum feature size on the order of or less than the optical wavelength. The finite extent and aperiodic nature of FADOE's excludes the use of RCWA, which is only valid for infinite periodic gratings. Also, small feature size prevents the use of scalar theory. Rigorous analysis of FADOE's requires far more complicated diffraction models than those for infinite periodic DOE's, i.e., gratings. In recent years, several models have been adapted for this purpose, such as the boundary element method (BEM) [9], [69], the finite element method (FEM) [10], and the finite-difference time domain method (FDTD) [70]. In this dissertation the FDTD method is adopted as the rigorous diffraction model for analysis and design of FADOE's because it is computationally more efficient than other candidate methods. The implementation of a two-dimensional FDTD algorithm for the analysis and design of one-dimensional FADOE's is thoroughly discussed in this chapter. For the sake of completeness, brief reviews of the BEM and FEM methods are also included.

4.1 Boundary element method (BEM)

BEM has existed for a long time and has applications in a variety of engineering fields. Prather *et al.* [9] first introduced it to the analysis of diffractive optical elements. The basic concept behind BEM is that the diffracted or scattered field of finite aperture DOE is the re-radiation field of the surface field (for dielectric materials) or surface current (for conducting

materials), which is generated by the incident field. So the key issue of BEM is to numerically calculate the surface field or current distribution given the incident field and the DOE structure.

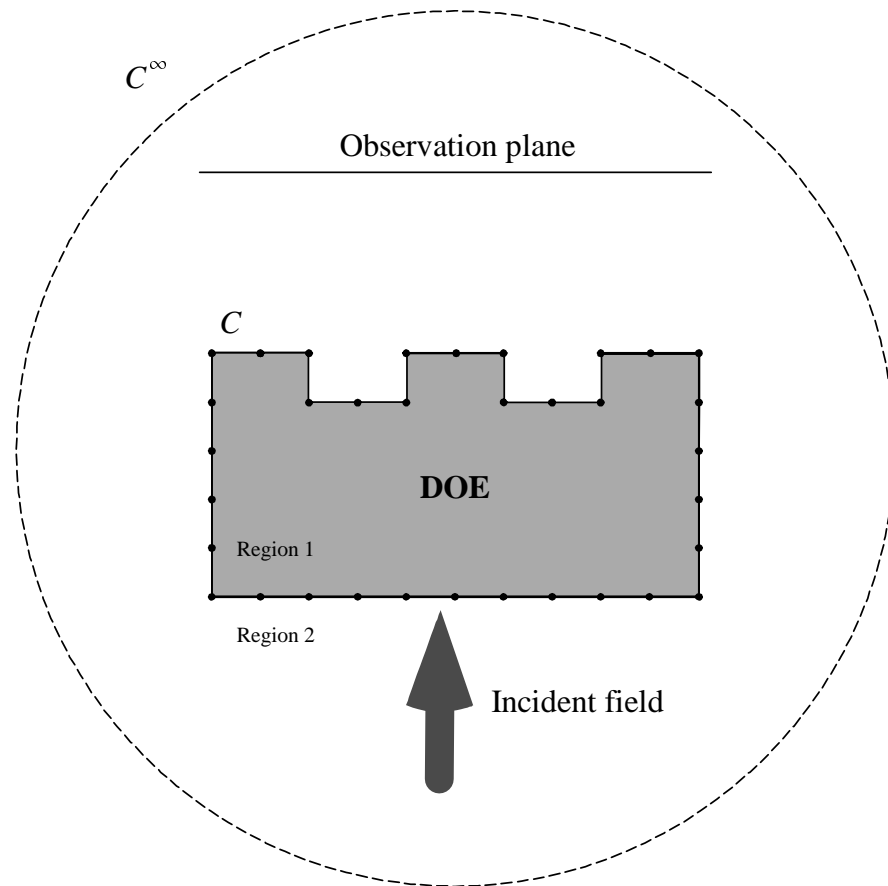


Figure 4.1 Geometry of boundary element method on analysis of DOE structures

As illustrated in Figure 4.1, the solution space is divided into two homogeneous regions: region 1, which contains the DOE, and region 2, which is free space. The two-dimensional time-harmonic wave equation is applied to each region. These equations can be cast into two coupled boundary integral equations by employing Green's theorem. To determine the electric field or current on the surface, the boundary C is sampled to reduce these coupled equations to a single

matrix equation in terms of the incident field values and the unknown scattered field. Solution of the matrix equation yields the scattered field or current values at the sampled nodes only. The field or current values elsewhere on the boundary can be determined by interpolation. The interpolated field or current values are then used to calculate the scattered field anywhere on the observation plane. If the total field values are desired, one can propagate the incident field to the observation plane by means of vector plane wave spectrum method.

One main shortcoming of BEM is that it requires a large amount of computer memory to obtain accurate results. The memory requirement is proportional to the square of the number of sampled points along the DOE boundary.

4.2 Finite element method (FEM)

Quite similar to BEM method, the FEM method has wide applications in many fields of engineering, especially Mechanical Engineering. This method is also commonly used in the antenna and microwave community to analyze scattering and waveguide problems. Lichtenberg *et al.* [10] first introduced the FEM to the optics community and applied it to the modeling of diffractive devices.

To illustrate the FEM method, a two-dimensional TE diffraction geometry is shown in Figure 4.2. A finite extended DOE is embedded in the FEM computational domain Ω , which is truncated by an outer boundary $\partial\Omega$. The outer boundary can consist either of a physical entity such as a metallic shield or an artificial boundary condition to simulate an unbounded, open space problem.

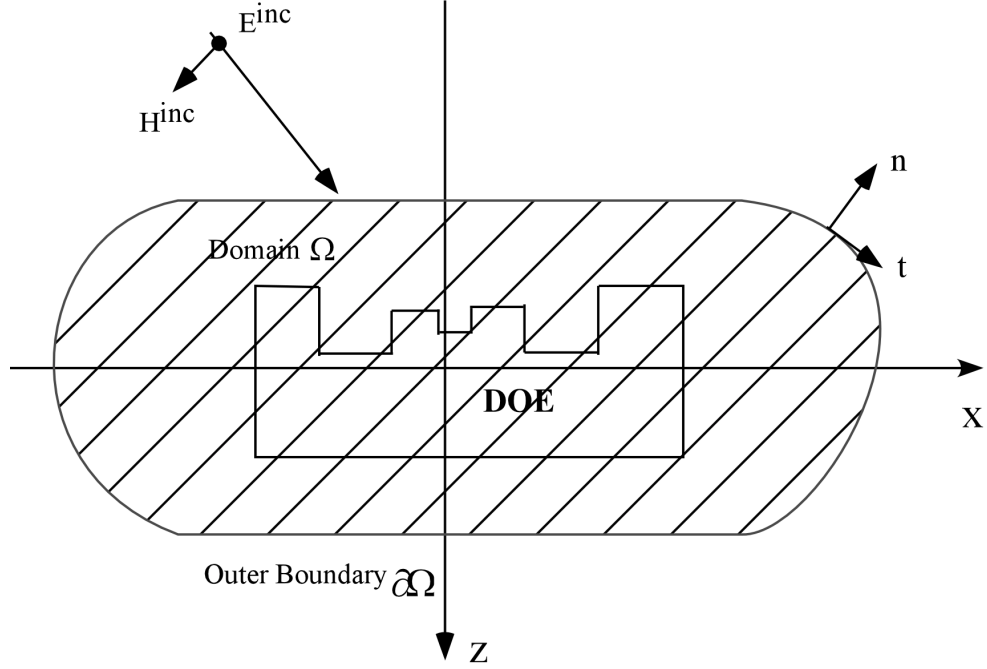


Figure 4.2 Two-dimensional TE diffraction geometry for FEM method

In the TE case, the FEM method starts with a variational form of the scalar Helmholtz equation for field component E_y

$$\int_{\Omega} \left\{ \mu_r^{-1} \nabla E_y^{tot} \cdot \nabla T^* - k_0^2 \epsilon_r E_y^{tot} T^* + g T^* \right\} dA = \oint_{\partial\Omega} \mu_r^{-1} \frac{\partial E_y^{tot}}{\partial n} T^* dt, \quad (4.1)$$

in which E_y^{tot} is the total field to be determined, μ_r and ϵ_r are the relative material constants, g is an electric or magnetic source inside the computational domain and k_0 is the wave number in free space. n and t are the outward normal and the tangential direction along the boundary respectively. The functional arising in the variational formulation can also be considered as an energy-related expression of the problem, which must be minimized to find the solution.

Then the variational formulation will be discretized over a spatial grid of small finite mesh elements, normally triangular cells of constant permittivity and permeability. It is assumed

that the electrical field E_y^{tot} can be represented as a combination of known real linear interpolation functions across these elements,

$$E_y^{tot}(x, z) = \sum_{i=1}^N e_i B_i(x, z), \quad (4.2)$$

in which e_i are unknown field values on the nodes. These N interpolation functions form a basis set for the solution. The testing function T in Equation 4.1 is set to each of the N basis functions $B_i(x, z)$ which results in a system of N linearly independent equations of the form

$$\mathbf{M}\mathbf{e} = \mathbf{c}, \quad (4.3)$$

in which the system matrix \mathbf{M} and coefficient vector \mathbf{c} can be analytically or numerically calculated while the actual expression of them depend on the outer boundary conditions applied to the surface integral on the right hand side of Equation 4.1. Equation 4.3 must be solved for the field values on the nodes \mathbf{e} and the field anywhere from nodes in the modeling region can then be determined by interpolation using Equation 4.2.

4.3 Finite-difference time-domain method (FDTD)

In contrast to BEM and FEM, the FDTD method directly solves the time-dependent Maxwell's curl equations by a recursive method referred to as Yee's time-marching algorithm [13]. Because of its time-dependent nature, the FDTD method can be used to obtain both the steady state and the transient response of the DOE structure. Also, by employing pulse incident sources, the spectrum response of the DOE can be obtained within a single run, which can save a lot of computer time in certain applications. Most importantly the computational cost associated with FDTD, i.e., the memory requirement and CPU time, is linearly proportional to the number of sampled points or nodes within the FDTD computational area, which is very attractive as far as electrically large DOE structures are concerned. Due to these unique features, the FDTD method

is particularly efficient for DOE modeling. In this dissertation, a two-dimensional FDTD algorithm for both TE and TM polarized illumination with arbitrary incident angle is fully developed and is integrated into a rigorous design tool for designing FADOE's.

In this section, an overview of the FDTD method is first presented to give a overview of the method. After that, the detailed algorithms for a two-dimensional FDTD algorithm are described subsequently. Then the application of the developed FDTD algorithm to the analysis of two-dimensional FADOE's is illustrated with some special considerations to accommodate the unique features of two-dimensional FADOE's. Finally a two-dimensional dielectric circular cylinder scattering problem is used to validate the developed two-dimensional FDTD algorithm.

4.3.1 Overview of the FDTD method

The FDTD method was first proposed by Yee in 1966 [13] and was later developed by Taflove and others. In recent years, the microwave community has put forth considerable effort to make FDTD more efficient and more powerful [71]. Now FDTD is one of the most widely used numerical techniques for solving electromagnetic problems. Applications of FDTD in the optics field have begun to emerge [72], [73], [74].

Typically, the FDTD method employs a set of simple, second-order accurate central-difference equations for the space and time derivatives to approximate Maxwell's time-dependent curl equations. The unknown electric and magnetic field within and surrounding the structure of interest are volumetrically sampled and over a period of time. They interleave both in the space and time domains. After incorporating a time-dependent incident field, time-marching is accomplished by repeatedly implementing the finite difference equations at each cell of the corresponding space lattice. After steady state is reached, the steady state near field information can be extracted. If the far field response is desired, an appropriate near to far field transformation algorithm can be applied to propagate the scattered fields to the plane of interest, where the radar cross section or diffraction efficiencies can be determined.

Overall, the FDTD method is a time-marching procedure that simulates the continuous actual wave propagation in the physical medium by numerical wave propagation in the data space stored in a computer. At each time step, the system of equations to update the field components is fully explicit so that there is no need to solve a linear equation system.

Generally, the FDTD algorithm involves some major sub-algorithms. They are (1) basic Yee's algorithm for sampling Maxwell's Equations in both space and time, (2) absorbing boundary conditions (ABCs) for simulating open space regions, (3) incident field algorithm, (4) algorithm for reducing numerical dispersion error, and (5) near-far or near-near field transformation algorithm. All of them will be discussed in the following in the frame of two-dimensional TE case while The TM case can be easily derived by duality theory [75].

4.3.2 Basic Yee's algorithm

Consider a rather general two-dimensional scattering problem shown in Figure 4.3. The scattering structure is assumed to extend to infinity without any variation in the y direction. The modeling space is a source free region with dielectric material only. In TE case, only E_y , H_x , and H_z field components are involved and are governed by time-dependent Maxwell's equations

$$\frac{\partial E_y}{\partial t} = \frac{1}{\epsilon} \left(\frac{\partial H_x}{\partial z} - \frac{\partial H_z}{\partial x} \right), \quad (4.4)$$

$$\frac{\partial H_x}{\partial t} = \frac{1}{\mu} \frac{\partial E_y}{\partial z}, \quad (4.5)$$

$$\frac{\partial H_z}{\partial t} = -\frac{1}{\mu} \frac{\partial E_y}{\partial x}. \quad (4.6)$$

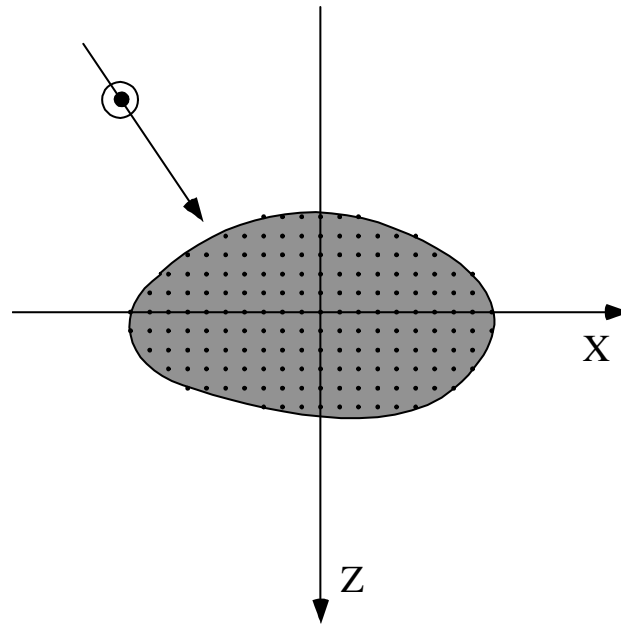


Figure 4.3 General two-dimensional TE scattering geometry with FDTD sampling grid

4.3.2.1 Basic ideas

In 1966, Kane Yee originated a set of finite-difference equation to numerically solve the time-dependent Maxwell's equations such as Equation 4.4. In Yee's algorithm, both electric and magnetic fields are sampled both in space and time. In the two-dimensional TE case, the field components E_y , H_x , and H_z are sampled by a uniform space grid with a unit cell shown in Figure 4.4. In this grid, electric and magnetic field components are interleaved in such a way that every electric component is surrounded by four circulating magnetic components. This positioning method has numerous advantages. First of all, the resultant finite-difference equations for the space derivatives used in curl operators are central in nature and second-order accurate. Secondly, the continuity of the tangential electric and magnetic fields is naturally maintained across an interface of different materials if the interface is parallel to one of the grid coordinate

axes so that there is no special effort needed to match field boundary conditions at the interface. At the beginning of the problem, the material permittivity and permeability of the modeling structure are simply specified at each field component location. For a rectangular Yee mesh, this yields a “staircase” approximation of the surface and internal geometry of the modeling structure with a space resolution set by the unit cell of the mesh.

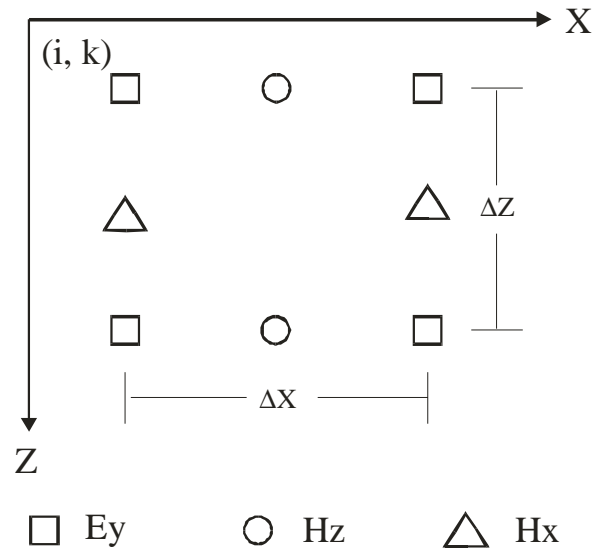


Figure 4.4 Unit cell of Yee's FDTD algorithm for TE illumination

As illustrated in Figure 4.5, the Yee algorithm also centers its \vec{E} and \vec{H} components in time domain in the style termed as leapfrog arrangement. All of the \vec{E} computations in the FDTD grid area are completed and stored in memory for a particular time point using the \vec{H} data previously stored in the memory. Then all of the \vec{H} computations are completed and stored in memory using the \vec{E} data just computed. The cycle can begin again with the re-calculation of the \vec{E} components based on the latest \vec{H} . This process continues until the time-marching is

concluded. This leapfrog time-marching process is fully explicit, thereby completely avoids the problems involved with simultaneous equations and matrix inversion. Another advantage of this arrangement is that the resultant finite-difference expressions for the time derivatives used in the curl equations are also central differenced and with second-order accuracy.

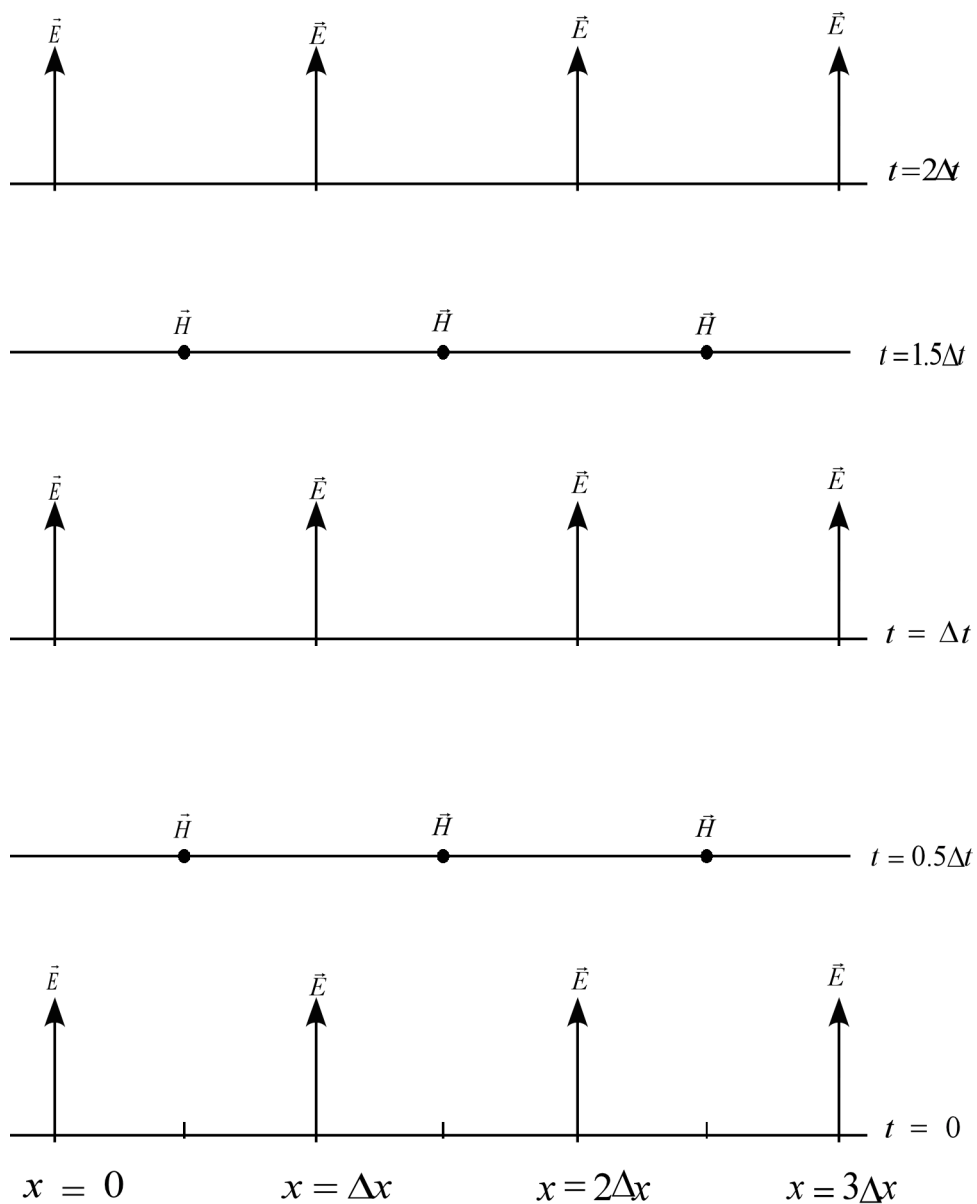


Figure 4.5 Space-time diagram of the Yee's algorithm for a one-dimensional wave propagation example showing the use of central differences for the space derivatives and leapfrog for the time derivatives

4.3.2.2 Notation and finite difference approximations

Yee introduced a set of notation for the finite difference operation of functions of space and time. For convenience, his notation is repeated here. Referring to Figure 4.2, a space point in a two-dimensional uniform rectangular grid is denoted as

$$(i, k) \equiv (i\Delta x, k\Delta z), \quad (4.7)$$

in which Δx and Δz are respectively, the space increments in the x and z directions and i and k are integer indices for that space point. Furthermore, any function f of space and time evaluated at a discrete space point and at a discrete time point is denoted as

$$f(i\Delta x, k\Delta z, n\Delta t) \equiv f_{i,k}^n, \quad (4.8)$$

in which Δt is the time increment, assumed uniform over the observation interval and n is the integer index for that time point.

In Yee's notation, the first partial space derivative of f in the x -direction, evaluated at time point n is approximated by a central difference as

$$\frac{\partial f}{\partial x}(i\Delta x, k\Delta z, n\Delta t) = \frac{f_{i+1/2,k}^n - f_{i-1/2,k}^n}{\Delta x} + O[(\Delta x)^2]. \quad (4.9)$$

Note the $\pm 1/2$ increment in i index denotes a space finite difference over $\pm 1/2 \Delta x$, rather than full Δx . Yee's expression for the first time part derivative of f , evaluated at the space point (i, k) , follows by analogy:

$$\frac{\partial f}{\partial t}(i\Delta x, k\Delta z, n\Delta t) = \frac{f_{i,k}^{n+1/2} - f_{i,k}^{n-1/2}}{\Delta t} + O[(\Delta t)^2]. \quad (4.10)$$

Note again the $\pm 1/2$ increment in index n denotes a time finite difference over $\pm 1/2 \Delta t$, rather than full Δt .

By applying above ideas and notations, the Maxwell's Equations given by Equation 4.4, 4.5 and 4.6 can be approximated by a set of finite difference equations as

$$E_y|_{i,k}^{n+1} = E_y|_{i,k}^n + \frac{\Delta t}{\epsilon_{i,k}} \left[\left(H_x|_{i,k+1/2}^{n+1/2} - H_x|_{i,k-1/2}^{n+1/2} \right) / \Delta z - \left(H_z|_{i+1/2,k}^{n+1/2} - H_z|_{i-1/2,k}^{n+1/2} \right) / \Delta x \right], \quad (4.11)$$

$$H_x|_{i,k+1/2}^{n+1/2} = H_x|_{i,k+1/2}^{n-1/2} + \frac{\Delta t}{\mu \Delta z} \left(E_y|_{i,k+1}^n - E_y|_{i,k}^n \right), \quad (4.12)$$

$$H_z|_{i+1/2,k}^{n+1/2} = H_z|_{i+1/2,k}^{n-1/2} + \frac{\Delta t}{\mu \Delta x} \left(E_y|_{i+1,k}^n - E_y|_{i,k}^n \right). \quad (4.13)$$

The Yee's algorithm defined by these difference equations requires that the time increment Δt has a specific bound relative to the space increments Δx and Δz to avoid numerical instability. This stability condition can be expressed as

$$\Delta t \leq \frac{1}{c \sqrt{\frac{1}{(\Delta x)^2} + \frac{1}{(\Delta z)^2}}}. \quad (4.14)$$

in which c is the speed of light in the modeling media. Also Δx and Δz are usually less than $\lambda/20$ to ensure numerical accuracy, where λ is the wavelength of the illumination.

4.3.3 Absorbing boundary conditions (ABC's)

In the FDTD algorithm, the electromagnetic fields are sampled in a finite volume of space around the structure of interest. The sampling lattice, i.e., computational domain, must be truncated at a certain place due to the limitation of the computer memory. For the open space problems, where the spatial domain of the computed field is unbounded in one or more coordinate directions, a boundary condition on the outer boundaries of the sampling lattice is needed to simulate the infinite extent of the problem. That boundary condition should permit the outgoing wave to pass through without any reflection. Such boundary conditions are called absorbing boundary conditions (ABC's).

ABC's cannot be directly derived from the Yee's algorithm. Principally this is because Yee's algorithm employs a central spatial difference scheme that requires field information one half space cell to each side of a sampling point. For the outermost sampling points, the central

differences cannot be implemented since the fields at one-half space cell outside of them are unknown. Although it is possible to derive exact analytical expressions for the fields at the outer grid boundary in terms of known fields within the grid by using Green's theorem, such expressions are "global" in nature in that the field data required are located at a contour completely enclosing the computation domain. The high computational burden associated with the storage and processing of these data makes the "global" approach unpractical. In contrast, local ABC's require field data only in the vicinity of the outer boundary and therefore need minimum computational cost. The computer resource advantage of local ABC's relative to global ABC's is so decisive that almost all existing FDTD codes use local ABC's.

Historically various kinds of local ABC's have been developed, such as Bayliss-Turkel scattered-wave annihilating ABC [76], Mur's ABC [77], Liao's ABC [78], and Berenger's perfect match layer (PML) ABC [79]. Berenger's PML ABC represents the present state of art in ABC's and is implemented in this dissertation.

The basic idea of Berenger's PML ABC is to construct a nonphysical impedance-matched absorbing medium with both electric and magnetic losses adjacent to the outer FDTD mesh boundary. Consider the two-dimensional TE case again, for free space with possible electric and magnetic loss, the Maxwell's Equations can be rewritten as

$$\epsilon_0 \frac{\partial E_y}{\partial t} + \sigma E_y = \frac{\partial H_x}{\partial z} - \frac{\partial H_z}{\partial x}, \quad (4.15)$$

$$\mu_0 \frac{\partial H_x}{\partial t} + \sigma^* H_x = \frac{\partial E_y}{\partial z}, \quad (4.16)$$

$$\mu_0 \frac{\partial H_z}{\partial t} + \sigma^* H_z = -\frac{\partial E_y}{\partial x}, \quad (4.17)$$

in which ϵ_0 and μ_0 are free space permittivity and permeability and σ and σ^* denote the electric conductivity and magnetic loss of the free space. It is well known that if the following condition is satisfied

$$\frac{\sigma}{\epsilon_0} = \frac{\sigma^*}{\mu_0}, \quad (4.18)$$

the intrinsic impedance of the lossy free space medium matches that of the lossless vacuum, and no reflection will occur when a plane wave propagates normally across the interface between them.

Berenger introduced a new way to assign electric and magnetic loss by splitting E_y into two sub-components denoted as E_{yx} and E_{yz} . The four field components, rather than the usual three, are coupled by the following equations:

$$\epsilon_0 \frac{\partial E_{yx}}{\partial t} + \sigma_x E_{yx} = -\frac{\partial H_z}{\partial x}, \quad (4.19)$$

$$\epsilon_0 \frac{\partial E_{yz}}{\partial t} + \sigma_z E_{yz} = -\frac{\partial H_x}{\partial x}, \quad (4.20)$$

$$\mu_0 \frac{\partial H_x}{\partial t} + \sigma_z^* H_x = \frac{\partial (E_{yx} + E_{yz})}{\partial z}, \quad (4.21)$$

$$\mu_0 \frac{\partial H_z}{\partial t} + \sigma_x^* H_z = -\frac{\partial (E_{yx} + E_{yz})}{\partial x}, \quad (4.22)$$

in which the parameters σ_x and σ_y are electric conductivities and σ_x^* and σ_z^* are magnetic losses. Each pair of (σ_x, σ_x^*) and (σ_z, σ_z^*) must satisfy the condition of Equation 4.18.

Consider the two-dimensional TE FDTD scattering shown in Figure 4.6, to implement Berenger's PML ABC, a PML region backed by perfectly conducting (PEC) walls surrounds the normal free space FDTD computation region. In the PML region, the field-split Maxwell's Equations (Equations 4.19 to 4.22) must be used for Yee's algorithm. At both the left and right sides of the FDTD grid, each PML has matched (σ_x, σ_x^*) along with $\sigma_z = \sigma_z^* = 0$ to permit reflectionless transmission across the vacuum-PML interface. Similarly, at both the lower and upper sides of the FDTD grid, each PML has matched (σ_z, σ_z^*) along with $\sigma_x = \sigma_x^* = 0$. At

four corners of the grid where there is overlap of two PML's, all four losses are present and set to those of the adjacent PML's. In each PML region, the losses should increase gradually with depth ρ as

$$\sigma(\rho) = \sigma_{\max} (\rho/\delta)^n, \quad (4.23)$$

in which δ is the total thickness of the PML region and σ is either σ_x or σ_z . This yields a PML reflection factor of

$$R(\theta) = \exp\left(-\frac{2\sigma_{\max}\delta \cos\theta}{(n+1)\epsilon_0 c}\right). \quad (4.24)$$

For $\theta = 0$, it gives out the theoretical reflection coefficient at normal incidence for the PML over PEC

$$R(0) = \exp\left(-\frac{2\sigma_{\max}\delta}{(n+1)\epsilon_0 c}\right), \quad (4.25)$$

which is user-defined and is usually set to 10^{-5} in most implementations of PML.

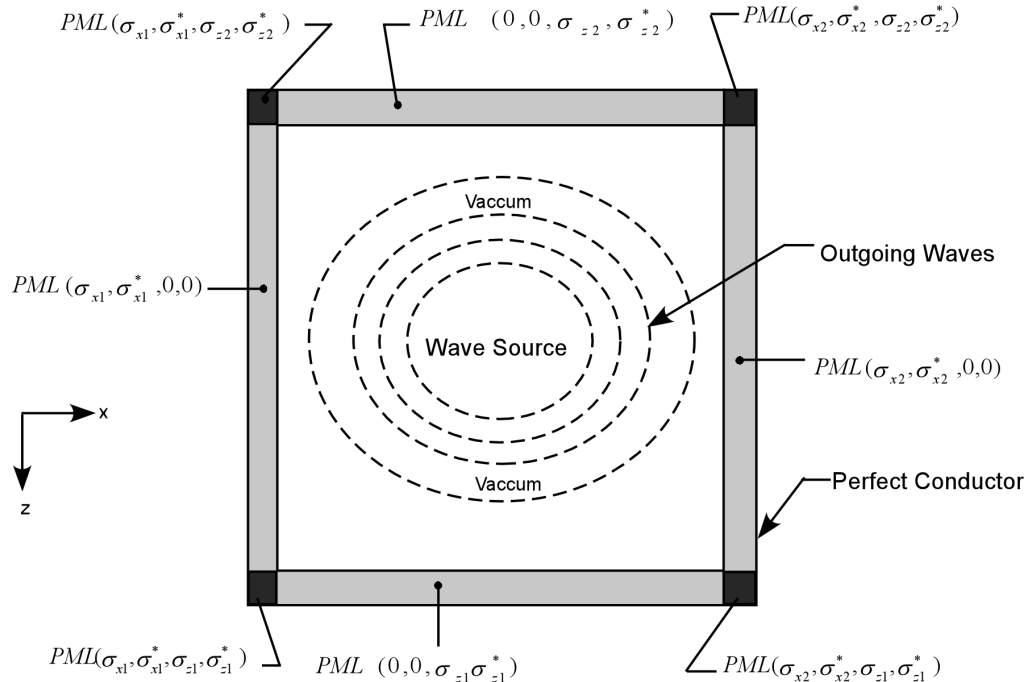


Figure 4.6 Implementation of Berenger PML ABC for two-dimensional FDTD algorithm in the TE case

4.3.4 Incident field algorithm

To activate the FDTD algorithm, an electromagnetic excitation (or incident field) must be introduced into the FDTD lattice. There are several different ways to generate an incident wave source for the FDTD algorithm. One approach is to insert the incident wave as an initial condition, in which the field components at all FDTD sampling points are initialized according to the desired wave source [13] at the beginning of the Yee algorithm. The initial condition approach is a non-compact wave source in the sense that many extra FDTD cells must be added to lengthen the computational region to physically contain the long duration pulses or continuous sinusoidal plane wave. Another method is to insert the incident wave as a hard source. The hard source is set up simply by assigning the desired source function to specific electric or magnetic

field components in the FDTD lattice. The problem of the hard source approach is that it will cause spurious, nonphysical reflection when the numerical wave propagates upon the source grid because it cannot permit the numerical wave to pass through (hence terminology hard source).

The total/scattered field formulation [77], [80] was the first compact wave source that succeeded in all respects and still remains in use today for popular FDTD software. As illustrated later, this approach is found to be particularly suitable for DOE modeling and therefore is adopted. The total/scattered field formulation is based on the linearity of Maxwell's equations and the decomposition of the electric and magnetic fields as

$$\vec{E}_{tot} = \vec{E}_{inc} + \vec{E}_{scat} , \quad (4.26)$$

$$\vec{H}_{tot} = \vec{H}_{inc} + \vec{H}_{scat} . \quad (4.27)$$

Here \vec{E}_{inc} and \vec{H}_{inc} are the values of the incident wave fields, which are assumed to be known at all space points of the FDTD grid at all time steps. These are the field values that would exist in the homogeneous incident medium, that is, if there were no DOE in the FDTD modeling space.

\vec{E}_{scat} and \vec{H}_{scat} are the values of the scattered wave fields, which are initially unknown. These are the fields that result from the interaction of the incident wave with the DOE structure. The Yee algorithm can be applied to either total field components or scattered field components with equal validity.

As shown in Figure 4.7, in total/scattered field approach, the FDTD computational region is divided into two regions by a virtual surface. Region 1, the inner zone of the lattice, is called the total field region. In this region it is assumed that the FDTD algorithm operates on the total field components. Normally the DOE structures are embedded within this region. Region 2, the outer zone of the lattice, is called the scattered field region. Here the FDTD algorithm operates only on the scattered field components. A connecting condition is provided at the interface of the total field and scattered field regions, which ensures consistency of the FDTD algorithm and

simultaneously generates an arbitrary incident wave source in region 1 with a user-defined time waveform and duration, angle of incidence and the desired polarization.

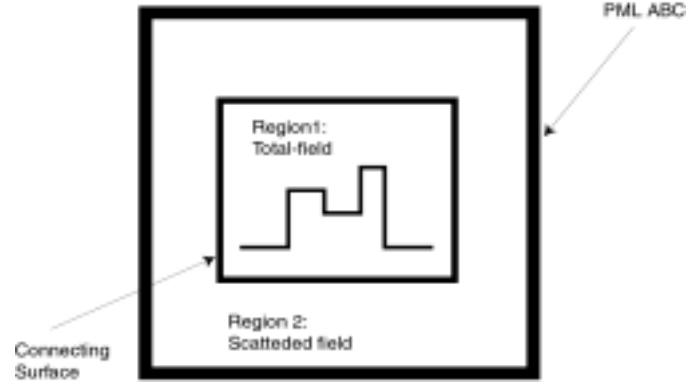


Figure 4.7 FDTD total/scattered field formulation schematics

Figure 4.8 shows the implementation of the connecting condition in two-dimensional TE grid. It is assumed that the total field components $E_{y,tot}$ and $H_{z,tot}$ lie exactly on the total/scattered field interface located at $z = k_0 \Delta z$. To update $E_{y,tot} \Big|_{i,k_0}^n$ by the Yee algorithm, the field values of $H_{x,tot} \Big|_{i,k_0+1/2}^{n+1/2}$ and $H_{x,tot} \Big|_{i,k_0-1/2}^{n+1/2}$ are required. Apparently $H_{x,tot} \Big|_{i,k_0+1/2}^{n+1/2}$ is known and stored in the memory because the grid point $(i, k_0 + 1/2)$ is located in the total field region. However, $H_{x,tot} \Big|_{i,k_0-1/2}^{n+1/2}$ is not available because the grid point $(i, k_0 - 1/2)$ is in scattered field region and only $H_{x,scat} \Big|_{i,k_0-1/2}^{n+1/2}$ is stored in the memory. Yet, knowing that

$$H_{x,tot} \Big|_{i,k_0-1/2}^{n+1/2} = H_{x,scat} \Big|_{i,k_0-1/2}^{n+1/2} + H_{x,inc} \Big|_{i,k_0-1/2}^{n+1/2}, \quad (4.28)$$

we can modify the finite difference expression of Equation 4.11 to achieve consistency when time-marching the E_y components (indicated by solid squares in Figure 4.8) located on the interface

$$E_{y,tot}\Big|_{i,k_0}^{n+1} = E_{y,tot}\Big|_{i,k_0}^n + \frac{\Delta t}{\mathcal{E}(i,k_0)} \cdot \left\{ \left[\frac{H_{x,tot}\Big|_{i,k_0+1/2}^{n+1/2} - H_{x,scat}\Big|_{i,k_0-1/2}^{n+1/2}}{\Delta z} - \frac{H_{z,tot}\Big|_{i+1/2,k_0}^{n+1/2} - H_{z,scat}\Big|_{i-1/2,k_0}^{n+1/2}}{\Delta x} \right] - \frac{H_{x,inc}\Big|_{i,k_0-1/2}^{n+1/2}}{\Delta z} \right\}. \quad (4.29)$$

Including the $H_{x,inc}\Big|_{i,k_0-1/2}^{n+1/2}$ term in Equation 4.29 effectively converts the stored value of the scattered magnetic field $H_{x,scat}\Big|_{i,k_0-1/2}^{n+1/2}$ into a total field quantity, which is required for consistency of both sides of the equation.

The consistency problem also exists for the scattered magnetic field component $H_{x,scat}\Big|_{i,k_0-1/2}$ (indicated by solid triangle in Figure 4.8). Time-marching this component by blindly applying Equation 4.12 yields

$$H_{x,scat}\Big|_{i,k_0-1/2}^{n+1/2} = H_{x,scat}\Big|_{i,k_0-1/2}^{n-1/2} + \frac{\Delta t}{\mu(i,k_0-1/2)\Delta z} \left[E_{y,tot}\Big|_{i,k_0}^n - E_{y,scat}\Big|_{i,k_0-1/2}^n \right]. \quad (4.30)$$

To keep consistency, the incident field must be subtracted from Equation 4.30:

$$H_{x,scat}\Big|_{i,k_0-1/2}^{n+1/2} = \left\{ H_{x,scat}\Big|_{i,k_0-1/2}^{n+1/2} \right\}_{4-30} - \frac{\Delta t}{\mu(i,k_0-1/2)\Delta z} E_{y,inc}\Big|_{i,k_0}^n. \quad (4.31)$$

A similar situation happens on the other three total/scattered field interfaces. The finite difference equations of Yee's algorithm must be modified in order to keep the consistency of the algorithm and simultaneously generate the desired incident wave source. Note that proper treatment of the four interface corner points at $E_y\Big|_{i_0,k_0}$, $E_y\Big|_{i_1,k_0}$, $E_y\Big|_{i_1,k_1}$, and $E_y\Big|_{i_0,k_1}$ (where two adjacent magnetic field components are in scattered field region) is provided by the overlapping operations implied by Equation 4.29.

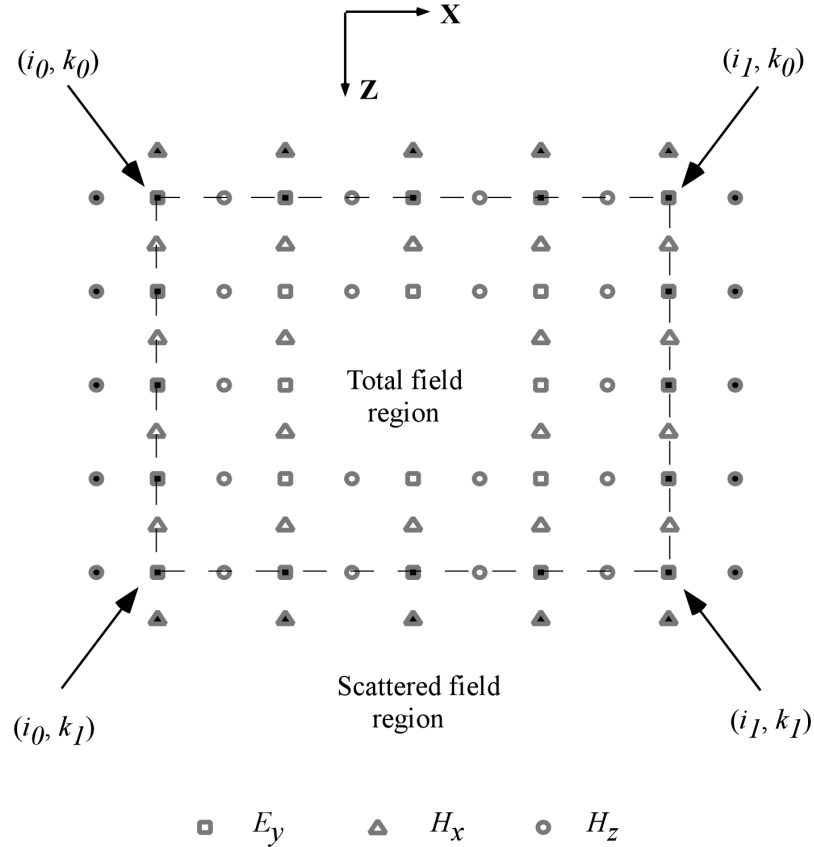


Figure 4.8 Field components in the two-dimensional TE lattice at or near the interface of total and scattered fields used for generating incident wave source

The connecting condition discussed above completely confines the incident wave into the total field region and yet is transparent to the outgoing scattered numerical waves which are free to enter the scattered field region. It is obvious that the values of incident fields at or near the connecting surface are required to implement the connecting condition. A simple one-dimensional auxiliary wave approach can be utilized to calculate these data. In the case of two-dimensional case and normal incidence, the values of E_y at the interface and the values of H_x half space step from the interface are needed. An auxiliary one-dimensional source FDTD grid is placed along the propagating direction of the two-dimensional incident wave (z-axis in normal

incidence). A point hard source is used to excite the one-dimensional source grid and therefore the two-dimensional incident field. The source grid E_y' and H_x' is time-marched using the same space increment Δz and time increment Δt of the two-dimensional TE grid. The values of E_y and H_x of the two-dimensional incident plane wave can be easily interpolated from the one-dimensional source grid. At normal incidence, they are equal to E_y and H_x of the source grid at the corresponding z positions. In this way, there is no need to evaluate large numbers of sinusoidal or exponential functions associated with the incident wave, and more important the numerical dispersion is automatically compensated.

4.3.5 Numerical dispersion

Numerical dispersion arises from the approximation of Maxwell's Equations by a set of finite difference equations, i.e., the Yee algorithm. The physical principle is that the phase velocity of the numerical wave propagating in the FDTD grids can differ from that of the wave actually propagating in the media. This difference, although very small, can cause a lot of numerical problems and therefore is a factor in FDTD modeling that must be accounted for to understand its operation and its accuracy.

Theoretically numerical dispersion can be minimized by using a fine grid in FDTD. However this is practically inefficient because it will greatly increase the computational cost. As mentioned above, the numerical dispersion can be removed by implementing a one-dimensional source grid. The basic idea is simple. The analytic incident wave, which is the solution of Maxwell's Equations, is not an exact solution of the finite difference equations of the FDTD algorithm. If the values of the incident fields are not explicitly assigned according to an analytic expression, but rather calculated as in the case of the 1-D FDTD algorithm, the numerical dispersion can be overcome.

4.3.6 Near to far field transformation algorithm

In DOE analysis and design, very often the far field distribution is interested so that some important parameters such as diffraction efficiency can be determined from that. However, it is practically impossible to directly extend the FDTD computational region to the far field region because of the limitation of the computer resources. Due to the unique feature of the DOE's, it is not computationally efficient to include the final observation plane directly into the FDTD domain even if the near field distribution (for example, twenty wavelength away from the DOE) is desired. This can be easily seen from Figure 4.9. Usually DOE's are in thin slab shape with a much smaller longitude extent (or DOE thickness) and a relatively large transverse extent (or DOE width). Due to the limitation of the fabrication technologies, the etch depth of the DOE's is usually of the order of the optical wavelength at most. So any wavelength-scale extension of FDTD computational region in longitude direction will greatly enlarge the computational region necessary to model DOE structure itself and result in a huge increase in the computational burden.

An efficient way to solve this contradiction is to limit the FDTD computational region to the DOE structure and obtain the near field distribution resulted from the diffraction of the DOE structure. Then a near-to-near or near-to-far field transformation algorithm is employed to effectively propagate the resultant near field to the desired observation plane. On the other hand, the provision of a well-defined scattered field region by the total/scattered field formulation also permits such systematic near-to-near or near-to-far field transformation.

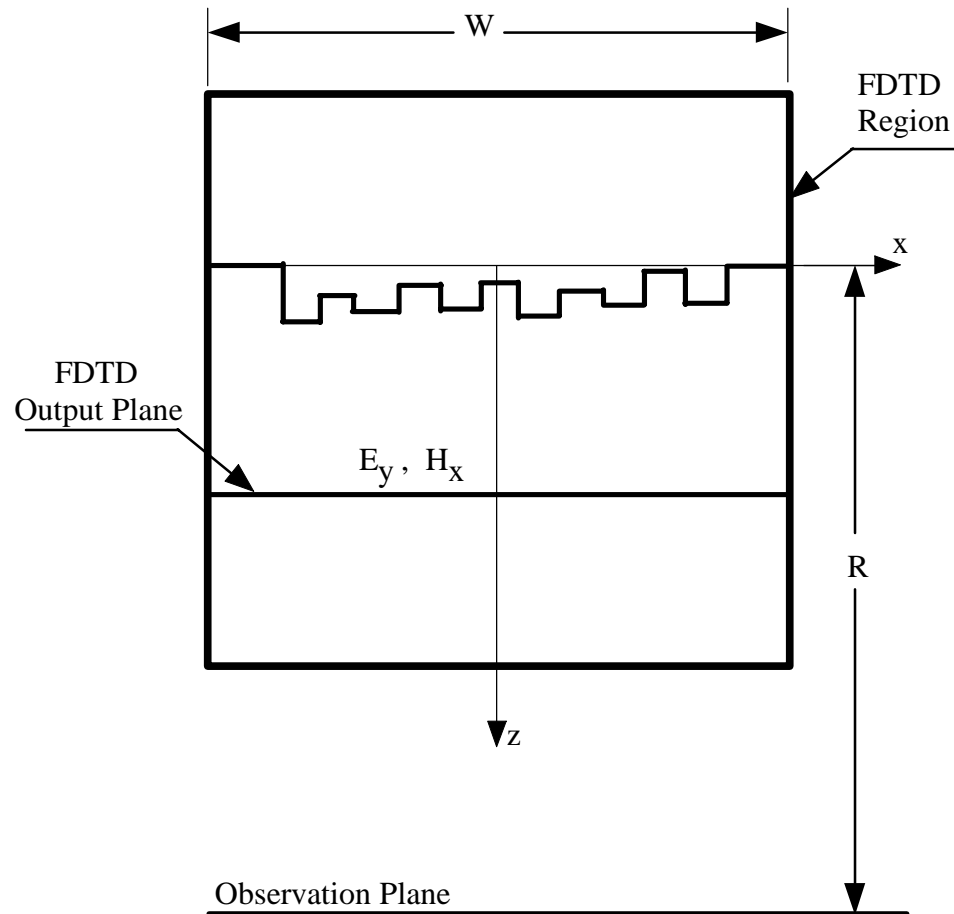


Figure 4.9 Geometry of the FDTD near-to-far field transformation algorithm for FADOE modeling

The Green's function based near-to-far field transformation algorithm [80], [81] is popular in the microwave community. However, it is not suitable to the field transformation problem encountered in two-dimensional FADOE analysis. The main reason is that it is only valid for the far field region in the sense that

$$\frac{R}{W} \gg 1, \quad (4.32)$$

in which W is the width of the FADOE and R is the distance between the FADOE and the observation plane. This far field condition is not always true in DOE analysis. Another concern is that it is computationally expensive compared to the field propagation algorithm available in the optics community. To this end, the vector plane wave spectrum (VPWS) [82] is found to be perfect for field propagation in two-dimensional FADOE analysis.

The VPWS approach is similar to the standard scalar plane wave spectrum [24]. In the two-dimensional TE case shown in Figure 4.9, the propagation must be carried out for both tangential components E_y and H_x on the FDTD field output plane, instead of E_y alone as in the scalar plane wave spectrum. From Maxwell's Equations, it is straightforward to show that the field on the observation plane can be expressed as

$$E_y(x, z = z_p) = \int_{-\infty}^{\infty} F_y(k_x) \exp(-j(k_x x + k_z z)) dk_x, \quad (4.33)$$

$$H_x(x, z = z_p) = \frac{-1}{2\pi\mu c} \int_{-\infty}^{\infty} F_y(k_x) \frac{k_z}{k_0} \exp(-j(k_x x + k_z z)), \quad (4.34)$$

in which

$$F_y(k_x) = \int_{-\infty}^{\infty} E_y(x, z = z_0) e^{jk_x x} dx \quad (4.35)$$

is the plane wave spectrum of E_y component on the FDTD output plane. With these field components, the z component of the complex Poynting vector for TE case can be written as

$$S_z = \frac{1}{2} E_y H_x^*, \quad (4.36)$$

and the intensity distribution on the observation plane is given by

$$I = \text{Re}\{S_z\}. \quad (4.37)$$

The vector plane wave spectrum approach is exact for any distance after the output plane and is very efficient because of the usage of fast Fourier transform.

4.3.7 Apply FDTD algorithm onto the analysis of two-dimensional FADOE's

A powerful and efficient two-dimensional FDTD software package for analysis and design of FADOE's can be developed by integrating the detailed FDTD algorithms discussed above. However unique features of two-dimensional FADOE's must be considered and some modifications must be made.

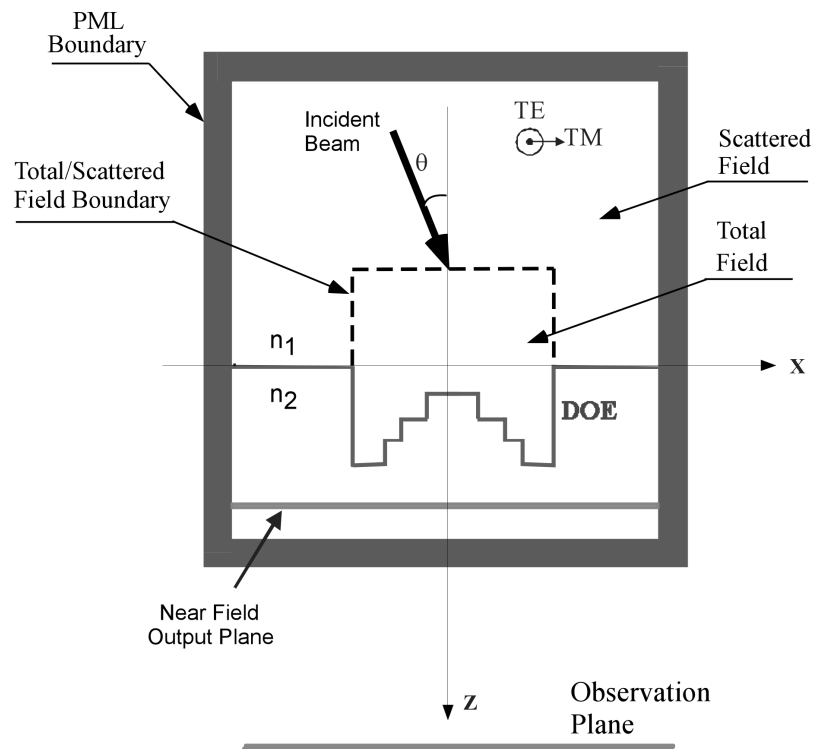


Figure 4.10 Schematic representation of FDTD geometry on FADOE analysis

Figure 4.10 illustrates the overall geometry of FDTD algorithm for analysis of FADOE's. The FADOE is totally embedded in the FDTD computational grid. The refractive

indices of the incident media and DOE substrate are assumed to be n_1 and n_2 respectively. On the outside boundaries of the FDTD computational grid, Berenger's ABC's backed up by perfect electrical conductors (PEC) are used to truncate the entire computation region and to simulate the propagation of the field to outer open space. Because of the negligible reflection error caused by PML ABC, the PML ABC's can be placed only a few cells away from the DOE interface in the longitude direction (or z direction), which greatly reduces the computation region and hence the computation load. While in the x direction, the PML ABC's must be put at least two wavelengths away from the left and right edge of the FADOE to leave enough space for the diffracted field from FADOE. Because the diffracted field is localized around the FADOE, this amount of space is enough for it to attenuate to a negligible degree.

To excite the FDTD grid, the total/scattered field formulation is employed to introduce the incident plane wave for both TE and TM with arbitrary incident angle θ . As shown in Figure 4.10, the formulation is slightly modified here. Only three interfaces are needed to define the total field region because physically the incident field only exists in the incident media while in the DOE substrate only transmitted and diffracted fields exist. Since there is no incident field in the substrate, the substrate region can be automatically treated as total field region.

After the steady state is reached, the field amplitude and phase information on the near field output plane (just past the FADOE interface) can be extracted by a simple temporal Fourier transformation operation [80]. Then the vector plane wave spectrum is used to propagate the field to the observation plane.

It is worthy to point out that if the incident angle $\theta = 0$ and the DOE profile is symmetric about z-axis, the FDTD algorithm can be only applied to half of the DOE structure. The field distribution in the other half can be obtained by symmetry so that the FDTD computation can be reduced to half.

4.3.8 Validation of the two-dimensional FDTD algorithm

A dielectric circular cylinder scattering problem [75] is chosen to validate the developed FDTD algorithms. As shown in Figure 4.11, a TE polarized uniform plane wave with unit amplitude is incident normally on a lossless dielectric circular cylinder of radius a . The relative dielectric constants of the incident medium and the cylinder are 1 for free space and ϵ_r , respectively. The scattered field distribution on the plane with z distance from the center of the cylinder is observed. Analytical solution can be found for this scattering problem [75].

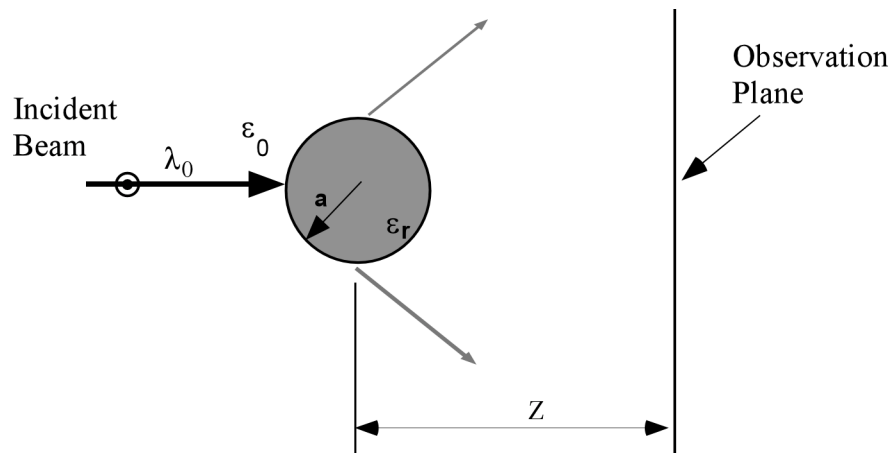


Figure 4.11 Geometry of a dielectric circular cylinder scattering under TE illumination

On the other hand, this problem also can be easily solved numerically by the FDTD method. To do that, the parameters are set to $\lambda_0 = 1.0\mu\text{m}$, $a = 0.5\mu\text{m}$, $\epsilon_r = 2.0$. The observation distance is set to $2.1\mu\text{m}$. The FDTD calculated electric field distribution on the observation plane is compared with the analytical result in Figure 4.12. The excellent agreement between them verifies the proposed FDTD algorithms.

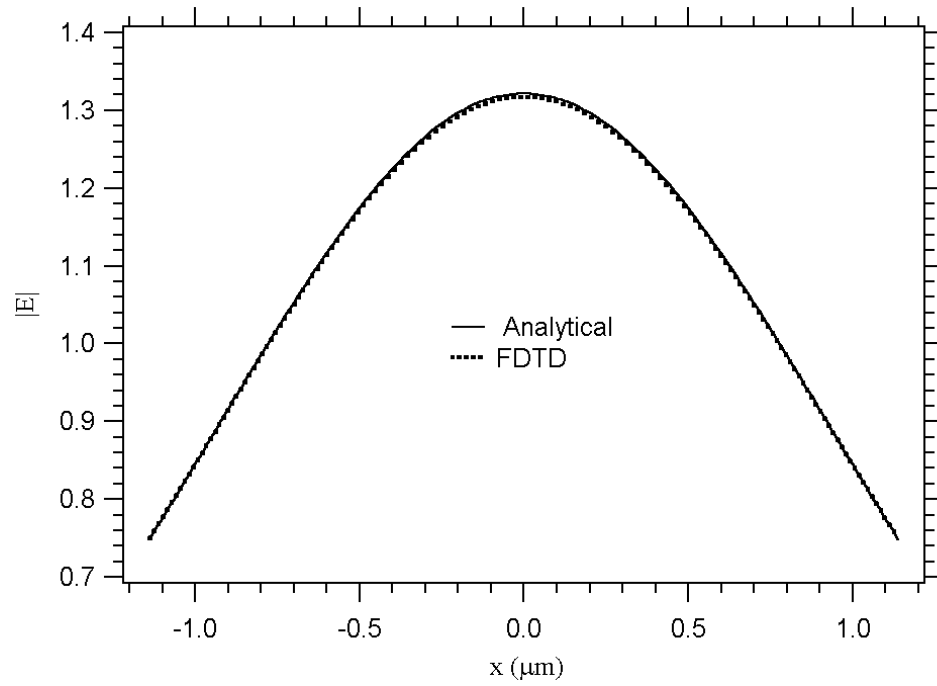


Figure 4.12 Comparison between the FDTD and analytical results on a dielectric circular cylinder scattering problem

Chapter 5

OPTIMIZATION METHODS

In Chapter 4, an efficient and powerful two-dimensional FDTD algorithm for rigorously analyzing FADOE's has been developed. However, it is not enough for synthesis or design of FADOE's. As pointed out in Section 2.3.4, an additional optimization method is required to achieve optimal design, which is the topic of this chapter.

According to their search capability, the optimization methods generally can be classified into two categories: local and global optimization methods. Local optimization methods, such as gradient-based search algorithms, can only search the neighborhood of the starting point in the problem solution space. Though they are computationally efficient and converge rapidly, the success of their operation must rely on highly educated initial guesses near the optimal solution. This strict restriction limits their applications in the area of DOE optimization because usually the solution space associated with DOE design problems is multi-modal so that to find a good initial guess is almost as hard as to find the global optimum of the solution itself. In contrast, global optimization methods do not depend on their initial choice of the problem parameters and are well suited for the optimization of DOE's. Nevertheless, because of their global search nature, the computational cost of global optimization methods may become extremely high.

The most common optimization method employed in DOE design is simulated annealing (SA) [51], [53], [83], [84]. In 1983, Kirkpatrick [85] introduced SA for the general purpose of optimization and its application in DOE design started to appear [83] in 1989. Prather *et al.* [53] first applied SA onto the synthesis of finite aperiodic sub-wavelength DOE's. SA is briefly reviewed in Section 5.1. Another possible global optimization method for DOE design is genetic

algorithms (GA's) [86], [87], [88]. GA's were invented by Holland [89] in the 1960s and were developed by Holland and his students and colleagues. In 1995, Johnson [86] first introduced GA's into the DOE design area and mainly applied it to the scalar domain DOE design. In his work, an advanced genetic algorithm, termed micro-GA (μ GA) [90], was adopted, in which a small population size is used compared to that of conventional GA's. In this dissertation, the μ GA has been successfully applied to the design of FADOE's for the first time. Section 5.2 is devoted to GA's where the salient features of GA's are discussed. A brief illustration of some commonly used genetic operations is also presented. Then the structures of the standard GA's and μ GA's are compared in Section 5.2.3. In the end, the implemented μ GA is applied to the searching of the global minimum of a 100 variable multi-modal test function, which illustrates its validity.

5.1 Simulated annealing (SA)

Simulated annealing is a probabilistic based optimization method, which is modeled after the Maxwell-Boltzman distribution theory in statistical mechanics. In SA, optimization starts from an arbitrary selected solution candidate, which will be randomly perturbed according to some predetermined distribution function to generate a series of potential candidates. The objection function of a candidate is evaluated. If the performance is improved, the candidate is unconditionally accepted. However, if the performance worsens, the candidate will be accepted with some probability governed by the Maxwell-Boltzman distribution:

$$P(\Delta E, T) = \exp(-\Delta E / T), \quad (5.1)$$

where T is the equivalent system temperature and ΔE is the change of the objection function. Though this acceptance possibility may be small, it allows SA to avoid stagnating to sub-optimal. As the iterations go on, the system "temperature" decreases so that the probability that the deteriorating candidates will be accepted decreases as well. And theoretically the SA algorithm

will converge to the global optimum in the end of the iteration. The key point of SA is to choose a proper cooling schedule that can navigate the system to its minimum state and therefore, the global optimum of the solution.

5.2 Genetic algorithms (GA's)

Like SA, genetic algorithms are also probabilistic based optimization methods. However, GA's are patterned after natural evolutionary process, i.e., survival of the fittest, and work on a set of candidate solutions called population instead of single candidate in SA. Though GA's have been around for only thirty years, they have been used in a wide variety of optimization problems, including numerical optimization and such combinatorial optimization problems as circuit layout and job-shop scheduling. Because of their success in these areas, GA's have already established their positions in the field of optimization and searching. Interest in GA's has been growing rapidly in recent years among researchers in many disciplines. Nevertheless, it is noteworthy to recognize that GA's are far from being an established science because even the mathematic mechanisms of many basic operators of GA's still need to be better understood. In this section, the terminologies and several general features of GA's are first briefly reviewed. Then some basic operations of GA's are presented without going into theoretical principles. More detailed material on GA's can be found in several books on GA's [14], [91], [92], [93].

5.2.1 Overview of GA's

Ironically there is no rigorous definition of "genetic algorithm." It can only be said that most methods called "GA's" have at least the following elements in common: coding of the problem parameters, populations of chromosomes, selection according to fitness, crossover to generate new offspring, and/or random mutation of new offspring.

GA's works on an encoding of the problem parameters, instead of directly on the parameters. Analogous to natural genetics, the encoded parameters are called genes. The possible feature values of each gene are called alleles, which may be floating point numbers or discrete ones spanned in its defined domain. A chromosome is a string of all encoded genes of the problem, which represents a point in the search space of candidate solutions. Most often the GA requires a fitness function that assigns a score (fitness) to each chromosome. The fitness of a chromosome depends on how well that chromosome solves the problem at hand.

The GA processes populations of chromosomes (or individuals), by successively replacing one such population with another through a series of genetic operations, such as selection and crossover. Each iteration of this process is called a generation. A GA is typically iterated for anywhere from 50 to 500 or more generations. The entire set of generations is called a run. At the end of a run there are often one or more highly fit chromosomes in the population. Since randomness plays a large role in GA's, two runs with different random-number seeds will generally converge to different final results, which means that GA's are initial population dependent. Note this contradicts the ideal definition of global optimization methods to which GA's belong. Ideally, the optimized results of global optimization methods (i.e., the global optimum of the solution space) should be independent of the choice of the starting point of the optimization process. This contradiction is caused by the finite population size and finite generations employed in practical GA implementations. On the other hand, this contradiction shows an important feature of practical GA's in that GA's are strong at global search while weak at local search. They can quickly locate the region that the global optimum may exist in the solution space but cannot efficiently search that region for the global optimum. Some special considerations must be taken to enhance the local search capability of GA's so that their algorithm robustness can be improved. This can be realized by either implementation of some special genetic operator such as the 'creeping' operator [93] adopted in this dissertation or incorporation of local search algorithms such as hill climbing.

Although there are a lot of successful applications of GA's, they are not necessarily suitable for all optimization problems. Unfortunately, at present GA researchers cannot give a clear guide on the GA's application domain. A rule of thumb is that if the solution space of the specific problem is very large, not smooth and unimodal, or is not well understood, GA's have a good chance to be applicable and outperform other optimization methods. The problem considered herein, the optimization of FADOE's, is a typical example of such a problem. However a GA's performance will depend very much on details of the particular implementation such as the method for chromosome encoding, the choice of the genetic operators and their parameter settings. Some basic genetic operations needed for common GA implementations are introduced in the following.

5.2.2 Basic genetic operations

In this section, some basic genetic operations are illustrated. For most operations, several different methods are presented, because the performances of these methods are usually problem sensitive. Therefore different combinations of these operations may be tried to find out the best one for a specific problem.

5.2.2.1 Chromosome encoding

Chromosome encoding is a set of mechanisms to map the problem parameters to gene positions in a chromosome with finite length. Because of the historical reason, the binary encoding is the most widely used encoding method, in which the parameters are encoded into a chromosome with binary digits (1 or 0). For example, consider the minimization problem of a simple function

$$f(x) = x^2, \quad (5.2)$$

with x defined in the range $[-2, 2]$. If the required precision is the fourth digit place after the decimal point, the implication is that the range $[-2, 2]$ must be divided into at least

4·10000 uniform sub-ranges. This means that 16 bits are required as a binary string. The mapping from a binary chromosome (string) $\langle b_{15} \cdots b_0 \rangle$ into a real number in the range $[-2, 2]$ is straightforward and can be completed in two steps:

- Convert the binary string $\langle b_{15} \cdots b_0 \rangle$ from the base 2 to base 10 by

$$\left(\langle b_{15} \cdots b_0 \rangle \right)_2 = \left(\sum_{i=0}^{15} b_i \cdot 2^i \right)_{10} = x', \quad (5.3)$$

- Find a corresponding real number x by

$$x = -2.0 + x' \cdot \frac{4}{2^{16} - 1}. \quad (5.4)$$

Binary encoding is unnatural and unwieldy for many problems such as the above example. Recent work demonstrated that other encoding methods such as real-valued and multiple-character encodings have shown better performance than binary encoding on many problems, which is still a controversial issue because Holland's schema theory [89] predicts that GA's should exhibit better performance on binary encoding. At present there are no rigorous guidelines for predicting which encoding will work best. However, Davis [92] advocates using whatever encoding is the most natural for the specific problem. This might be the best philosophy until the theory of GA's and encodings is better formulated.

5.2.2.2 Parent Selections

After deciding on the encoding method, the second decision to make in GA implementation is how to perform selection, that is, how to choose the individuals in the current population as parents who will create offspring for the next generation. The purpose of selection is to emphasize the fitter individuals in the population in hopes that their offspring will in turn have even higher fitness. There are two important issues in the evolution process of GA: population diversity and selective pressure. These factors are strongly related: an increase in the selective pressure decreases the diversity of the population and vice versa. In other words, strong

selective pressure will inevitably result in the premature convergence of the GA's; a weak selective pressure can make the search ineffective. So it is critical to choose a right selection method and its parameters so that a balance between these two factors can be achieved. As was the case for encoding, numerous selection methods have been proposed; three of them are discussed here.

The first method is fitness proportionate selection originally used by Holland [89], in which the selection probability of each individual is defined as the fraction of its fitness in the total summation of the fitness of the whole population:

$$P(\vec{x}_i) = \frac{F_i}{\sum_{j=1}^N F_j}, \quad (5.5)$$

in which $P(\vec{x}_i)$ is the probability of i th individual being selected as the parent of the next generation and F_i is the its fitness value and N is the population size. The most common implementation of this method is the "roulette wheel" approach. In this approach, each individual is assigned a slice of a circular "roulette wheel," the size of which is proportional to the individual's fitness. The wheel is spun for N times and on each spin the individual under the wheel's marker is selected to be in the pool of parents for the next generation.

Although fitness proportion selection is intuitively simple, it has several problems, mainly the premature convergence caused by its high selection pressure in the early stage of the evolution. Furthermore, it is not suitable to GA's with small population size, especially the μ GA, because in such cases the actual selection probabilities calculated by Equation 5.5 are far from their expected values, which makes them meaningless.

An alternative selection method is rank selection. In this selection method, the individuals in the current population are first ranked according to their fitness values, then the selection probability of each individual is assigned according to its rank rather than its absolute fitness

value. Michalewicz [91] introduced two ranking probability functions. One is linear and defined as

$$prob(\bar{x}_i) = q - (rank_i - 1)s, \quad (5.6)$$

in which $rank_i$ is the rank of i th individual and q is a user defined, population size dependent parameter. s is a parameter necessary to fulfill the requirement of

$$\sum_{i=1}^N prob(\bar{x}_i) = 1. \quad (5.7)$$

The other function is a nonlinear one defined as

$$prob(\bar{x}_i) = \frac{1}{1 - (1 - q)^N} q(1 - q)^{rank_i - 1}, \quad (5.8)$$

in which q is also a user defined, but population size independent parameter. In both cases, a single parameter q can control the selective pressure of the algorithm such that large q values impose stronger selective pressure.

However, the above rank selection methods are not suitable to μ GA either because of the same reason mentioned earlier. In this dissertation, a new rank selection method, the deterministic rank selection, is developed especially for μ GA. In deterministic rank selection, the parents of the new individuals are completely determined by the rank of the old population. For example, the parents of first new individual are No. 1 and 2 individuals in the rank and those of the second are No. 1 and 3 and so on.

In rank selection, the absolute differences in fitness between individuals are obscured by ranking process. This discarding of absolute fitness information could have advantages and disadvantages. It standardizes the GA process for all kinds of problems and keeps the selection pressure very well during various stages of the GA evolution. However, in some cases, it might be useful to know that one individual is far fitter than others. Moreover, selection by rank violates the schema theorem, which ensures the convergence of the GA.

The last selection method is tournament selection, which combines the idea of ranking in a very interesting and efficient way. Two individuals are randomly chosen and a random number r in the range $[0, 1]$ is then generated. If r is less than w , a predetermined winning probability, the one with higher fitness value is selected to be parent; otherwise the less fit one is selected. The two are then returned to the original population and can be selected again.

Tournament selection is similar to rank selection in terms of selection pressure. Also it is computationally more efficient for GA's with larger size of population.

5.2.2.3 Offspring breeding

In implementing a GA, once the parent selection is completed, the third decision is how to breed offspring from the selected parents. The main operation for offspring breeding is crossover, in which segments of the selected parent chromosome are combined to form new ones. Crossover is the major distinguishing feature of the GA's. The intuition behind the crossover is information exchange between different potential solutions.

Suppose the two selected parent chromosomes are

$$\bar{x}_1 = (a_1, a_2, \dots, a_n) \quad (5.9)$$

and

$$\bar{x}_2 = (b_1, b_2, \dots, b_n), \quad (5.10)$$

two new offspring chromosomes can be created from them by a single-point crossover operator

$$\left\{ \begin{array}{l} (a_1, a_2, \dots, a_c, a_{c+1}, \dots, a_n) \\ (b_1, b_2, \dots, b_c, b_{c+1}, \dots, b_n) \end{array} \right\} \Rightarrow \left\{ \begin{array}{l} (a_1, a_2, \dots, a_c, b_{c+1}, \dots, b_n) \\ (b_1, b_2, \dots, b_c, a_{c+1}, \dots, a_n) \end{array} \right\}, \quad (5.11)$$

in which c is the randomly selected crossover point. Similarly, if two crossover points are selected, we will have a two-point crossover operator, which can form offspring chromosomes that cannot be realized by a single-point crossover, such as

$$\left\{ \begin{array}{l} (a_1, \dots, a_{c_1}, a_{c_1+1}, \dots, a_{c_2}, a_{c_2+1}, \dots, a_n) \\ (b_1, \dots, b_{c_1}, b_{c_1+1}, \dots, b_{c_2}, b_{c_2+1}, \dots, b_n) \end{array} \right\} \Rightarrow \left\{ \begin{array}{l} (a_1, \dots, a_{c_1}, b_{c_1+1}, \dots, b_{c_2}, a_{c_2+1}, \dots, a_n) \\ (b_1, \dots, b_{c_1}, a_{c_1+1}, \dots, a_{c_2}, b_{c_2+1}, \dots, b_n) \end{array} \right\}, \quad (5.12)$$

in which c_1 and c_2 are two crossover points. We can go further to multiple-point and even uniform crossover. With uniform crossover, for each gene of the offspring chromosome, it decides (with certain probability p) which parent will contribute its allele to that gene. For example, for $p=0.5$, the uniform crossover may produce a pair of offspring as

$$\left\{ \begin{array}{l} (a_1, a_2, a_3, a_4, a_5 \dots, a_n) \\ (b_1, b_2, b_3, b_4, b_5 \dots, b_n) \end{array} \right\} \Rightarrow \left\{ \begin{array}{l} (a_1, b_2, a_3, b_4, a_5 \dots, b_n) \\ (b_1, a_2, b_3, a_4, b_5 \dots, a_n) \end{array} \right\}. \quad (5.13)$$

For real-valued encoding, it is feasible to define some other crossover operators. One of them is called arithmetical crossover. If \bar{x}_1 and \bar{x}_2 are to be crossed parent chromosomes, the arithmetical crossover will result in two offspring as

$$\bar{x}'_1 = a \cdot \bar{x}_1 + (1-a) \cdot \bar{x}_2 \quad (5.14)$$

$$\bar{x}'_2 = (1-a) \cdot \bar{x}_1 + a \cdot \bar{x}_2, \quad (5.15)$$

in which a is a parameter, which could be either a constant (uniform arithmetical crossover), or a variable whose value is changed with the generation of the population (adaptive arithmetical crossover) or a random number between 0 and 1 (random arithmetical crossover). It is noticed that arithmetical crossover always searches toward the midpoint of \bar{x}_1 and \bar{x}_2 , which is not guaranteed to be the most promising direction.

To avoid this, Wright [94] proposed a new crossover method called the heuristic crossover. In this operator, the fitness values of selected parents are utilized to determine the searching direction. Namely, for two parents \bar{x}_1 and \bar{x}_2 , if parent \bar{x}_1 has a higher fitness value, then the heuristic crossover will generate a single offspring \bar{x}' according to

$$\bar{x}' = \bar{x}_1 + r \cdot (\bar{x}_1 - \bar{x}_2), \quad (5.16)$$

in which r is a random number between 0 and 1. However, it is not difficult to find out that heuristic crossover is always searching towards the two ends of the definition ranges of the genes, which is not always efficient either.

From the above discussion, we can see that the arithmetical crossover and heuristic crossover are complementary in the searching directions. As a result the search capability of GA should be improved if these two crossover operators are used alternatively. This can be easily realized in the implementation of GA's: the choice of the crossover operator is determined by a random number r in $[0, 1]$; if $r < 0.5$, the arithmetic crossover is selected, otherwise heuristic crossover is then selected.

5.2.2.4 Mutation

In a mutation operation, first a gene is randomly selected with some predetermined probability of mutation rate, which is usually very small. Then the gene will be altered either arbitrarily or according to some rule. The intuition behind the mutation operator is the introduction of some extra variability into the population. In the earlier stage of a GA run, such extra variability prevents the premature loss of diversity of a gene and provides an "insure policy" against particular allele stagnation of a gene, whereas in the later stage of optimization mutation it performs the fine-tuning of the candidate solutions, which is critical for achieving an optimum solution. Compared to selection and crossover, mutation plays a decidedly secondary role in the operation of GA's [14].

5.2.2.5 Elitism

Elitism was first introduced by De Jong [95]. In this operation, the best chromosome found so far is directly copied into the population of the next generation without going through any other operations. This will keep the best chromosome intact and ensure that the next

generation will produce a chromosome as good as or even better than the present best chromosome. In most cases elitism can significantly improve the converging speed of the GA's.

5.2.3 Structures of GA's

With the above basic elements at hand, it is possible to implement different kinds of GA's. One main kind is the conventional GA's with a relative large population size (usually 100). A simple GA (SGA) proposed by Goldberg [14] only used selection, crossover and mutation operators, the structure of which is shown in Figure 5.1. However, the conventional GA's are not suitable to the FADOE's design problem because of their large population size. Since for every generation each individual in the population must be evaluated in terms of fitness values, large population size means many times of evaluation of fitness function. In the rigorous FADOE design, the performance of the candidate profiles (which must be encoded into chromosomes or individuals of course) is evaluated by a 2-D FDTD algorithm, which is computationally intensive. Many times of using the FDTD algorithm would result in a prohibitive computational load, even for powerful modern workstations. This the main reason for the failure of the previous attempt of applying GA to FADOE's design [96].

On the contrast, there is another kind of GA termed a micro-GA (μ GA) [15], or serial GA [91], in which a small population size (usually 5) is used. Because of the small population feature, μ GA is well suited to the FADOE design and is adopted in this research. μ GA involves the same genetic operations as the conventional GA's, but puts them in a different structure. Figure 5.2 illustrates the structure of a typical μ GA. In μ GA, a series of conventional GA processes with a small population is carried out successively. In each conventional GA process, premature convergence (non-optimal result) is inevitable because of the small population size. However, this result can be treated as local optimum. To achieve global optimum, we can restart the GA search process from this local optimum. So a new generation is reproduced in the way

that the best individual is retained and the others are re-initialized either randomly or by mutating the best one. This new population is passed to the next GA process for searching even better local optima. Overall, μ GA achieves global optimum step by step by finding local optima with a series of small population conventional GA processes.

```

Randomly initialize a population (usually size of 100)
For (gen=1:Max_generation)
{
    Decode the chromosomes (if necessary)
    Evaluate fitness function
    Reproduce population of next generation
    {
        Select parent chromosomes
        Crossover selected parents
        Mutate crossover-generated new chromosomes
    }
}

```

Figure 5.1 Structure of a typical simple conventional GA

```

Randomly initialize a population (usually size of 5)
For (gen = 1:Max_generation)
{
    While (not converged)
    {
        Decode the chromosomes (if necessary)
        Evaluate fitness function
        Reproduce population of next generation
        { Select parent individuals
          Crossover selected parents
        }
    }
    Restart  $\mu$ GA
    { Retain the best individual
      Re-initialize others randomly or by mutating the best
    }
}

```

Figure 5.2 Structure of a typical μ GA

5.2.4 Validation of the implementation of μ GA

A sample function was used to validate the implementation of the proposed μ GA. The function is a modified version of De Jong F3 function [14], which is defines as

$$f(x_1, x_2, \dots, x_n) = \sum_{i=1}^n |\text{int}(x_i)|, \quad (5.17)$$

in which the $\text{int}(x_i)$ function truncates the integer part of a float number x_i . A 2-D image plot of the function with two variables ($n=2$) defined in $[-5.12, 5.12]$ is shown in Figure 5.3. As clearly indicated in the figure, the truncation function results in lots of plateaus into the function. This functional roughness makes the minimization problem difficult and will force most of the optimization methods to local minima.

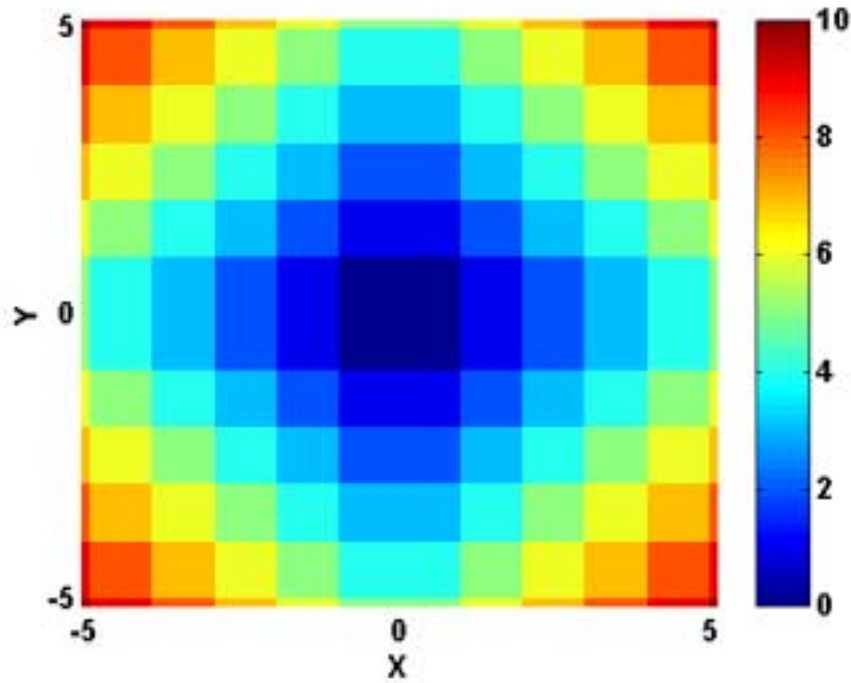


Figure 5.3 2-D image plot of a modified De Jong F3 function

To test the optimization capability of μ GA, 100 variables were used with the definition range of $[-5.12, 5.12]$. Binary encoding and float encoding were compared under the same configurations of μ GA (rank selection, uniform crossover). In binary encoding, 10 binary bits were used for encoding each variable, which achieved an accuracy of 0.01 for each variable and resulted in a chromosome with length of 1000 bits, compared with 100 in float encoding. Figure 5.4 shows typical convergence curves for both encoding methods. It is evident that float encoding is more effective than binary encoding on this problem.

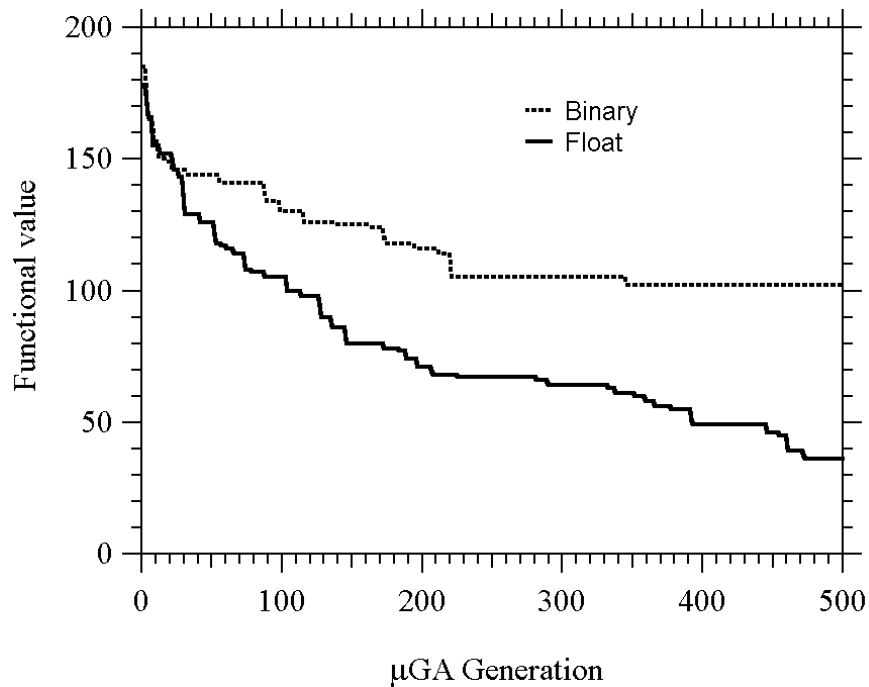


Figure 5.4 Comparison of binary and float encoding methods on the sample function with 100 variables

Additionally, comparisons were also made for three types of crossover operations for float encoding, i.e., arithmetical crossover, heuristic crossover and the combination of them. As

demonstrated in Figure 5.5, arithmetical crossover worked best while the other two had similar performances. After about 130 generations of μ GA, it found the global minimum of the function (0). The excellent performance of the arithmetical crossover is expected because the global minimum of this sample function is located at $x_i = 0$, which is exactly the middle point of the definition range. As pointed out in Section 5.2.2.3, arithmetical crossover tends to navigate μ GA to the middle points of the span ranges of the variables. However, for general problems whose global optimum may locate anywhere in the definition domain of its parameters, the combination of the arithmetical and heuristic crossover works best, as will be seen in next chapter.

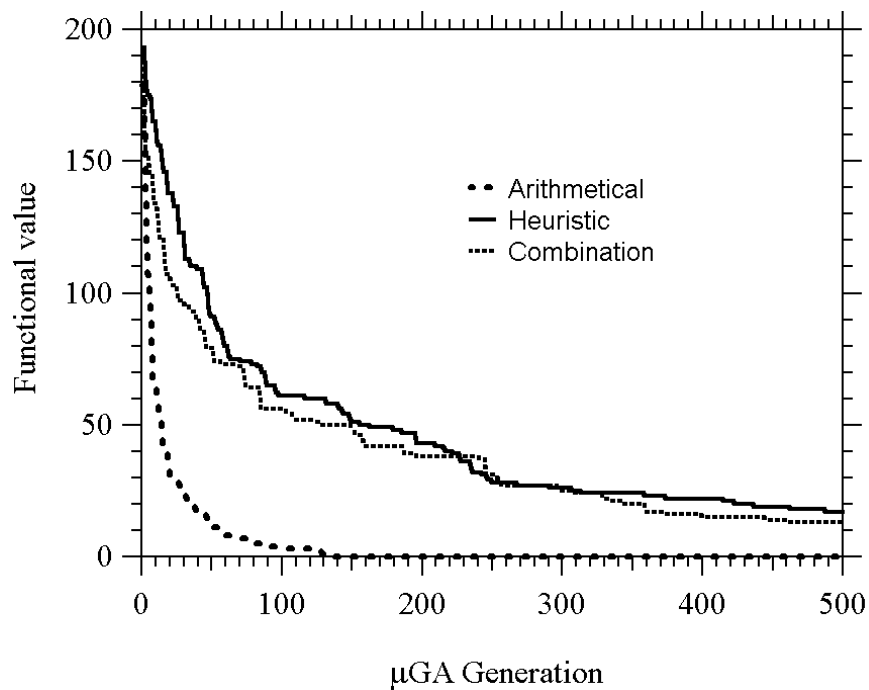


Figure 5.5 Comparison of three types of crossover operations for float encoding on the sample function with 100 variables

Chapter 6

FORMULATION OF μ GA-FDTD RIGOROUS DESIGN TOOL FOR FADOE'S

After the completion of the 2-D FDTD algorithm and the μ GA, it is ready to integrate them into a complete rigorous design tool for FADOE's design. The main task of the integration is to formulate μ GA particularly for the FADOE design problem. Specifically, one must choose an encoding method by which the FADOE profiles can be encoded into chromosomes. Also a fitness function must be developed upon which the performances of FADOE profiles can be evaluated. Such a fitness function must accommodate multiple design constraints so that multi-functional novel devices can be optimized. The detailed formulation of the μ GA-FDTD rigorous design tool for FADOE's is discussed in Section 6.1. In Section 6.2, the performance of the developed μ GA-FDTD design tool is tested on a simple diffractive microlens design case.

6.1 Formulation of the μ GA-FDTD rigorous design tool

In this section, a simple float encoding method for FADOE is first discussed. Then an advanced fitness function is developed to control both the intensity and phase distributions and their uniformities on the plane of interest (observation plane). In the end the overall structure of the μ GA-FDTD design tool is illustrated in the form of pseudo-code.

6.1.1 Encoding of DOE profile

To apply μ GA on the FADOE design, the first step is to encode the FADOE profile into a chromosome. As illustrated in Figure 6.1, this is achieved by uniformly dividing the FADOE

width along the x-axis into N cells, in each of which the etch depth is encoded as a gene. The genes are then combined to form a chromosome, which in turn represents a FADOE profile. We adopt float encoding or real-valued encoding of genes instead of classical binary coding. As mentioned in the previous chapter, there are several advantages of float encoding compared to binary coding. First, no additional encoding-decoding process is required for float encoding; second the length of the chromosome is much shorter to achieve the same precision, and most important, our GA experiences as well as those of other researchers [93] indicate that float encoding outperforms binary coding for complex optimization problems with large numbers of parameters, such as the FADOE optimization problem concerned herein.

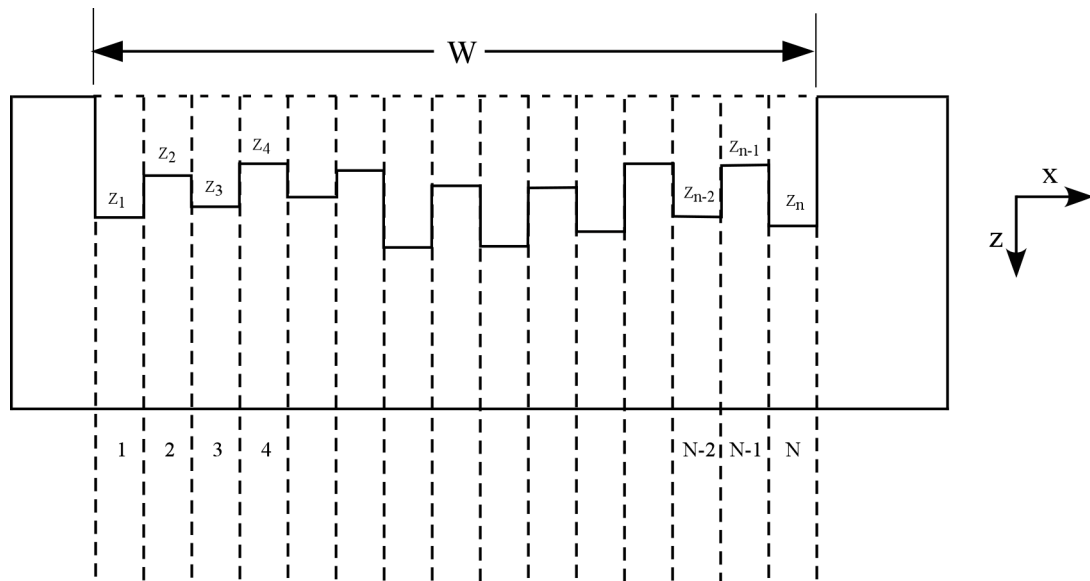


Figure 6.1 μ GA encoding geometry for FADOE's design

6.1.2 Fitness function definition

Once the encoding is accomplished, one must establish a fitness function, i.e., a design metric for the FADOE design problem, with which the performance of a specific DOE profile can be evaluated. In DOE designs, the performance of DOE's is often evaluated by two parameters: diffraction efficiency and uniformity. A flexible and sophisticated fitness function is developed, in which multiple design constraints can be imposed. With this fitness function, not only the intensity and phase distributions of the field on the observation plane but also their uniformities can be controlled. The fitness function can be expressed as

$$\begin{aligned}
 F = & I^{\text{TE}} + I^{\text{TM}} \pm \sum_{j=1}^{M_1^{\text{TE}}} U_j^{\text{I,TE}} \pm \sum_{j=1}^{M_1^{\text{TM}}} U_j^{\text{I,TM}} \pm \sum_{j=1}^{M_1^{\text{TEM}}} U_j^{\text{I,TEM}} \\
 & + P^{\text{TE}} + P^{\text{TM}} \pm \sum_{j=1}^{M_P^{\text{TE}}} U_j^{\text{P,TE}} \pm \sum_{j=1}^{M_P^{\text{TM}}} U_j^{\text{P,TM}} \pm \sum_{j=1}^{M_P^{\text{TEM}}} U_j^{\text{P,TEM}}
 \end{aligned} \tag{6.1}$$

where the I and P terms are constraints on the intensity and the phase respectively for both TE and TM, $\sum_j U_j^{\text{I}}$ and $\sum_j U_j^{\text{P}}$ terms are uniformity constraints on intensity and phase respectively and j runs over the number of regions of interest (M 's) for the fields of TE, TM or between TE and TM. The fitness function defined in Equation 6.1 covers most of the FADOE design problems. For some special design problems, however, the code of fitness definition can always be easily modified.

In Equation 6.1, intensity constraints (I terms) can be imposed by either a target function or a weighting function while phase constraints (P terms) can be imposed by a target function only. In general the target function is the exact intensity or phase distributions required to fulfill the function of the FADOE 's and the constraint can be written as

$$C = \sum_{s=1}^N \alpha_1 \cdot |g(x_s) - g_t(x_s)|, \tag{6.2}$$

where g is the actual intensity or phase distributions resulted by a specific DOE profile and g_t is the desired one; α_1 is a user defined scaling factor; and x_s is the sampled transverse coordinate on the observation plane. C could be I or P terms in Equation 6.1. On the other hand a weighting function can be any function useful to control the desired characteristic of the FADOE and the constraint can be written as

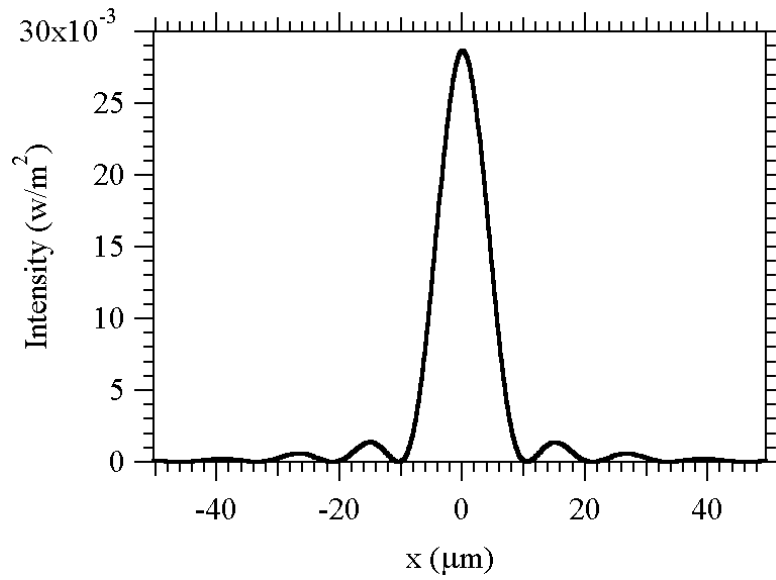
$$C = \sum_{s=1}^N W(x_s) I(x_s), \quad (6.3)$$

where $W(x)$ is the weighting function and $I(x)$ is the actual intensity distribution. Figure 6.2 shows an example of target function and weighting function for a microlens design. Note that weighting function is more flexible than target function because there is no need of a priori about the diffracted field on the observation plane, which is hard to be determined before the design is carried out for most problems. However, target function imposes more stringent constraints than weighting function so that the performance of the resultant design will be closer to the design requirement.

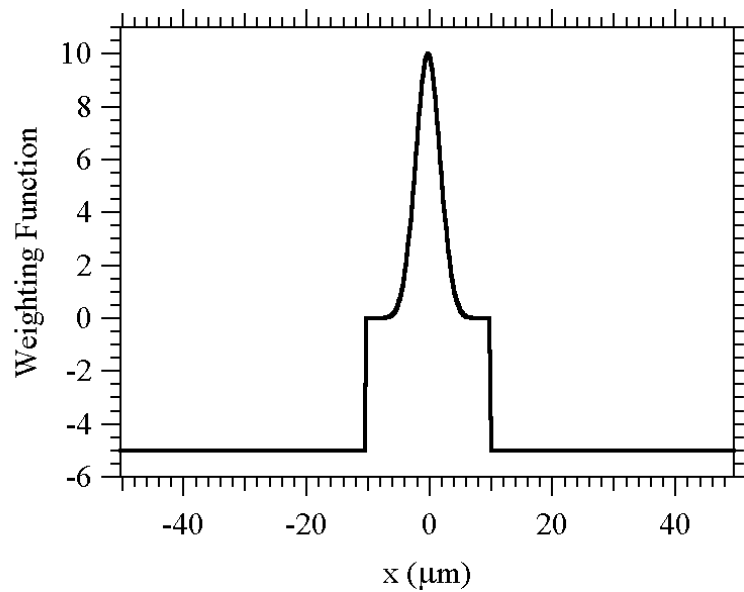
To control the uniformity property of the field distribution, the uniformity constraints (U_j terms) in Equation 6.1 are defined as

$$U_j = \sum_{k=1}^L \alpha_2 \left| g(x_{b_1+k}) - g(x_{b_2+k}) \right|, \quad (6.4)$$

where g is the actual intensity or phase distribution; b_1 and b_2 are beginning points of two equal-length (with length L) interested regions on the observation plane; and α_2 is another user defined scaling factor. Note the uniformity constraints defined by Equation 6.4 are designed only for minimization purpose, so the \pm sign in Equation 6.1 must be properly chose according to the optimization purpose of the problem (+ for minimization and – for maximization of fitness function).



(a)



(b)

Figure 6.2 Sample of target and weighting function of μ GA for a microlens design (a) target function (exact desired intensity distribution on the observation plane) (b) weighting function

6.1.3 Pseudo-code of the whole design tool

Figure 6.3 is the pseudo-code of the μ GA-FDTD design tool. There are two apparent differences between this implementation of μ GA and the traditional implementations of μ GA [50]. First we modified the way to re-initialize the population except for the fittest one (i.e., restart operation) after each μ GA process is converged. In the first half of the generations μ GA is restarted randomly, while in the later generations μ GA is restarted by mutating the fittest individual. In the early generations, the best individual found so far (local optima) may be totally different from the desired global optimum and does not contain much useful information. By randomly restarting, we search for new local optima in different space rather than continue searching around this local optimum so that the convergence speed can be improved. However, in the later generations, ideally the achieved best individual is very close to the global optimum; the job left for optimization is local fine-tuning, which can be realized by mutating the fittest individual. Second, an additional creeping process is carried out after each normal μ GA process to enhance the local search capability of the μ GA-FDTD method. The operations of this creeping process are the same as those of normal ones except the restarting of the population. In the creeping process, the population is restarted by a “creeping” operator [93]. For FADOE design this creeping operator is implemented as follows: the fittest DOE profile is perturbed by the increase or decrease of the etch depth of some randomly selected DOE cells of a unit FDTD grid size in the z direction (ΔZ) to generate the other 4 individuals. With this crept initial population, the creeping process searches the neighborhood of the fittest DOE profile resulted from normal μ GA process and chooses a better point for next μ GA process. This fine-tuning of the intermediate local optima can improve the overall converging speed of the whole design algorithm for most of the design problems we ever carried out.

```

Initialize FDTD algorithm
Randomly initialize  $\mu$ GA population

For (gen = 0:Max_generation)
{ Normal  $\mu$ GA process:
  While (not converged)
  {
    Evaluate fitness values by FDTD
    {Setup DOE profile from each individual;
     Pass to FDTD to get near/far field;
     Compute fitness value.}

    Generate a new generation
    { Pre-process of fitness values if necessary;
      Select parent individuals;
      Crossover parent individuals to get offspring.}
  }

  Restart  $\mu$ GA
  { Retain the fittest individual;
    If (gen < max_generation/2)
      Randomly generate other 4.
    Else
      Mutate the fittest to generate other 4.
    End
  }

  Creeping  $\mu$ GA process:

  Restart  $\mu$ GA.
}

```

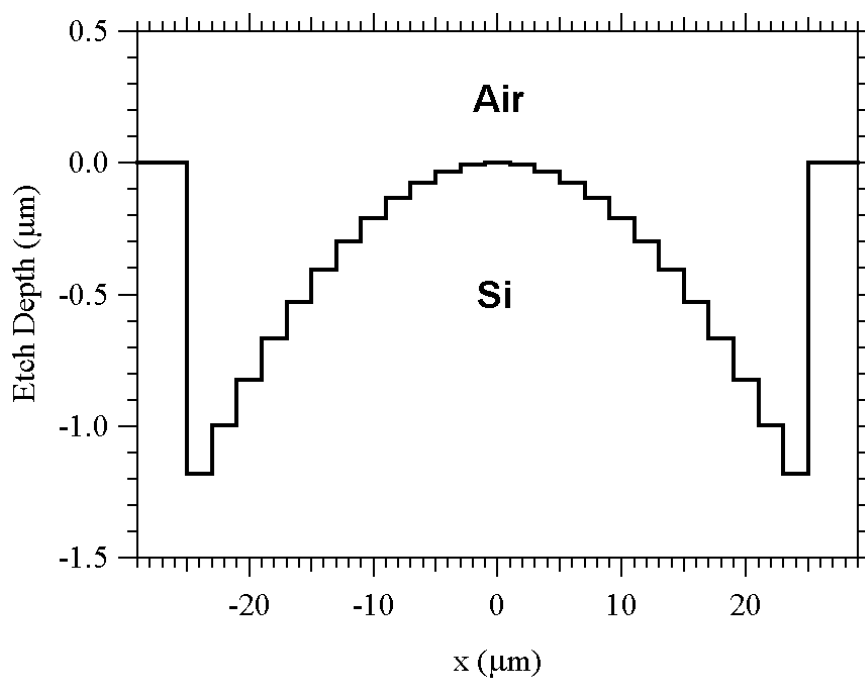
Figure 6.3 Pseudo-code of the μ GA-FDTD rigorous design tool for FADOE design

6.2 Test of the μ GA-FDTD on a diffractive microlens design

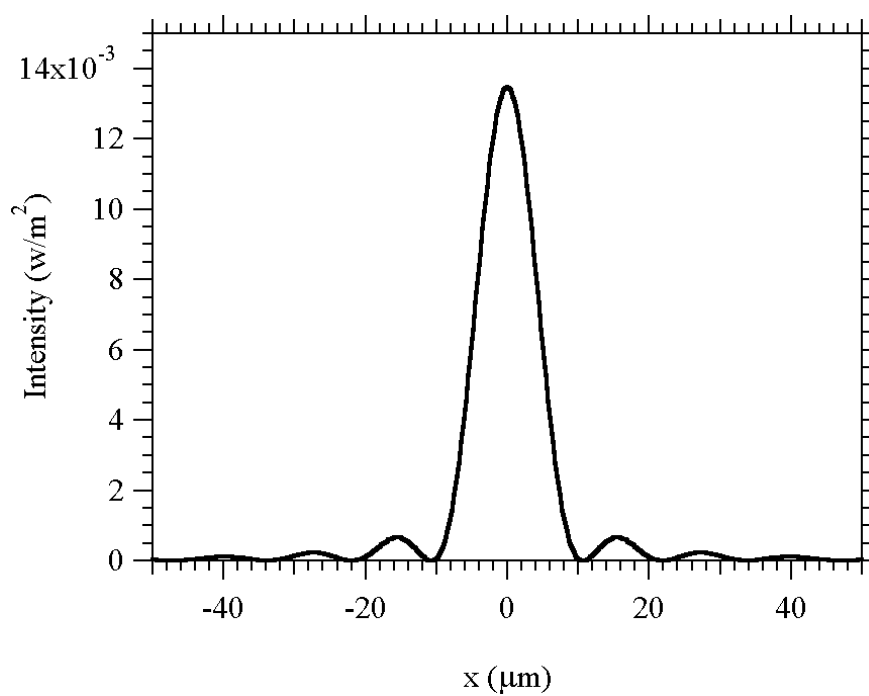
Before applying the μ GA-FDTD to challenging DOE design problems, a simple design example is used to test and validate the algorithm. The example is a diffractive microlens with a focal length of $100\ \mu\text{m}$ and a width of $50\ \mu\text{m}$ (f-number of $f/2$). The microlens is assumed to be etched into a Silicon substrate ($n_1=3.38$) and is illuminated from Silicon at normal incidence by a unit amplitude TE polarized monochromatic plane wave with $\lambda_0=5\ \mu\text{m}$. The exit media is air ($n_2=1.0$). The minimum feature size of the lens is set to $2\ \mu\text{m}$ so that the DOE is divided into 25 cells. The maximum etch depth is set to $1.2\ \mu\text{m}$. Since the float encoding is adopted for μ GA, all optimized microlens profiles presented below are unquantized, even though in the FDTD calculation the profiles are sampled and quantized by FDTD grids with a unit grid size of $\lambda_0/20$ and $\lambda_0/50$ for the x and z directions respectively.

This lens can be designed analytically [49], which results in a continuous quadratic profile as shown in Figure 6.4(a). Figure 6.4(b) shows its intensity distribution on the focal plane. Note both the lens profile and the field distribution are symmetrical about the z-axis, which means this design problem is a physically symmetrical problem. As stated in Section 4.3.7, this symmetry characteristic can be utilized to cut half of the FDTD computation.

Various tests and comparisons have been made for μ GA-FDTD on the design of this microlens. Both target function and weighting function approaches have been employed to impose design constraints through fitness function. Performances of the arithmetical crossover and the combination of arithmetical and heuristic crossover are also compared. Some salient features of the μ GA-FDTD design tool are revealed through these tests and comparisons.



(a)



(b)

Figure 6.4 Analytically designed microlens (a) lens profile (b) intensity distribution on the local plane

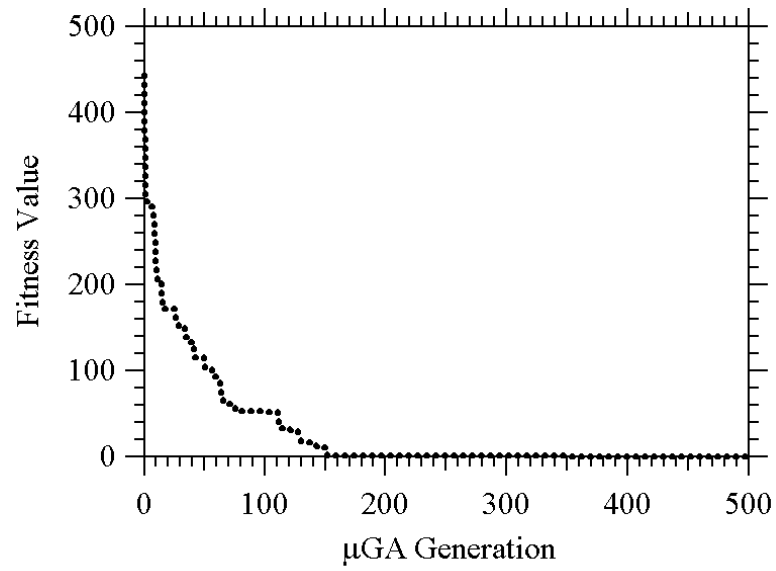
6.2.1 Target function approach

In this test, the target function approach is used to impose intensity constraints in the fitness function. The target function used is the actual intensity distribution resulting from the analytical profile, as shown in Figure 6.4(b). The purpose of this test is to check whether the μ GA-FDTD can duplicate the analytical profile, which obviously is the global optimum for this case. Since only intensity constraint is needed and is controlled by a target function, the fitness function consists of only the first term of Equation 6.1 and can be written in the form of Equation 6.2 with α_1 being constants linearly proportional to the target intensity distribution at sampled points.

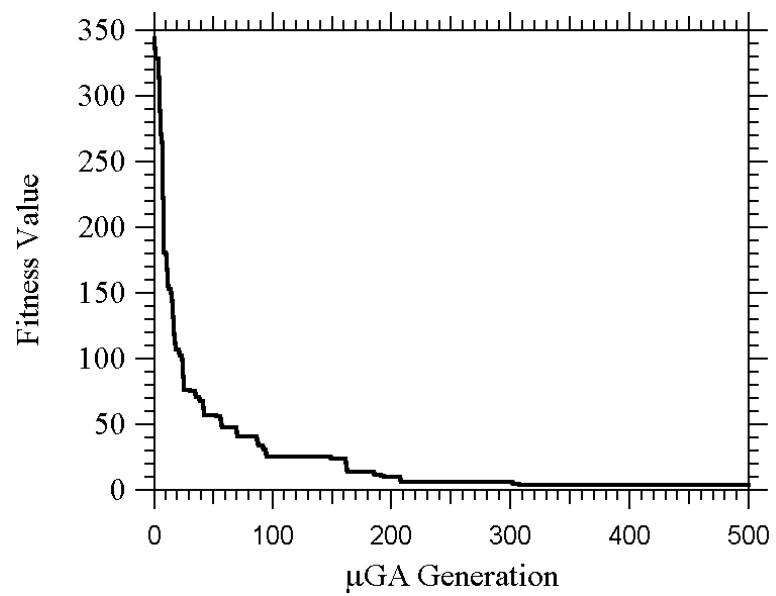
The μ GA-FDTD algorithm starts searching from randomly selected DOE profiles. Figure 6.5(a) indicates that the fitness value decreases rapidly and the algorithm converges after about 150 generations of μ GA. The optimized microlens profile and its intensity distribution on the focal plane are compared with those of the analytical lens profile in Figure 6.6(a) and (b). The optimized intensity distribution is almost identical to the analytical one. (The residue fitness value is 0.5088 over 800 sample points.) However, the optimized lens profile is slightly different from the analytical one. Note the differences at most cell locations are less than a FDTD grid size in the z direction, which means that the etch depth at these cells is treated as the same during the FDTD calculation. It is expected that different profiles can result in very close intensity distributions. In fact, from different runs μ GA-FDTD converged to several other profiles with similar performance, which demonstrates its excellent search and optimization capability.

In the above test, the combination of arithmetical and heuristic crossover is utilized in μ GA. A comparison test is carried out with same configurations of μ GA except that the arithmetical crossover is used. Although μ GA-FDTD can also converge to profiles with similar performance as the one found in above test, the convergence speed of arithmetical crossover is

much slower than that of the combination of arithmetic and heuristic crossover, which is clearly indicated by Figure 6.5(b).

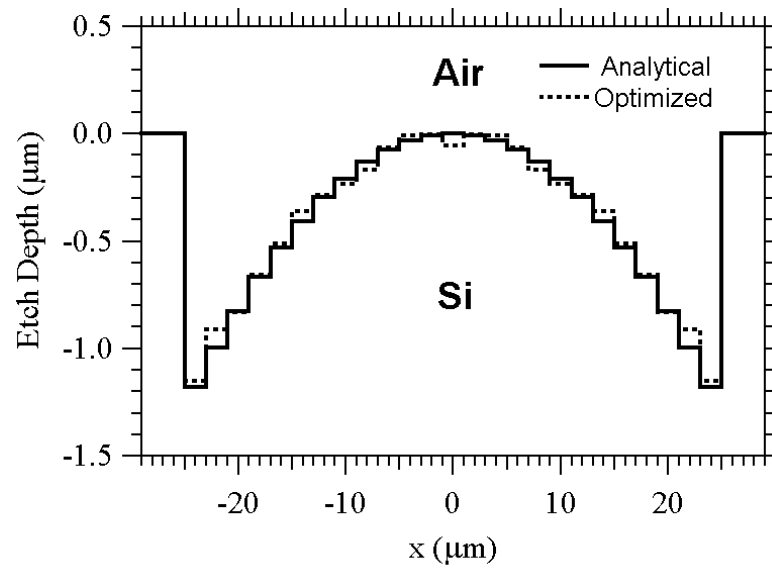


(a)

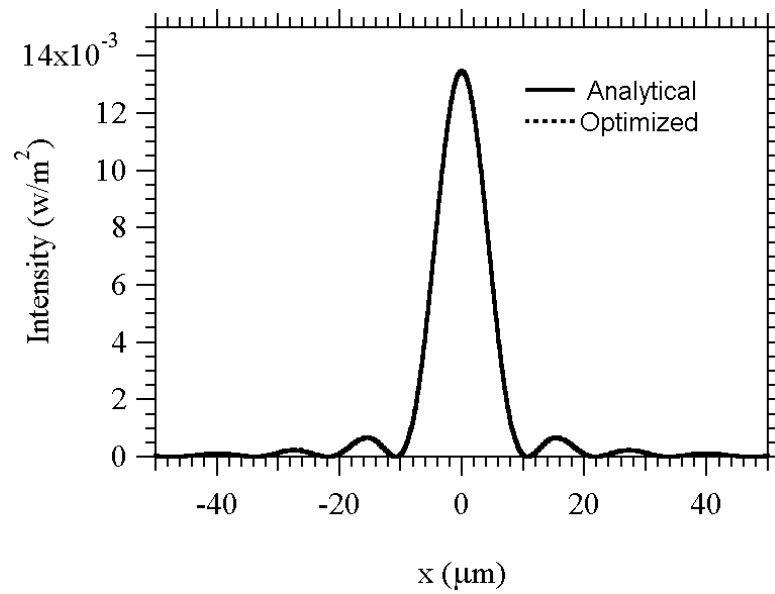


(b)

Figure 6.5 Convergence curves of the μ GA-FDTD on a microlens design case (target function approach) (a) combination of arithmetical and heuristic crossover and (b) arithmetical crossover



(a)



(b)

Figure 6.6 Microlens optimized by μGA -FDTD with target function approach (a) the analytical and μGA optimized lens profiles and (b) their intensity distributions on the focal plane

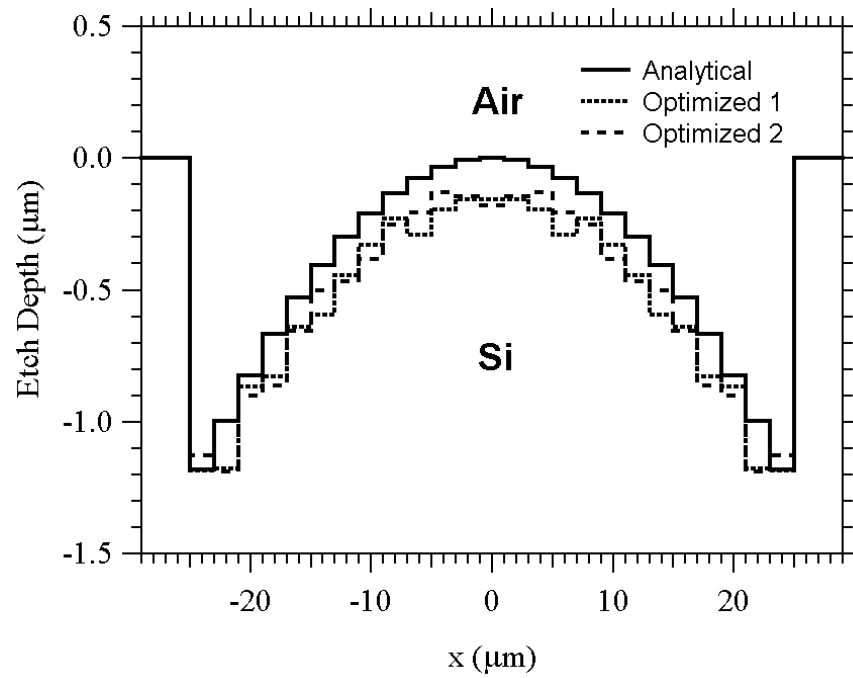
6.2.2 Weighting function approach

In this test, the weighting function approach, instead of the target function approach, is employed to design microlens. The purpose of this test is to find any profile that may outperform the analytical one. The weighting function used to control the intensity distribution on the focal plane is similar to the one shown in Figure 6.2(b) and can be written as

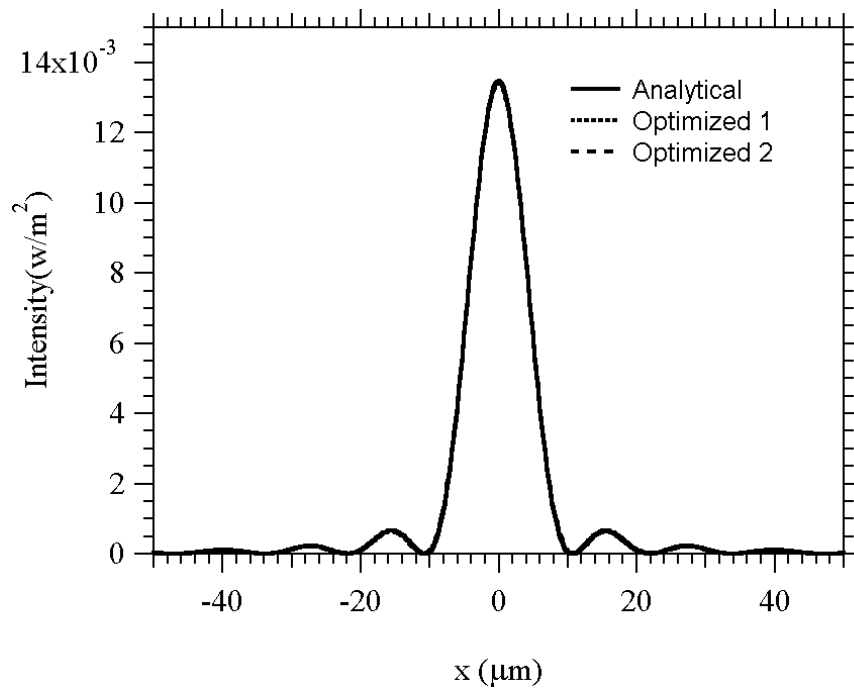
$$W(x_s) = 10 \exp\left(-\frac{x_s^2}{8}\right) - 10 \left(1 - \text{rect}\left(\frac{x_s}{20}\right)\right), \quad (6.5)$$

where $\text{rect}()$ is the rectangular function. The weighting function consists of two parts: a Gaussian function in the window from $-10\mu\text{m}$ to $10\mu\text{m}$ to control the peak intensity in the center and a constant negative weighting (penalty) outside this region to control the side-lobes. An apparent difference of this test is that the fitness function must be maximized instead of minimized in order to achieve the design goal.

Again the $\mu\text{GA-FDTD}$ found a number of lens profiles. Figure 6.7(a) and (b) show two optimized lens profiles along with the analytical profile and their corresponding intensity distributions on the focal plane. The performances of the optimized profiles are very close to that of analytical one, but cannot outperform it, which makes physical sense that the analytical profile is the best solution to this design problem. However, it is interesting to notice that the optimized lens profiles have a slightly shallow etch depth, which makes practical sense that they are easier to be fabricated. Their μGA convergence curves shown in Figure 6.8 demonstrate the rapid convergence of $\mu\text{GA-FDTD}$ once more.



(a)



(b)

Figure 6.7 Microlens optimized by μGA -FDTD with weighting function approach (a) analytical and two optimized lens profiles and (b) their intensity distributions on the focal plane

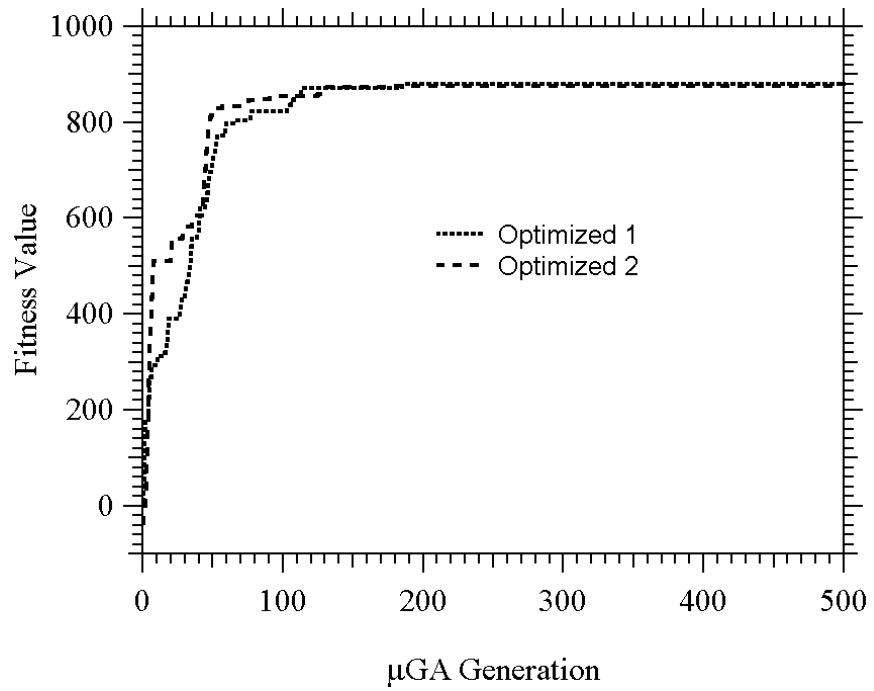


Figure 6.8 Convergence curves of μ GA-FDTD with weighting function approach

Chapter 7

FADOE DESIGN EXAMPLES AND APPLICATIONS

In this chapter, numerical results are presented for several FADOE components optimized by the μ GA-FDTD rigorous design tool outlined in the previous chapter. These components are based on the same design geometry, which is illustrated in Section 7.1. First, several 1-to-2 focusing beam fanners with various peak separation distances are designed. It is relatively easy to optimize such elements when the peak separation distance is small. As the separation distance increases, the optimization task becomes more challenging because of the field noise in the center of the observation plane. The fitness function must be carefully tuned to better control the intensity distribution so that the noise is subsided and more power is focused into the interested regions. Deeper etch depth and smaller feature size also may be necessary. Based on the experience gained from the 1-to-2 beam fanner, a 1-to-3 beam fanner with 50 μm peak separations is realized by an additional uniformity control constraint in the fitness function.

The power of the μ GA-FDTD rigorous design tool is further demonstrated by the optimization of two novel multi-functional elements, 1-to-2 beam fanner/quarter-wave plate and a focusing polarization beam splitter. Integration of multiple functions into a single element has numerous advantages such as cost reduction and improvement of the system stability. However, the multi-objective optimization problems associated with the design of such elements are much more complicated than single-objective optimization problems. The design of these elements is the first successful attempt toward this trend. The details of these two elements are covered in Section 7.3.

7.1 Design scenario

Figure 7.1 is the design geometry for all numerical examples presented in this chapter. Similar to the design geometry of the microlens in the previous chapter, the DOE's are assumed to be etched into Silicon substrate ($n_1=3.38$) and are illuminated from Silicon at normal incidence by a unit amplitude TE or TM polarized monochromatic plane wave with $\lambda_0=5\ \mu\text{m}$. The exit media is air ($n_2=1.0$). The observation plane is $100\ \mu\text{m}$ away from the Silicon/air interface, which is located in the near field region. Different design constraints can be applied to the field distribution on the plane to achieve different design functions. The width of the DOE's is $50\ \mu\text{m}$ and is uniformly divided into a number of cells depending on the minimum feature size. Also, all optimized DOE profiles presented below are unquantized.

For μGA , the deterministic rank selection and the combination of arithmetical and heuristic crossover were used for all the examples. Furthermore, the weighting function approach for the fitness function is adopted to impose various design constraints because of its flexibility.

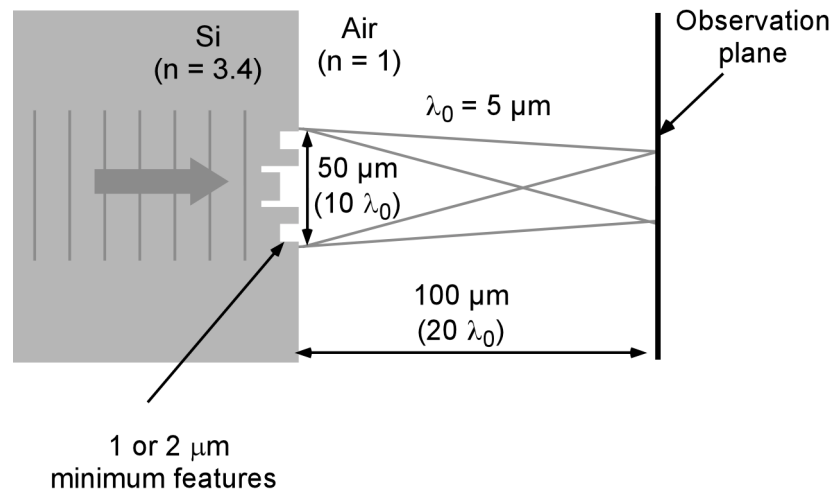


Figure 7.1 Geometry for the numerical design examples

In the application of the μ GA-FDTD design tool, it is critical to choose the proper maximum etch depth and minimum feature size of the FADOE's according to the design requirements because these parameters will directly affect the complexity of the optimization problem and the difficulty of the fabrication process in the future.

The minimum feature size will determine how many cells that the DOE will be divided into, which consequentially determines the number of parameters of the optimization problem. The maximum etch depth will determine the span of each parameter. With the determination of these two parameters, the solution space that the μ GA searches is completely defined. Therefore it is the designer's responsibility to properly choose these key parameters to ensure that some good solutions exist in the defined solution space.

On the other hand, these parameters will also affect the micro-fabrication process to realize the optimized design. The aspect ratio, which is defined as the ratio between the maximum etch depth and the minimum feature size, will determine the fabrication methodology and the ease of the fabrication process. Lower aspect ratio is always desired. The designer also must account for this fabrication issue when choosing these parameters.

The choice of these parameters is generally based on the experience and different trials of the μ GA-FDTD. This will be illustrated in the examples presented below.

7.2 Focusing beam fanners

Focusing beam fanners are diffractive optical elements commonly used in many applications such as pixelized infrared imaging polarimetry. Such elements split the incident beam into the required number of sub-beams and focus them into the specific regions (or target windows) on the observation plane to achieve the desired peak separations. In all design examples presented below, the target windows are defined as the region with 20 μm width about the locations of the desired peaks. For instance, in a 1-to-2 beam fanner with 25 μm peak

separation, the two target windows are $[-22.5 \mu\text{m}, -2.5 \mu\text{m}]$ centered at $-12.5 \mu\text{m}$ and $[2.5 \mu\text{m}, 22.5 \mu\text{m}]$ centered at $12.5 \mu\text{m}$. Note all 1-to-2 and 1-to-3 beam fanners considered here are physically symmetrical elements because the required beams are symmetrical about the z -axis.

The performances of the beam fanners are evaluated in terms of diffraction efficiency (DE), which is defined as the fraction of the power focused into the target windows to the total incident power. The design objectives are to maximize the diffraction efficiencies for both TE and TM illuminations and to minimize the difference of the diffraction efficiencies between them. It is important to point out that the running time of the code is doubled compared to that of microlens case because the performance of each potential DOE profile must be evaluated for both TE and TM by the FDTD algorithm.

7.2.1 1-to-2 focusing beam fanners

The 1-to-2 beam fanners are supposed to generate two focused beams on the observation plane with required peak separations. In this section, $\mu\text{GA-FDTD}$ design examples are presented for peak separations of 25, 50, 100, 200 μm . As pointed out in the previous section, for small peak separations of 25 and 50 μm , shallow etch depth can be used and the $\mu\text{GA-FDTD}$ found numerous DOE profiles that can fulfill the required functions. However, the diffraction efficiency drops as the peak separation becomes wider. To achieve reasonably good design, deeper etch depth and smaller minimum feature size must be used to enlarge the search space. This is clearly demonstrated in the design of 1-to-2 beam fanners with peak separations of 100 and 200 μm .

7.2.1.1 25 and 50 μm peak separations

Intuitively, for small peak separations, shallow etch depth may be enough. A good guess for the maximum etch depth is the depth corresponding to π phase shift, which is 1.05 μm for Si/Air interface at 5 μm wavelength. The minimum feature size is set to 2 μm , which results in 25

cells in the DOE aperture. In fact, since the DOE profile should be symmetric about the z-axis, the etch depth at 13 cell locations needs to be optimized.

Multiple constraints are required to achieve the design objectives. First the diffraction efficiencies of TE and TM are controlled by two weighting functions similar to Equation 6.5 but with two Gaussian functions centered about two beam locations, which can be written as

$$W(x_s) = 10 \left(\exp \left(-\frac{(x_s - 12.5)^2}{8} \right) + \exp \left(-\frac{(x_s + 12.5)^2}{8} \right) \right) - 10 \operatorname{rect} \left(\frac{x_s}{10} \right) - 10 \left(1 - \operatorname{rect} \left(\frac{x_s}{40} \right) \right) \quad (7.1)$$

for 25 μm peak separation and

$$W(x_s) = 10 \left(\exp \left(-\frac{(x_s - 25)^2}{8} \right) + \exp \left(-\frac{(x_s + 25)^2}{8} \right) \right) - 10 \operatorname{rect} \left(\frac{x_s}{30} \right) - 10 \left(1 - \operatorname{rect} \left(\frac{x_s}{80} \right) \right) \quad (7.2)$$

for 50 μm peak separation. Then an intensity uniformity constraint (penalty) is added to each weighting function to control the difference of diffraction efficiencies between TE and TM (i.e., the fifth term of Equation 6.1). Balance between intensity constraints and the uniformity constraint has to be made to ensure the realization of all the design objectives.

As in the microlens case studied in previous chapter, for each peak separation case, $\mu\text{GA-FDTD}$ found several FADOE profiles that satisfy the design requirements. The $\mu\text{GA-FDTD}$ design results for 25 μm are summarized in Figure 7.2(a)-(d), showing two optimized DOE profiles and their corresponding intensity distributions. The profiles are simple and easy to fabricate. Profile (a) achieves diffraction efficiency of 50.38% for TE and 52.58% for TM with a difference of 2.2% while profile (b) has a slightly better performance with a DE of 50.98% for TE illumination and 52.64% for TM illumination with a difference of 1.66% between them.

Figure 7.3 illustrates two μ GA-FDTD optimized 1-to-2 beam fanners with 50 μm peak separation. The two profiles have almost identical performance for TE illumination (the DE is about 43.54%) and a little different performances for TM (The DE of profile (a) is 45.56% and that of profile (b) is 44.56%). However, the higher DE of profile (a) results in a bigger difference in DE between TE and TM than the profile (b) so that their performances in terms of fitness values are very close. This is a vivid example of the tradeoff between different design objectives.

The μ GA convergence curves for all four designs are shown in Figure 7.4, which demonstrate the excellent convergence of the μ GA-FDTD rigorous design tool again.

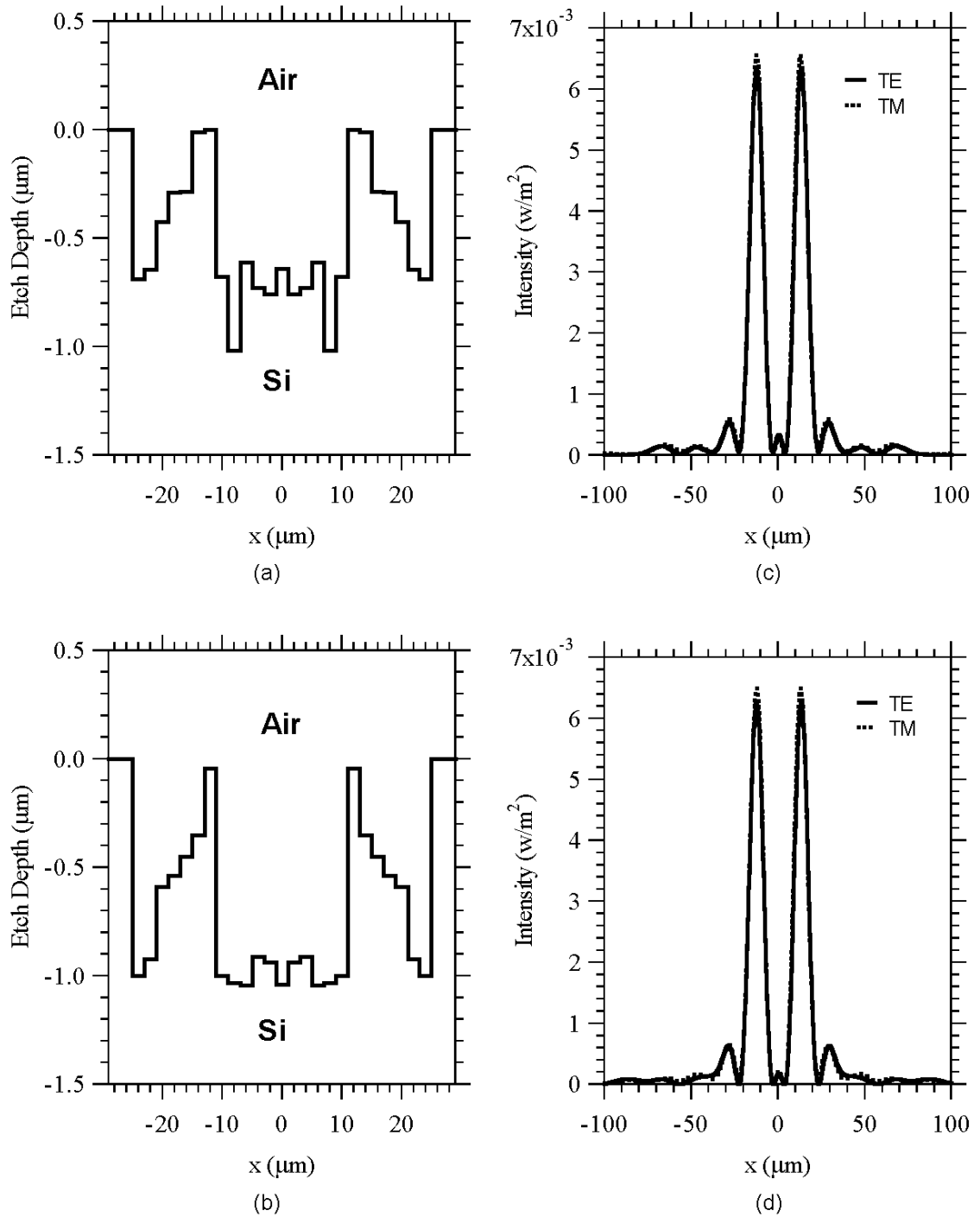


Figure 7.2 Two μ GA-FDTD optimized 1-to-2 beam fanners with 25 μm peak separation

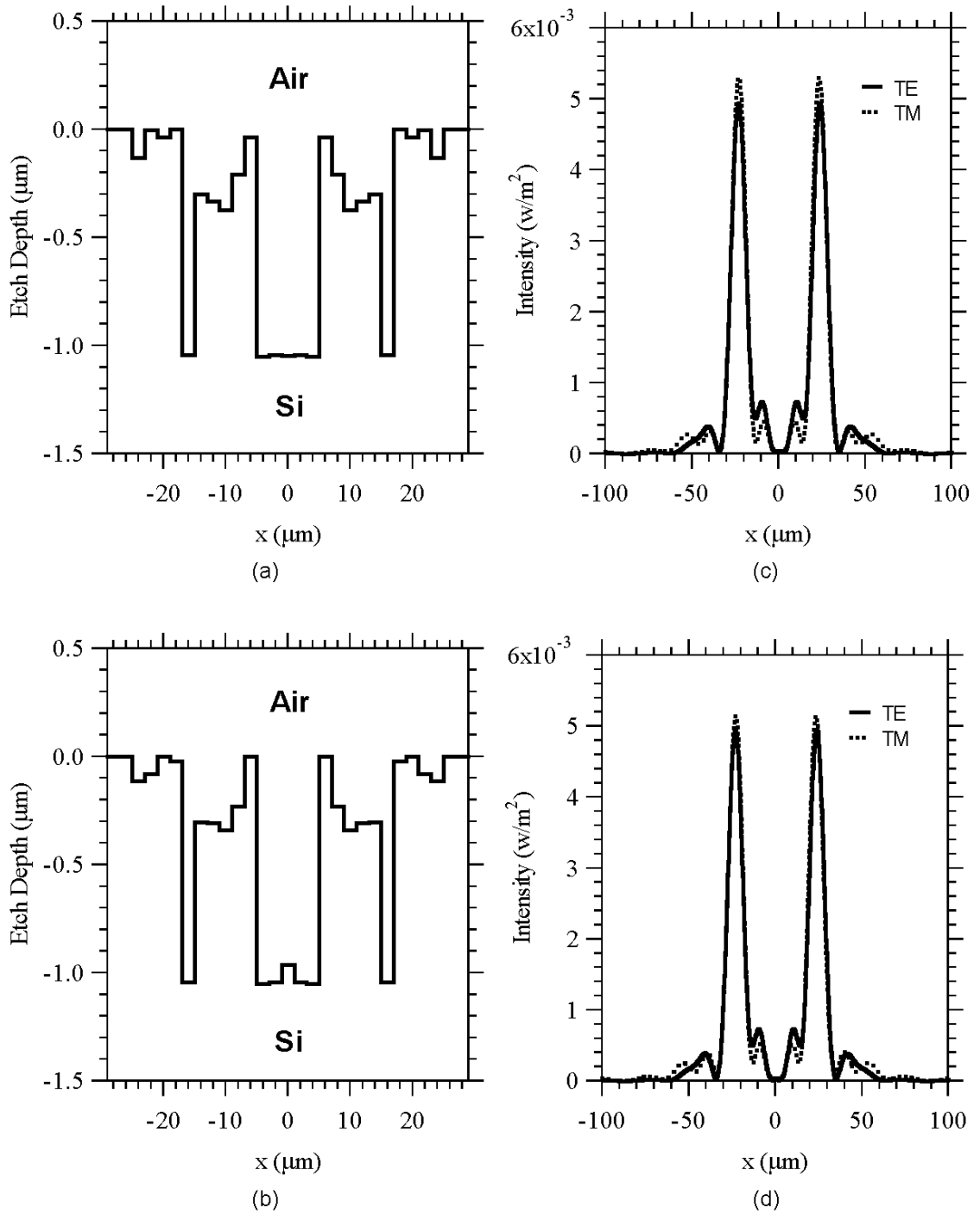
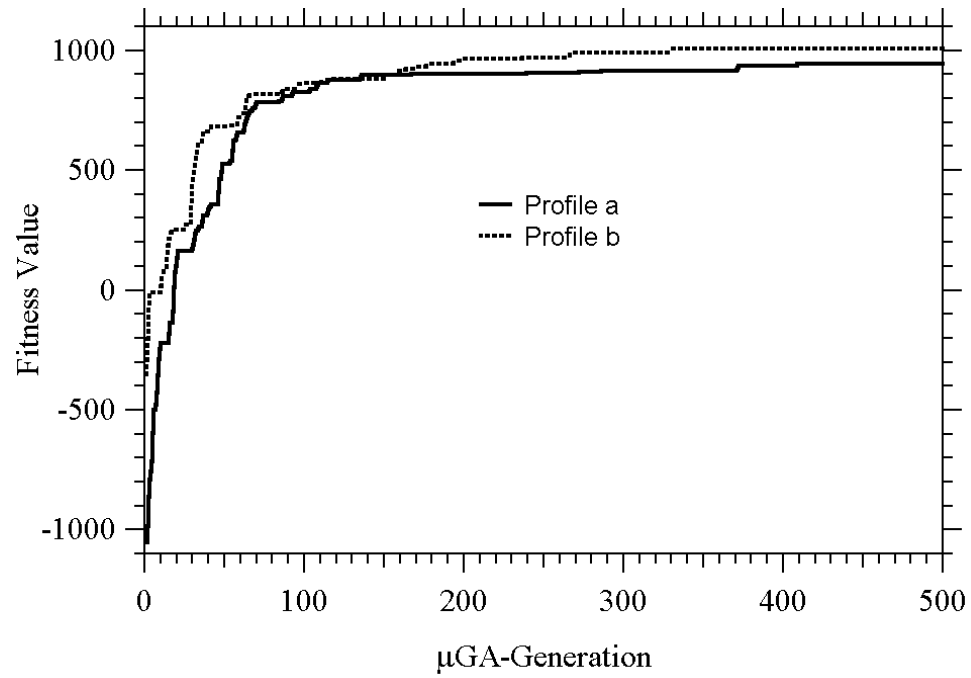
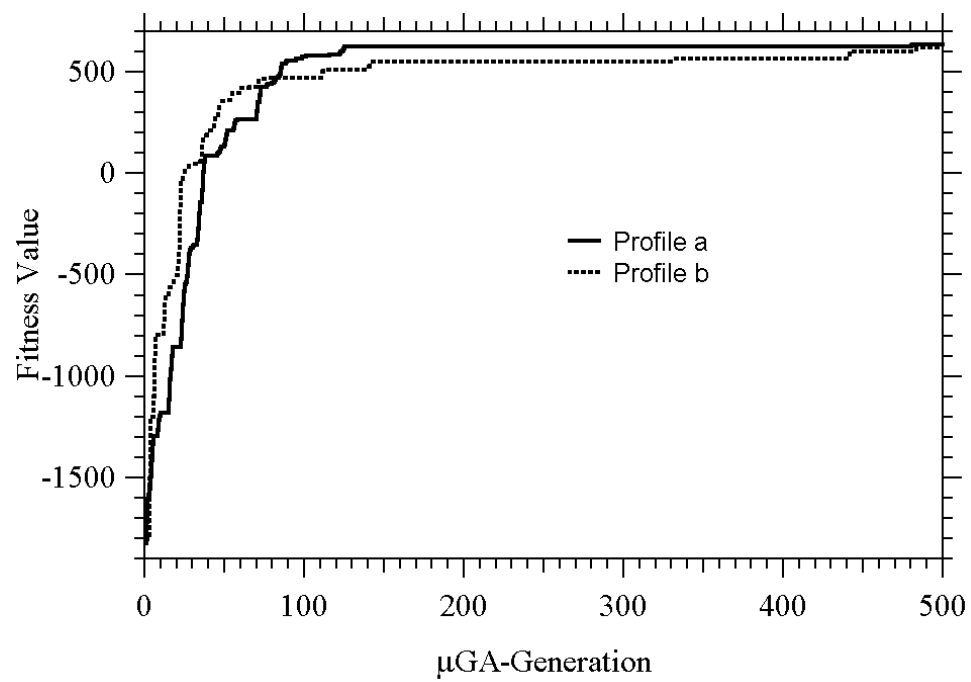


Figure 7.3 Two μGA -FDTD optimized 1-to-2 beam fanners with 50 μm peak separation



(a)



(b)

Figure 7.4 μGA convergence curves for 1-to-2 beam fanner designs with different peak separations (a) 25 μm and (b) 50 μm

7.2.1.2 100 and 200 μm peak separations

Designing wide-angle beam fanners is a challenging job. For the design scenario we consider herein, the 100 and 200 μm peak separations of the 1-to-2 beam fanner correspond to the angular separations of 53.13° and 90° . During the design of these beam fanners, a noticeable phenomenon is that the diffraction efficiency drops as the peak separation becomes wider if the same maximum etch depth and minimum feature size for 25 and 50 μm cases are used. Figure 7.5 illustrates two μGA -FDTD optimized 1-to-2 beam fanners for 100 μm (Figure 7.5 (a) and (c)) and 200 μm (Figure 7.5 (b) and (d)). In both cases, the performances are much worse than the elements of 25 and 50 μm . The peak intensity decreases and the noise out of the target windows increases. The 100 μm element only has diffraction efficiencies of 34.51% for TE and 36.12% for TM respectively, which is about 15% lower than those of the 25 μm element. The design of the 200 μm element doesn't perform the function of 1-to-2 beam splitting anymore.

To improve the designs for these elements, deeper etch depth and smaller feature size may be used to broaden the solution space. Physically deeper DOE structures appear to be able to scatter the incident light over a broader angular range and more feature cells means more design freedom so that the characteristics of the FADOE can be better controlled.

In the redesign of the 100 μm element, the maximum etch depth is doubled to 2.1 μm , which corresponds to a 2π phase shift and the minimum feature size is kept the same. The weighting function is

$$W(x_s) = 20 \exp\left(-\frac{(x_s - 50)^2}{16}\right) + 20 \exp\left(-\frac{(x_s + 50)^2}{16}\right) - 10 \text{rect}\left(\frac{x_s}{80}\right) - 10 \left(1 - \text{rect}\left(\frac{x_s}{120}\right)\right) \quad (7.3)$$

Two improved designs are shown in Figure 7.6. The Profile a has DE of 44.83% for TE illumination and 48.66% for TM with a difference of 3.83% while those of profile b are 45.39%, 50.09% and 4.7% respectively. Both elements perform much better than the previous design.

On the other hand, the redesign process for the 200 μm element is far more difficult than that of the 100 μm one because of the challenge of the problem. The maximum etch depth is further increased to 3.15 μm , which corresponds to a 3π phase shift and the minimum feature size decreases to 1 μm , which results in 50 cells in the aperture of the FADOE's. The weighting function is carefully tuned to

$$W(x_s) = 80 \left(\exp \left(-\frac{(x_s - 100)^2}{8} \right) + \exp \left(-\frac{(x_s + 100)^2}{8} \right) \right) - 10 \text{rect} \left(\frac{x_s}{150} \right) - 10 \left(1 - \text{rect} \left(\frac{x_s}{250} \right) \right) \quad (7.4)$$

A μGA -FDTD optimized design is illustrated in Figure 7.7. The design achieved a DE of 27.8% for TE illumination and 33.2% for TM illumination. Although the performance is greatly improved, it is still not good enough. More numerical experiments show that there is no dramatic improvements in performance if the etch depth is further increased.

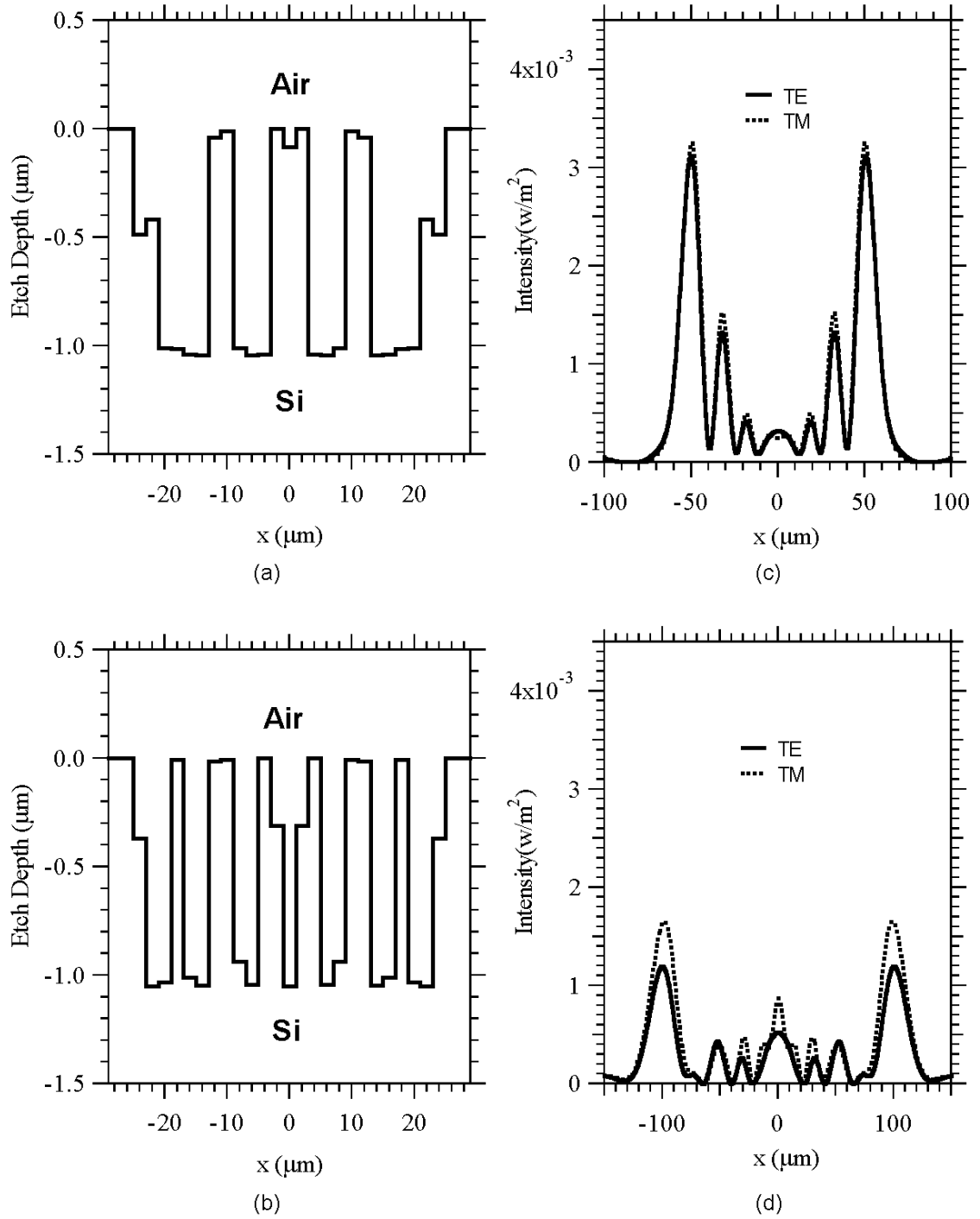


Figure 7.5 $\mu\text{GA-FDTD}$ optimized 1-to-2 beam fanners with 100 and 200 μm peak separations using same maximum etch depth and minimum feature size as those of the 25 and 50 μm peak separation cases

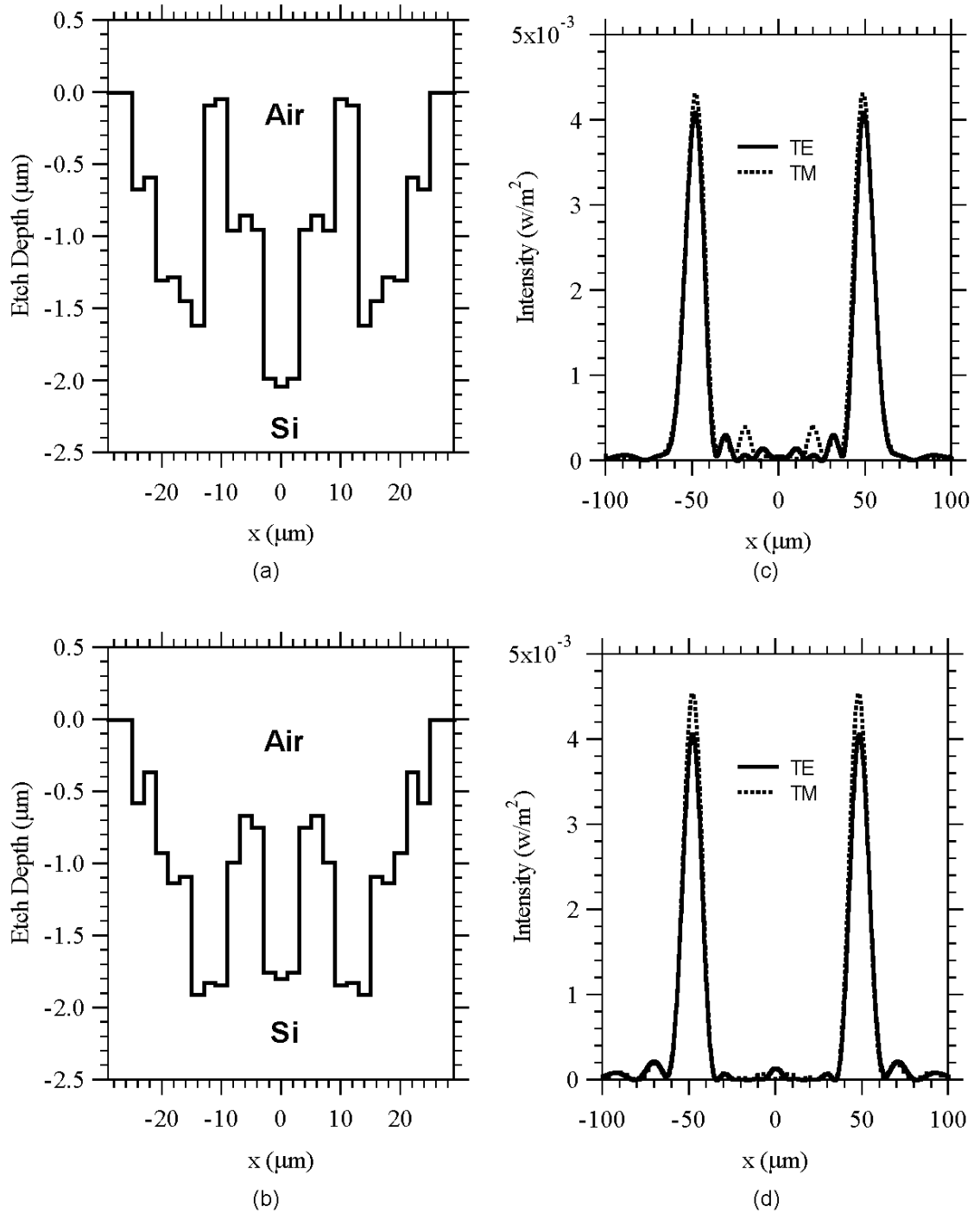
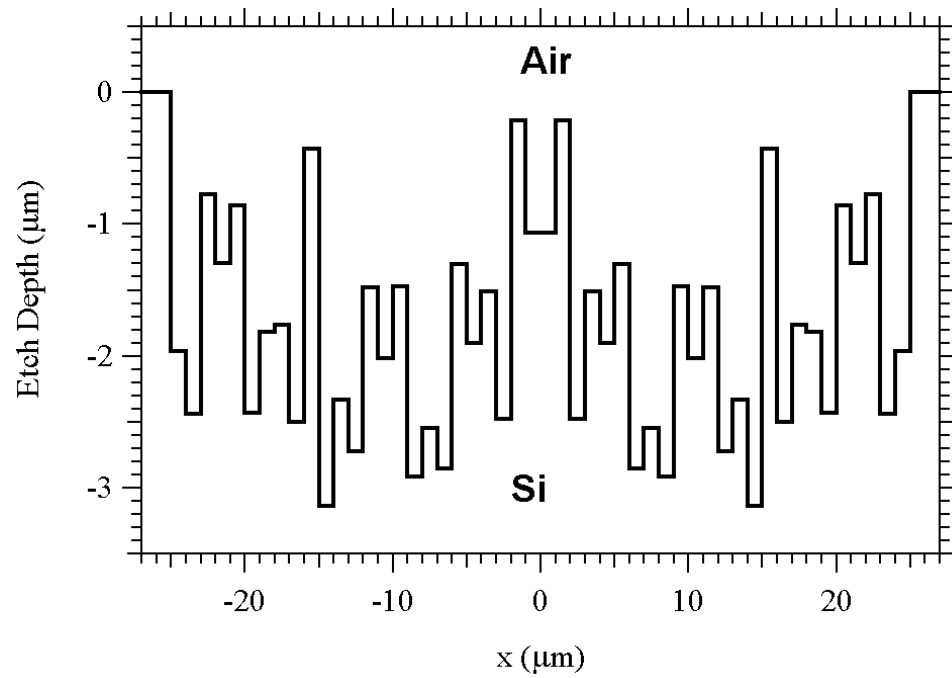
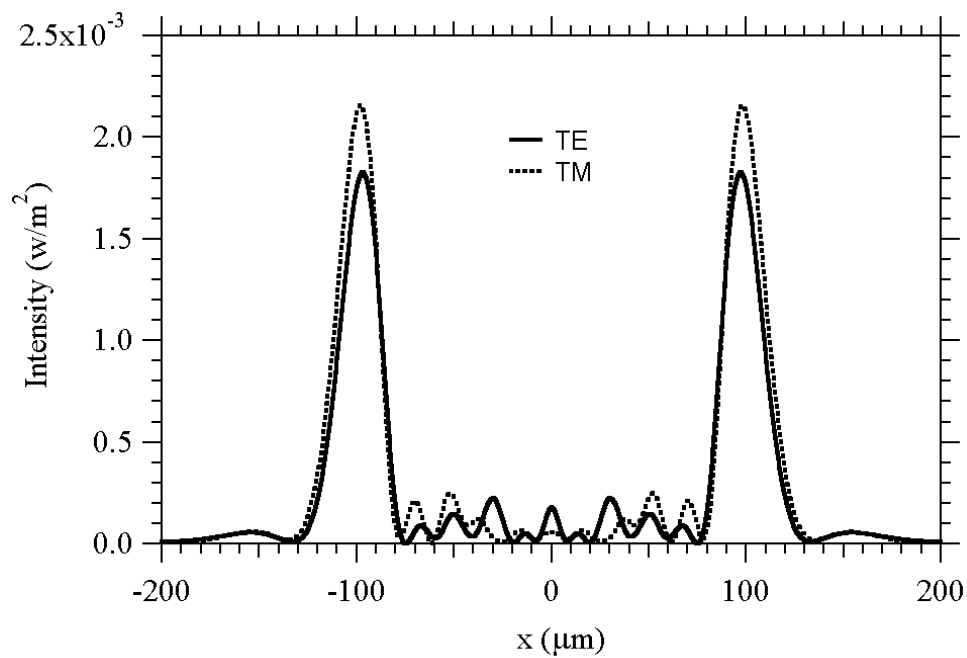


Figure 7.6 Two improved $\mu\text{GA-FDTD}$ optimized 1-to-2 beam fanners with 100 μm peak separation with deep etch depth



(a)



(b)

Figure 7.7 Improved μGA -FDTD design for 1-to-2 beam fanners with $200 \mu\text{m}$ peak separation with deeper etch depth and smaller feature size (a) DOE profile and (b) the intensity distribution on the focal plane

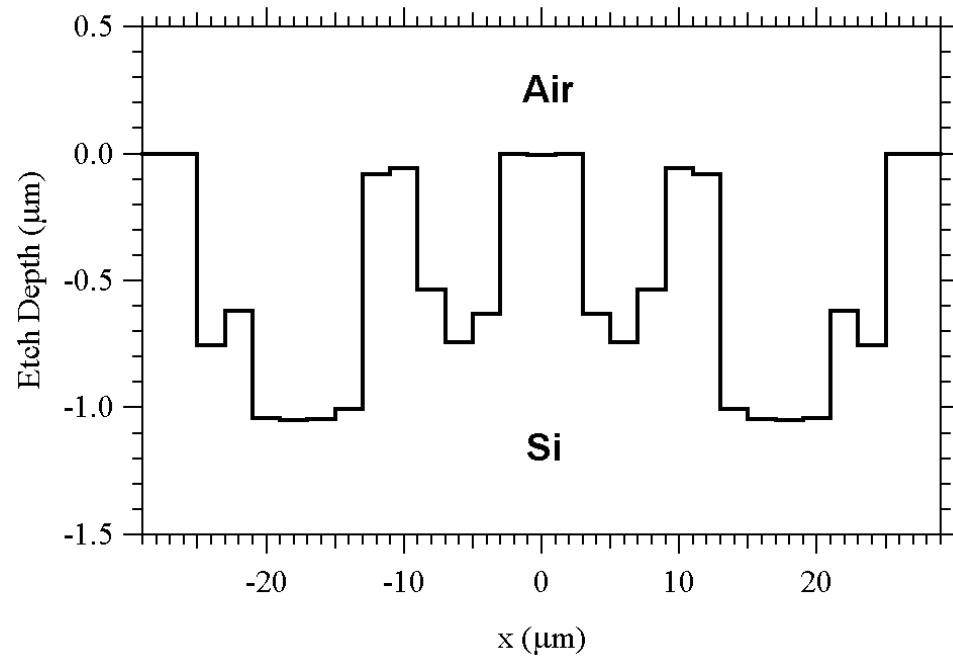
7.2.2 1-to-3 focusing beam fanner

In this design problem, a FADOE element is required to split the incident beam into three sub-beams and focus them to three target windows centered at $-50 \mu\text{m}$, 0 and $+50 \mu\text{m}$ in the focal plane. Since the peak separation is $50 \mu\text{m}$ in this 1-to-3 beam fanner, the settings of $\mu\text{GA-FDTD}$ for a 1-to-2 beam fanner with $50 \mu\text{m}$ peak separation may be applicable. Based on this idea, the maximum etch depth is set to $1.05 \mu\text{m}$ and the minimum feature size is set to $2 \mu\text{m}$. The weighting function can be expressed as

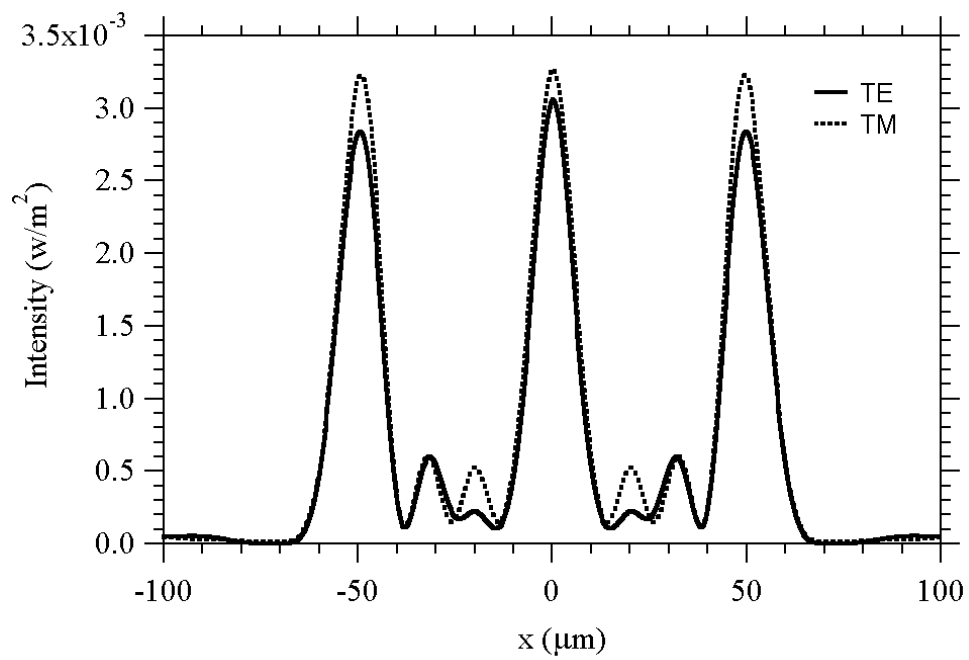
$$W(x_s) = 20 \left(\exp\left(-\frac{(x_s - 50)^2}{8}\right) + \exp\left(-\frac{x_s^2}{8}\right) + \exp\left(-\frac{(x_s + 50)^2}{8}\right) \right) - 8 \text{rect}\left(\frac{x_s - 25}{20}\right) - 8 \text{rect}\left(\frac{x_s + 25}{20}\right) - 10 \left(1 - \text{rect}\left(\frac{x_s}{140}\right) \right) \quad (7.5)$$

Then three uniformity constraints (penalty) are added to the fitness function. A uniformity constraint must be applied for each of the TE and TM illuminations to control the peak intensity difference between the center window and $-50 \mu\text{m}$ window. This uniformity constraint is decisive to the success of the μGA optimization because μGA would converge to a microlens without it. Also another uniformity constraint is necessary to control the difference of diffraction efficiencies between TE and TM. Balance between all these design constraints becomes so complicated that it requires several test runs of the $\mu\text{GA-FDTD}$.

Figure 7.8(a) shows an optimized 1-to-3 beam fanner profile and Figure 7.8(b) shows its intensity distribution on the focal plane. This design achieves a DE of 48.42% for TE illumination and 53.84% for TM with a 5.43% difference. The peak intensities are also quite uniform for both TE and TM illumination, with a 1.04% difference for TE and 0.83% for TM.



(a)



(b)

Figure 7.8 μGA -FDTD optimized 1-to-3 beam fanners with 50 μm peak separations (a) DOE profile and (b) its intensity distribution on the focal plane

7.3 Novel multi-functional elements

The design examples presented in the previous section demonstrate that multi-objective designs can be realized with the careful balance among objectives in the fitness function, although it is hard to achieve in certain cases. This means that it is possible to design multi-functional FADOE elements with the μ GA-FDTD rigorous design tool under the control of multi-objective fitness function. As mentioned previously, such multi-functional FADOE elements have numerous advantages compared to single functional counterparts. In this section, the design of two novel multi-function FADOE elements is explored. The first one is a focusing 1-to-2 beam fanner/quarter-wave plate element, which realizes three functions: beam splitting, focusing, and phase retardance control. The other one is a focusing TE/TM polarization beam splitter, which also realizes three functions: beam splitting, focusing and polarization separation. The details of these two elements are presented below.

7.3.1 Focusing 1-to-2 beam fanner/quarter-wave plate

This element is based on the design of 1-to-2 beam fanners. In the design of a 1-to-2 beam fanner, if the phase difference between fields of TE and TM in the two beam windows is controlled to be $\pi/2$, we can realize a new element that can perform as a focusing beam fanner and a quarter-wave plate at the same time. In this design, the two output beams are separated by $50 \mu\text{m}$ at the focal plane and the phase difference within a $20 \mu\text{m}$ window centered about each beam is required to be $\pi/2$. The design objectives are the same as those of the previous example except for an additional objective on the phase difference, which makes the balance among different objectives more difficult. To realize this additional objective, a phase constraint (the last term in Equation. 6.1) is attached to the fitness function for a 1-to-2 focusing beam splitter. The minimum feature size is set to $1\mu\text{m}$ so that the DOE is divided into 50 cells. The maximum etch depth is set to $3.15\mu\text{m}$, which corresponds to a 3π phase retardance.

The DOE profile resulted after 500 generations of μ GA, shown in Figure 7.9(a), has a diffraction efficiency of 21.71% for TE and 25.87% for TM with a uniformity difference of 4.16%, which is poorer than those of the pure 1-to-2 beam fanner design discussed in the previous section. These poor performances are traded for the additional design objective, the constant phase difference between TE and TM, which is represented in Figure 7.9(c). The phase difference is almost constant ($\pi/2$) within the required windows. Figure 7.9(d) is the μ GA convergence curve for this design. Note μ GA does not converge as fast as it did for other examples discussed above. This is mainly due to more complex solution space defined by deeper etch depth and smaller feature size.

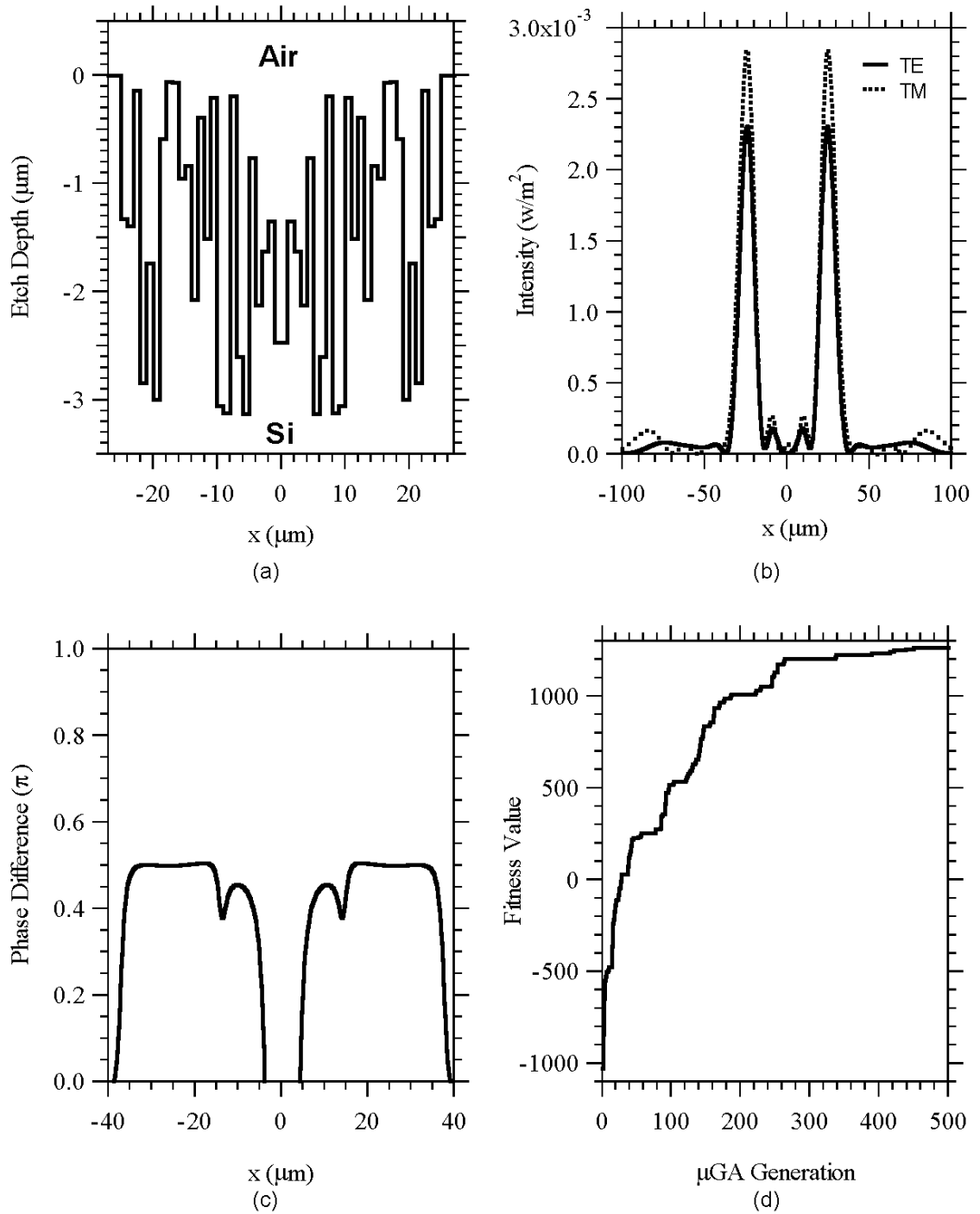


Figure 7.9 Results of μ GA-FDTD design on a focusing 1-to-2 beam fanner/quarter-wave plate multi-functional FADOE element

7.3.2 Focusing polarization beam splitter

The other multi-functional element designed by μ GA-FDTD, also the final example, is a focusing polarization beam splitter. In this design problem, an unsymmetrical FADOE was optimized for focusing polarization beam splitting, that is, the DOE must focus the TE illumination into a 15 μm detecting window centered at +12.5 μm while focusing TM illumination into a similar window centered at -12.5 μm , which results in a center separation of 25 μm for TE and TM. The design objectives are to maximize the diffraction efficiencies into two target windows and to maintain the uniform performance for TE and TM. The minimum feature size and maximum etch depth are 1 μm and 3.15 μm respectively. The fitness function consists of two weighting function terms and the intensity uniformity term of Equation 6.1.

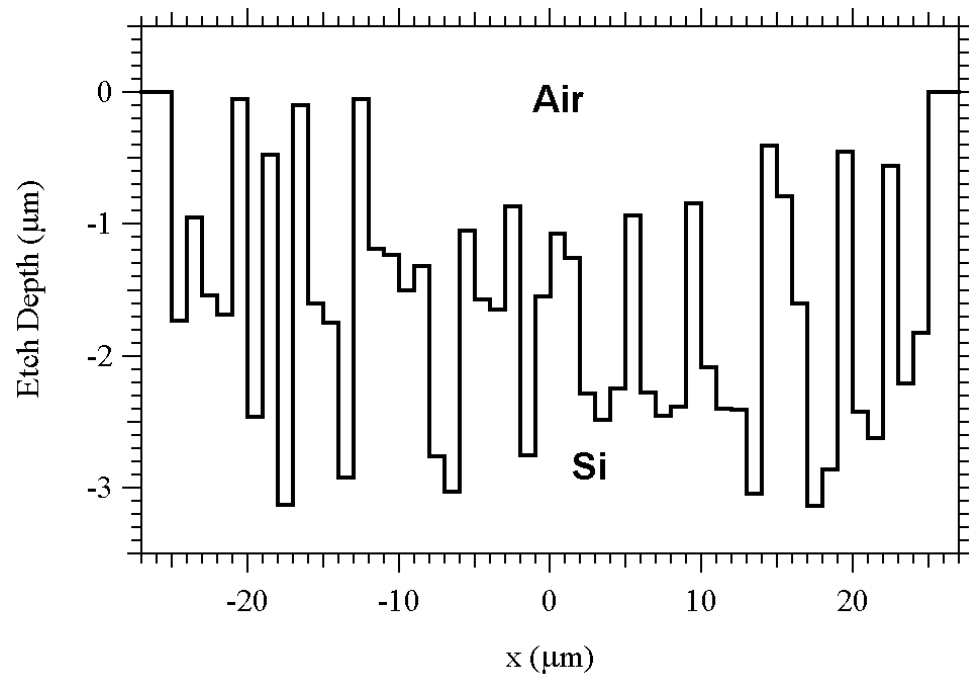
After 1200 μ GA generations, μ GA-FDTD resulted in a DOE profile, which is summarized in Figure 7.10. The profile produces 18.56% diffraction efficiency for TE illumination and for 18.05% TM illumination with 0.51% non-uniformity. Suppose detectors are placed at the centers of the detecting windows, two extinction ratios can be defined. In the TE detecting window (centered at +12.5 μm), the extinction ratio ER_{em} is defined as

$$ER_{em} = \frac{\text{Detected Power of TE}}{\text{Detected Power of TM}} \quad (7.6)$$

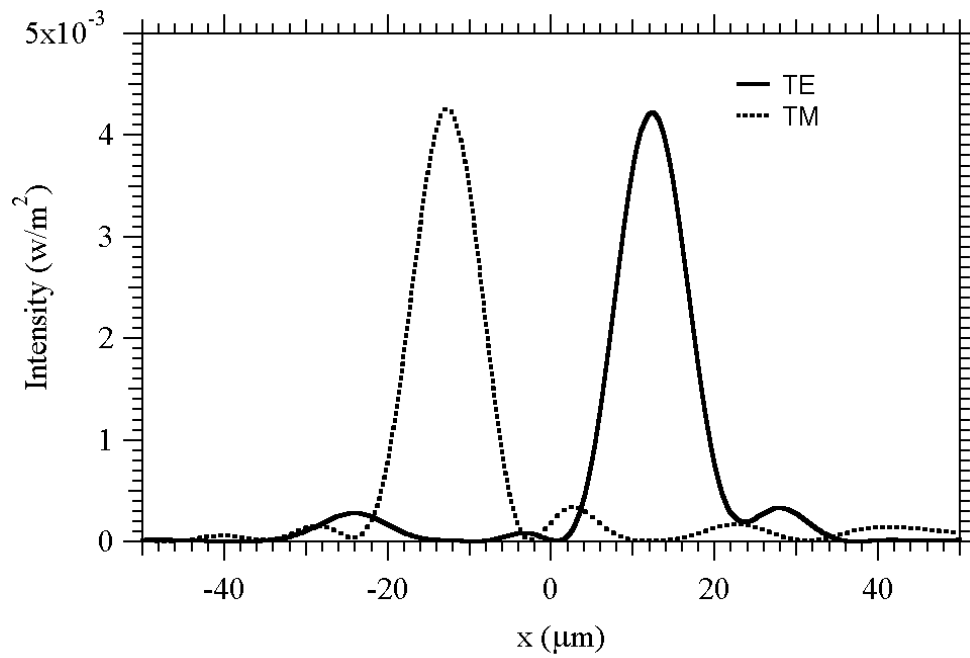
Similarly, in the TM detecting window (centered -12.5 μm), the extinction ration ER_{me} is defined as

$$ER_{me} = \frac{\text{Detected Power of TM}}{\text{Detected Power of TE}} \quad (7.7)$$

Figure 7.11 shows ER_{em} and ER_{me} as a function of the aperture of the detectors. For a 15 μm diameter detector, ER_{em} and ER_{me} are 74.9 and 46.5, which are good enough for most applications.



(a)



(b)

Figure 7.10 A μGA -FDTD optimized focusing TE/TM polarization beam splitter (a) DOE profile and (b) intensity distributions on the local plane

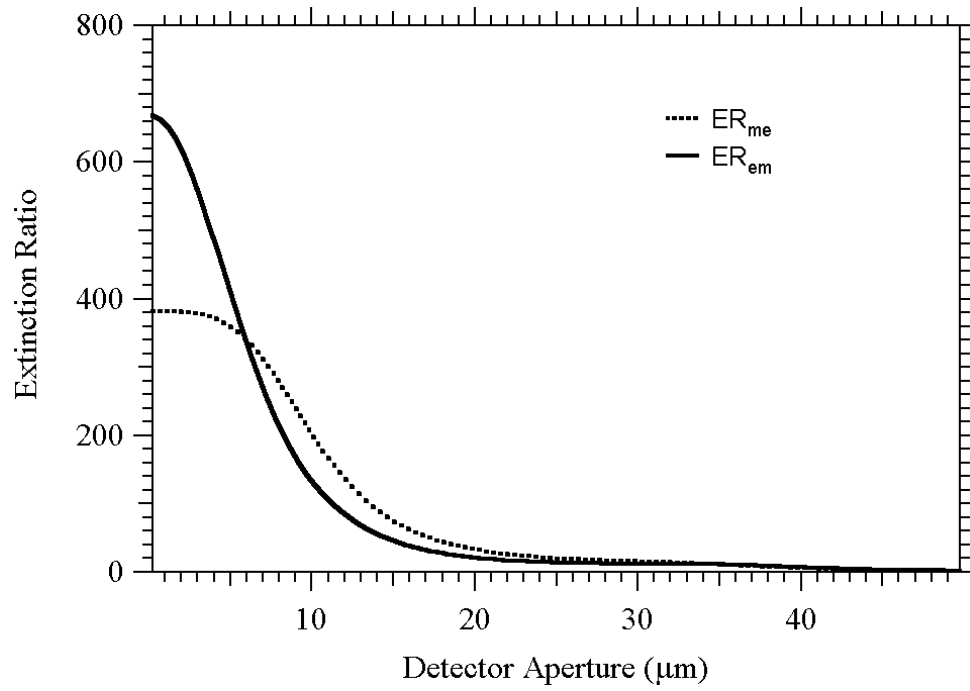


Figure 7.11 Two extinction ratio functions of the TE/TM polarization beam splitter

Chapter 8

DISCUSSION AND CONCLUSIONS

This dissertation focuses on the rigorous analysis and design of diffractive optical elements. Two types of DOE structures have been explored, namely the infinite periodic stacked rotated grating structures (SRGS's) and finite aperture aperiodic DOE's (FADOE's). For the rigorous analysis of SRGS's, a novel rigorous coupled-wave analysis (RCWA) algorithm, SRG-RCWA, was developed based on the standard three-dimensional RCWA algorithm. For the rigorous analysis of one-dimensional FADOE's, a two-dimensional finite-difference time domain (FDTD) algorithm was implemented. Furthermore, a rigorous design tool for designing one-dimensional FADOE's has been successfully developed, which utilizes the two-dimensional FDTD algorithm as the electromagnetic model and a micro-genetic algorithm (μ GA) as the global optimization method. In this chapter, a summary of these algorithms is presented followed by some recommendations towards future research in both the analysis and design areas. The limitations of the developed algorithms are discussed within the framework of the proposed future work.

8.1 Summary

The first part of the dissertation (Chapter 3) is concerned with the rigorous analysis of multi-layer stacked rotated grating structures (SRGS's). A novel rigorous analysis method for stacked rotated gratings (SRG's), termed the SRG-RCWA algorithm, has been developed, which is based on the standard 3-D RCWA algorithm. The difficulty of applying the standard 3-D

RCWA algorithm to the diffraction of SRGS's is first analyzed, which is found to be the requirement of the same grating periods in x and y directions for all the two-dimensional gratings in the stack. This difficulty is eliminated by the new concept of sampling frequency, that is, if the diffracted orders generated by all gratings lie on the same lattice in k-space (called a sampling lattice with x and y fundamental spatial frequencies, called sampling frequencies), all grating layers in the SRGS can be expanded into Fourier series with two sampling frequencies as fundamental frequencies so that the RCWA algorithm can still be applicable. With the SRG-RCWA algorithm, it is possible to rigorously analyze multi-grating-layer SRGS's that have gratings with different periods and orientations for the first time. In the new implementation of standard 3-D RCWA, Lalane's improved eigenvalue formulation is adopted and Moharam's enhanced transmittance matrix method for one-dimensional gratings is extended to two-dimensional gratings to make the new implementation efficient and stable.

Two fabricated SRGS's, designed as circular polarization filters for an infrared imaging polarimetry system, have been successfully characterized by the SRG-RCWA algorithm. The agreement between the experimental measurements and the SRG-RCWA numerical results demonstrated the validity and usefulness of the SRG-RCWA algorithm. The SRG-RCWA is believed to be very useful to many potential applications, such as photonic band gap structures with arbitrary rotated gratings.

The second part of the dissertation (Chapter 4-Chapter 7) is about the rigorous analysis and design of FADOE's. The main goal of this part of the research is to develop a rigorous design tool for FADOE's. A unidirectional design method, μ GA-FDTD, has been successfully developed.

First, a two-dimensional FDTD algorithm for one-dimensional FADOE's is implemented with the latest FDTD numerical techniques. This FDTD algorithm serves not only as the rigorous analysis tool for FADOE's, but also as the rigorous computational core for the proposed FADOE design tool. The FDTD algorithm has recently become popular for a wide variety of

electromagnetic problems and is a powerful numerical electromagnetic method. However, because of the computationally intensive nature of the algorithm, special attention must be paid to make the algorithm as efficient as possible. An excellent absorbing boundary condition, the PML ABC has been incorporated into the algorithm to limit the FDTD computational region just around the boundaries of FADOE's. Then an efficient vector plane wave spectrum method is employed to propagate the field calculated with FDTD to the observation plane. In this way, we avoid extending the FDTD computational region to the desired observation plane and hence greatly reduce the computational cost associated with the FDTD algorithm. Also the symmetry property of the FADOE's is utilized to cut FDTD computation by half.

In unidirectional DOE design methods, global optimization methods are required to achieve optimum designs. In this dissertation, a small population micro-genetic algorithm (μ GA) has been applied to the rigorous FADOE design for the first time. μ GA is an excellent global optimization method, especially for problems with complex, multi-modal, highly nonlinear solution space. Implementing μ GA is straightforward. In fact, a complete genetic algorithm package has been developed, in which both large population size conventional GA and μ GA were implemented. The package includes different encoding methods, and various selection and crossover operators. In particular, a 'creep' operator is introduced to enhance the local search capability of μ GA. Nevertheless, applying μ GA efficiently to the specific problem is not easy. Choices of different types of genetic operators and their parameters need a good understanding of both the operators and the working problem. Several test runs might be necessary for some tough design problems.

A sophisticated fitness function has been set up especially for FADOE design problems. With the precision control provided by the fitness function, multiple design constraints can be imposed on both intensity and phase distributions and their uniformity characteristics on the observation plane so that multi-objective optimizations can be realized. A variety of FADOE

elements have been optimized by the proposed μ GA-FDTD rigorous design tool, including common DOE elements such as microlens, 1-to-2 beam fanners, a 1-to-3 beam fanner and two novel multi-functional elements.

8.2 Recommendations for future research

In this dissertation, the SRG-RCWA was developed based on the standard three-dimensional RCWA algorithm. In recent years several improved formulations of RCWA have appeared in the literature, such as Li's Fourier factorization formulation [68] and Granet's adaptive spatial resolution formulation [97]. According to Li, the Lalane's improved eigenvalue formulation for the RCWA algorithm employed in the SRG-RCWA implementation is empirical and doesn't follow the Fourier factorization correctly and the converging speed is slower than Li's formulation. That means the convergence could be faster for SRG-RCWA if Li's formulation is adopted. Granet's formulation is a major progress in RCWA modeling with much faster convergence performance. However, the method is only formulated for one-dimensional gratings at present. Future work can be carried out to formulate Granet's algorithm for two-dimensional gratings and improve the SRG-RCWA by utilizing its fast convergence.

On the other hand, much work can be done on the design of FADOE's with the μ GA-FDTD design tool. Designs have been demonstrated only for a simple design scenario from a pure theoretical viewpoint. The μ GA-FDTD is quite versatile and can be applied to any design scenario for practical applications.

Several aspects can be improved in the present implementation of μ GA-FDTD. First, both μ GA and FDTD are parallel in nature so the code of the whole μ GA-FDTD is very easy to parallelize. For instance, a factor of 8 improvement in the computational efficiency can be achieved if the parallelized code runs on an 8-CPU workstation. Another possible improvement of μ GA-FDTD is the encoding method for electrically large aperture FADOE's. For such

FADOE's, the present encoding method is not efficient, which will result in a very large number of parameters and in turn a very complex optimization problem. Alternative encoding methods such as wavelets are likely used to reduce the number of parameters and to simplify the problem for the μ GA.

Because μ GA is an excellent optimization method, it may be useful and interesting to link it to various diffraction models such as the scalar plane wave spectrum method and standard two-dimensional and three-dimensional RCWA algorithms. Such integration can greatly broaden the applications of the μ GA and a wider range of DOE element can be optimized and designed.

APPENDIX A

**STANDARD THREE-DIMENSIONAL RIGOROUS COUPLED-WAVE ANALYSIS
ALGORITHM FOR MULTI-LAYER TWO-DIMENSIONAL GRATING STRUCTURES**

In this appendix the implementation of a stable and efficient three-dimensional RCWA algorithm for the diffraction of multi-layer stack with two-dimensional grating and homogeneous layers is illustrated. For generality and completeness, the implementation is formulated for the stacks of grating layers and homogeneous layers in any arbitrary order. Because the algorithm is based on an extension of the enhanced transmittance matrix approach of Moharam *et al.* [16] for 1-D gratings and also adopts Lalanne's [65] improved eigenvalue formalism, their notation will be followed in the derivation.

A. Geometry of the problem

Consider the geometry illustrated in Figure A.1 of a stacked multi-layer grating structure consisting of two two-dimensional grating layers and a homogeneous layer. Note that in general, a stack may have any number of grating layers and homogeneous layers in any arbitrary order. To apply RCWA to the stack, all of the grating layers must have the same periodicity, Λ_x , along the x direction and the same periodicity, Λ_y , along the y direction. The thickness for the ℓ th layer is d_ℓ , in which ℓ is the layer index. The number of layers in the stack is L and the total thickness of

the stack is $Z_L = \sum_{\ell=1}^L d_\ell$.

The whole stack can be divided into three regions: the incident region (Region I), the stack region (Region II), and the exit region (Region III). Regions I and III are isotropic dielectric media, characterized by permittivity ϵ_I and ϵ_{III} . The periodic permittivity and the inverse-permittivity of each grating layer in the stack region are expanded in Fourier series of the spatial harmonics according to

$$\epsilon_\ell(x, y) = \sum_{g,h} \epsilon_{\ell,gh} \exp\left(j \frac{2\pi gx}{\Lambda_x} + j \frac{2\pi hy}{\Lambda_y}\right), \quad (\text{A.1})$$

$$\varepsilon_{\ell}^{-1}(x, y) = \sum_{g,h} A_{\ell,gh} \exp\left(j \frac{2\pi gx}{\Lambda_x} + j \frac{2\pi hy}{\Lambda_y}\right), \quad (\text{A.2})$$

in which $\varepsilon_{\ell,gh}$ and $A_{\ell,gh}$ are the Fourier coefficients for ℓ th layer, which can be easily determined by

$$\varepsilon_{\ell,gh} = \frac{1}{\Lambda_x} \frac{1}{\Lambda_y} \int_0^{\Lambda_x} \int_0^{\Lambda_y} \varepsilon_{\ell}(x, y) \exp\left(-j \left(\frac{2\pi gx}{\Lambda_x} + \frac{2\pi hy}{\Lambda_y}\right)\right) dx dy, \quad (\text{A.3})$$

$$A_{\ell,gh} = \frac{1}{\Lambda_x} \frac{1}{\Lambda_y} \int_0^{\Lambda_x} \int_0^{\Lambda_y} \varepsilon_{\ell}^{-1}(x, y) \exp\left(-j \left(\frac{2\pi gx}{\Lambda_x} + \frac{2\pi hy}{\Lambda_y}\right)\right) dx dy. \quad (\text{A.4})$$

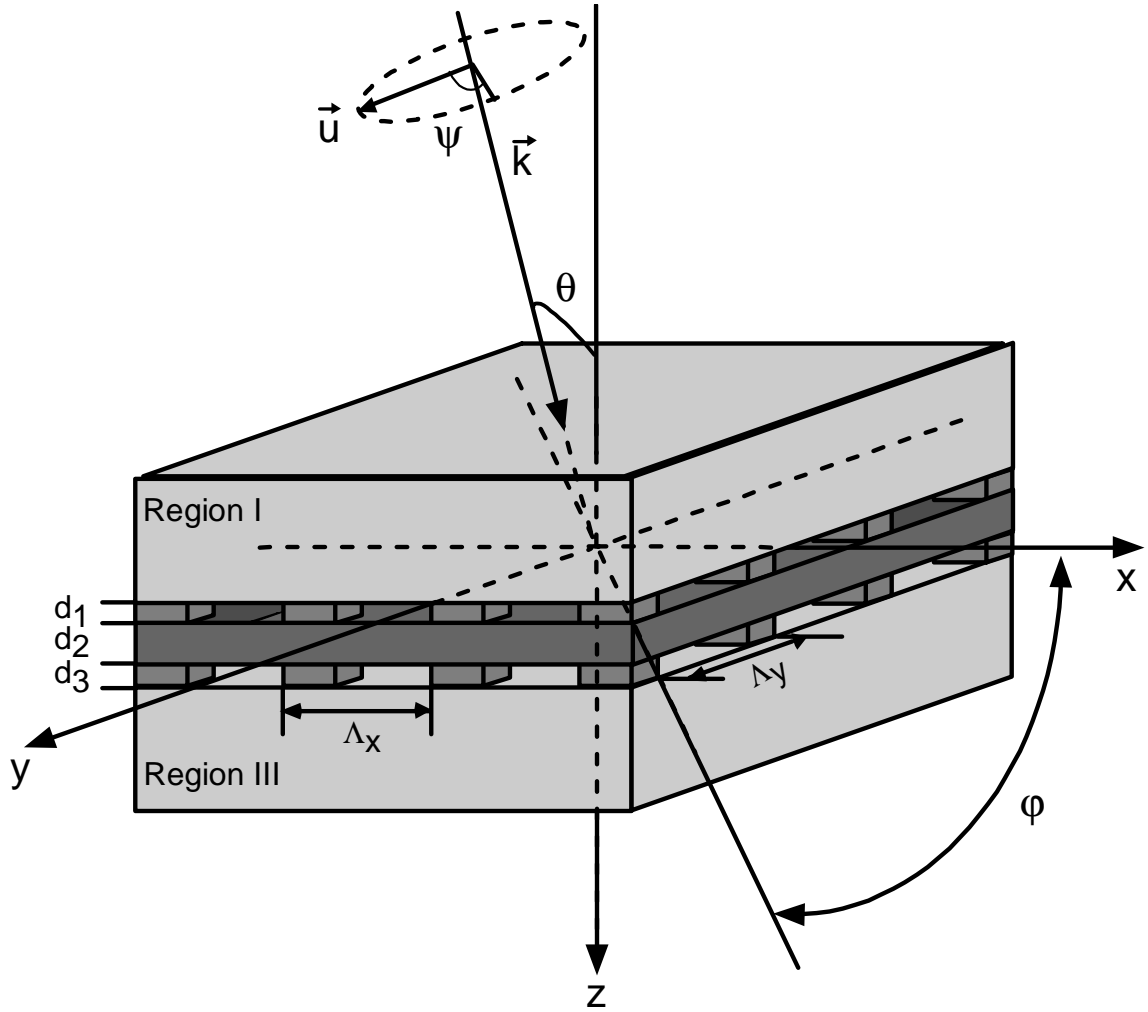


Figure A.1 Geometry of three-dimensional RCWA algorithm for multi-layer stack with two-dimensional gratings and homogeneous layer in arbitrary order

The electric field of an incident unit-amplitude plane wave with arbitrary linear polarization is given by

$$\vec{E}_{inc}(x, y, z) = \hat{u} \exp(-j\vec{k}_1 \cdot \vec{r}). \quad (\text{A.5})$$

A time dependence of $\exp(j\omega t)$ is assumed and omitted everywhere. The wave vector in the incident region, \vec{k}_1 , is given by

$$\vec{k}_1 = k_0 n_1 (\sin \theta \cos \varphi \hat{x} + \sin \theta \sin \varphi \hat{y} + \cos \theta \hat{z}), \quad (\text{A.6})$$

in which $k_0 = \frac{2\pi}{\lambda_0}$ and λ_0 is the vacuum wavelength of the incident wave. The unit polarization vector \hat{u} of the incident wave is given in terms of the angles θ, φ, ψ (which are defined in Figure A.1).

$$\begin{aligned} \hat{u} &= u_x \hat{x} + u_y \hat{y} + u_z \hat{z} \\ &= (\cos \psi \cos \theta \cos \varphi - \sin \psi \sin \varphi) \hat{x} + \\ &\quad (\cos \psi \cos \theta \sin \varphi + \sin \psi \cos \varphi) \hat{y} - (\cos \psi \sin \theta) \hat{z} \end{aligned}, \quad (\text{A.7})$$

in which θ is the polar angle and φ is the azimuth angle. The angle between the electric field vector and the incident plane is ψ .

B. Field expressions for each region

The electric fields in the incident region and the exit region can be expressed in terms of Rayleigh expansions:

$$\vec{E}_I = \vec{E}_{inc} + \sum_{m=-\infty}^{\infty} \sum_{n=-\infty}^{\infty} \vec{R}_{mn} \exp[-j(k_{xm}x + k_{yn}y - k_{Lz,mn}z)], \quad (\text{A.8})$$

$$\vec{E}_{III} = \sum_{m=-\infty}^{\infty} \sum_{n=-\infty}^{\infty} \vec{T}_{mn} \exp\{-j[k_{xm}x + k_{yn}y + k_{Lz,mn}(z - Z_L)]\}, \quad (\text{A.9})$$

in which \vec{R}_{mn} and \vec{T}_{mn} are the electric fields of mn-th reflected and transmitted orders respectively. The wave vector components $k_{x,m}$ and $k_{y,n}$ arise from phase matching and the Floquet conditions and are given by

$$k_{x,m} = k_0 [n_1 \sin \theta \cos \varphi - m(\lambda_0 / \Lambda_x)], \quad (\text{A.10})$$

$$k_{y,n} = k_0 [n_1 \sin \theta \sin \varphi - n(\lambda_0 / \Lambda_y)], \quad (\text{A.11})$$

and

$$k_{l_z, mn} = \begin{cases} k_0 \left[n_l^2 - (k_{xm}/k_0)^2 - (k_{yn}/k_0)^2 \right]^{1/2} & n_l > \left[(k_{xm}/k_0)^2 - (k_{yn}/k_0)^2 \right]^{1/2} \\ -jk_0 \left[(k_{xm}/k_0)^2 + (k_{yn}/k_0)^2 - n_l^2 \right]^{1/2} & n_l < \left[(k_{xm}/k_0)^2 - (k_{yn}/k_0)^2 \right]^{1/2} \end{cases} \quad l = \text{I, III}. \quad (\text{A.12})$$

In the grating regions, the fields may be expressed as a Fourier expansion in terms of the spatial harmonics

$$\vec{E}_\ell = \sum_{m=-\infty}^{\infty} \sum_{n=-\infty}^{\infty} \vec{S}_{\ell, mn}(z) \exp[-j(k_{xm}x + k_{yn}y)], \quad (\text{A.13})$$

$$\vec{H}_\ell = -j \left(\frac{\epsilon_0}{\mu_0} \right)^{1/2} \sum_{m=-\infty}^{\infty} \sum_{n=-\infty}^{\infty} \vec{U}_{\ell, mn}(z) \exp[-j(k_{xm}x + k_{yn}y)], \quad (\text{A.14})$$

in which ϵ_0 and μ_0 are the permittivity and permeability of free space, respectively. $\vec{S}_{\ell, mn}$ and $\vec{U}_{\ell, mn}$ are the amplitudes of the spatial harmonics of the fields such that \vec{E}_ℓ and \vec{H}_ℓ satisfy Maxwell's equations in the ℓ th grating layer

$$\nabla \times \vec{E}_\ell = -j\omega\mu\vec{H}_\ell, \quad (\text{A.15})$$

$$\nabla \times \vec{H}_\ell = j\omega\epsilon_0\epsilon_\ell(x, y)\vec{E}_\ell. \quad (\text{A.16})$$

Substituting Equations A.13 and A.14 into Equations A.15 and A.16 and eliminating the z components of the fields, an infinite set of first order differential equations can be derived

$$\frac{\partial S_{\ell, ymn}(z)}{\partial z'} = U_{\ell, xmn}(z) + \frac{k_{yn}}{k_0^2} \sum_{p=-\infty}^{\infty} \sum_{q=-\infty}^{\infty} A_{\ell, m-p, n-q} (-k_{yq} U_{\ell, xpq} + k_{xp} U_{\ell, ypq}), \quad (\text{A.17a})$$

$$\frac{\partial S_{\ell, xmn}(z)}{\partial z'} = -U_{\ell, ymn}(z) + \frac{k_{xm}}{k_0^2} \sum_{p=-\infty}^{\infty} \sum_{q=-\infty}^{\infty} A_{\ell, m-p, n-q} (-k_{yq} U_{\ell, xpq} + k_{xp} U_{\ell, ypq}), \quad (\text{A.17b})$$

$$\frac{\partial U_{\ell, ymn}(z)}{\partial z'} = \sum_{p=-\infty}^{\infty} \sum_{q=-\infty}^{\infty} \epsilon_{\ell, m-p, n-q} S_{\ell, xpq} + \frac{k_{yn}}{k_0^2} (k_{xm} S_{\ell, ymn} - k_{yn} S_{\ell, xmn}), \quad (\text{A.17c})$$

$$\frac{\partial U_{\ell, xmn}(z)}{\partial z'} = -\sum_{p=-\infty}^{\infty} \sum_{q=-\infty}^{\infty} \epsilon_{\ell, m-p, n-q} S_{\ell, ypq} + \frac{k_{xm}}{k_0^2} (k_{xm} S_{\ell, ymn} - k_{yn} S_{\ell, xmn}), \quad (\text{A.17d})$$

in which $z' = k_0 z$ and $p = m - g, q = n - h$. The indices m and n run over the different diffraction orders, while g and h run over the Fourier harmonics of the permittivity and its

inverse. In order to numerically solve this set of coupled differential equations, the set is truncated to finite size and expressed in matrix form as

$$\frac{\partial}{\partial z'} \begin{bmatrix} \mathbf{S}_{\ell,y} \\ \mathbf{S}_{\ell,x} \\ \mathbf{U}_{\ell,y} \\ \mathbf{U}_{\ell,x} \end{bmatrix} = \begin{bmatrix} \mathbf{0} & \mathbf{0} & \mathbf{P}_{\ell,11} & \mathbf{P}_{\ell,12} \\ \mathbf{0} & \mathbf{0} & \mathbf{P}_{\ell,21} & \mathbf{P}_{\ell,22} \\ \mathbf{Q}_{\ell,11} & \mathbf{Q}_{\ell,12} & \mathbf{0} & \mathbf{0} \\ \mathbf{Q}_{\ell,21} & \mathbf{Q}_{\ell,22} & \mathbf{0} & \mathbf{0} \end{bmatrix} \begin{bmatrix} \mathbf{S}_{\ell,y} \\ \mathbf{S}_{\ell,x} \\ \mathbf{U}_{\ell,y} \\ \mathbf{U}_{\ell,x} \end{bmatrix}, \quad (\text{A.18a})$$

in which

$$\mathbf{P}_\ell = \begin{bmatrix} \mathbf{P}_{\ell,11} & \mathbf{P}_{\ell,12} \\ \mathbf{P}_{\ell,21} & \mathbf{P}_{\ell,22} \end{bmatrix} = \begin{bmatrix} \mathbf{k}_y \boldsymbol{\varepsilon}_\ell^{-1} \mathbf{k}_x & \mathbf{I} - \mathbf{k}_y \boldsymbol{\varepsilon}_\ell^{-1} \mathbf{k}_y \\ \mathbf{k}_x \boldsymbol{\varepsilon}_\ell^{-1} \mathbf{k}_x - \mathbf{I} & -\mathbf{k}_x \boldsymbol{\varepsilon}_\ell^{-1} \mathbf{k}_y \end{bmatrix}, \quad (\text{A.18b})$$

$$\mathbf{Q}_\ell = \begin{bmatrix} \mathbf{Q}_{\ell,11} & \mathbf{Q}_{\ell,12} \\ \mathbf{Q}_{\ell,21} & \mathbf{Q}_{\ell,22} \end{bmatrix} = \begin{bmatrix} \mathbf{k}_x \mathbf{k}_y & \boldsymbol{\alpha} \mathbf{A}_\ell^{-1} + (\mathbf{1} - \boldsymbol{\alpha}) \boldsymbol{\varepsilon}_\ell - \mathbf{k}_y^2 \\ \mathbf{k}_x^2 - \boldsymbol{\alpha} \boldsymbol{\varepsilon}_\ell - (\mathbf{1} - \boldsymbol{\alpha}) \mathbf{A}_\ell^{-1} & -\mathbf{k}_x \mathbf{k}_y \end{bmatrix}. \quad (\text{A.18c})$$

Here, $\boldsymbol{\varepsilon}_\ell$ and \mathbf{A}_ℓ are the permittivity and inverse permittivity matrices which consist of harmonic coefficients $\varepsilon_{\ell,gh}$ and $A_{\ell,gh}$ defined in Equations A.3 and A.4. The diagonal matrices \mathbf{k}_x and \mathbf{k}_y are formed by the elements k_{xm}/k_0 and k_{yn}/k_0 . If M and N are the number of spatial harmonics retained along the x and y directions, then \mathbf{I} is the identity matrix of dimension MN. Note here the improved eigenvalue formulation proposed by Lalanne [65], is adopted, in which a grating geometry dependent parameter α is introduced, which is a real positive number in the interval of [0,1].

To improve computational efficiency, Equation A.18 can be further reduced to two second-order equations, shown here in matrix form as

$$\begin{bmatrix} \partial^2 \mathbf{S}_{\ell,y} / \partial z'^2 \\ \partial^2 \mathbf{S}_{\ell,x} / \partial z'^2 \end{bmatrix} = \boldsymbol{\Omega}_\ell \begin{bmatrix} \mathbf{S}_{\ell,y} \\ \mathbf{S}_{\ell,x} \end{bmatrix}, \quad (\text{A.19})$$

$$\boldsymbol{\Omega}_\ell = \begin{bmatrix} \mathbf{k}_x^2 + \mathbf{D}[\boldsymbol{\alpha} \boldsymbol{\varepsilon}_\ell + (\mathbf{1} - \boldsymbol{\alpha}) \mathbf{A}_\ell^{-1}] & \mathbf{k}_y \left\{ \boldsymbol{\varepsilon}_\ell^{-1} \mathbf{k}_x [\boldsymbol{\alpha} \mathbf{A}_\ell^{-1} + (\mathbf{1} - \boldsymbol{\alpha}) \boldsymbol{\varepsilon}_\ell] - \mathbf{k}_x \right\} \\ \mathbf{k}_x \left\{ \boldsymbol{\varepsilon}_\ell^{-1} \mathbf{k}_y [\boldsymbol{\alpha} \boldsymbol{\varepsilon}_\ell + (\mathbf{1} - \boldsymbol{\alpha}) \mathbf{A}_\ell^{-1}] - \mathbf{k}_y \right\} & \mathbf{k}_y^2 + \mathbf{B}[\boldsymbol{\alpha} \mathbf{A}_\ell^{-1} + (\mathbf{1} - \boldsymbol{\alpha}) \boldsymbol{\varepsilon}_\ell] \end{bmatrix}, \quad (\text{A.20})$$

in which $\mathbf{B} = \mathbf{k}_x \boldsymbol{\varepsilon}_\ell^{-1} \mathbf{k}_x - \mathbf{I}$ and $\mathbf{D} = \mathbf{k}_y \boldsymbol{\varepsilon}_\ell^{-1} \mathbf{k}_y - \mathbf{I}$.

C. Eigenvalue solution of the fields in the grating and homogeneous layers

As in the standard RCWA implementation, the coupled-wave equations of Equation A.19 are solved by finding the eigenvalues and eigenvectors of $\mathbf{\Omega}_\ell$, which is a matrix of rank $2MN$. Compared to the eigenvalue problem of Equation A.18, which is of rank $4MN$, the computational efficiency is improved by a factor of 8.

The spatial harmonics of the tangential electric field in the grating layers may be written as

$$S_{\ell,ymn}(z) = \sum_{i=1}^{2MN} w_{\ell 1,mi} \left\{ c_{\ell,i}^+ \exp(-k_0 \sigma_{\ell,i} (z - Z_{\ell-1})) + c_{\ell,i}^- \exp[k_0 \sigma_{\ell,i} (z - Z_\ell)] \right\}, \quad (\text{A.21})$$

$$S_{\ell,xmn}(z) = \sum_{i=1}^{2MN} w_{\ell 2,mi} \left\{ c_{\ell,i}^+ \exp(-k_0 \sigma_{\ell,i} (z - Z_{\ell-1})) + c_{\ell,i}^- \exp[k_0 \sigma_{\ell,i} (z - Z_\ell)] \right\}, \quad (\text{A.22})$$

in which the w 's are elements of \mathbf{W}_ℓ , the eigenvector matrix, and the σ 's are elements of $\mathbf{\Sigma}$, which is the diagonal matrix of the positive square roots of the eigenvalues of $\mathbf{\Omega}_\ell$. The c 's are $4MN$ unknown coefficients that will be determined from matching the boundary conditions at the appropriate interfaces. In Equations A.21 and A.22, Z_ℓ represents the cumulative depth of the structure to ℓ th layer and is given by

$$Z_\ell = \sum_{\ell'=1}^{\ell} d_{\ell'}, \quad (\text{A.23})$$

in which $d_{\ell'}$ is the thickness of the ℓ' th layer.

Equations A.21 and A.22 can be written into matrix form as

$$\mathbf{S}_{\ell,y} = \mathbf{W}_{\ell,1} (\mathbf{X}_{\ell,1} \mathbf{C}_\ell^+ + \mathbf{X}_{\ell,2} \mathbf{C}_\ell^-), \quad (\text{A.24})$$

$$\mathbf{S}_{\ell,x} = \mathbf{W}_{\ell,2} (\mathbf{X}_{\ell,1} \mathbf{C}_\ell^+ + \mathbf{X}_{\ell,2} \mathbf{C}_\ell^-), \quad (\text{A.25})$$

in which

$$\begin{bmatrix} \mathbf{W}_{\ell,1} \\ \mathbf{W}_{\ell,2} \end{bmatrix} = \mathbf{W}_\ell, \quad (\text{A.26})$$

and $\mathbf{X}_{\ell,1}$, $\mathbf{X}_{\ell,2}$ are $2MN \times 2MN$ diagonal matrices with diagonal elements equal to $\exp(-k_0 \sigma_{\ell,1} (z - Z_{\ell-1}))$ and $\exp(k_0 \sigma_{\ell,2} (z - Z_\ell))$, respectively.

The magnetic fields in the grating layers can be easily deduced by substituting Equations A.24 and A.25 into Equation A.18, which can be written as

$$\mathbf{U}_{\ell,y} = \mathbf{V}_{\ell,1} (-\mathbf{X}_{\ell,1} \mathbf{C}_\ell^+ + \mathbf{X}_{\ell,2} \mathbf{C}_\ell^-), \quad (\text{A.27})$$

$$\mathbf{U}_{\ell,x} = \mathbf{V}_{\ell,2} (-\mathbf{X}_{\ell,1} \mathbf{C}_\ell^+ + \mathbf{X}_{\ell,2} \mathbf{C}_\ell^-), \quad (\text{A.28})$$

in which

$$\mathbf{V}_{\ell,1} = (\mathbf{Q}_{\ell,11} \mathbf{W}_{\ell,1} + \mathbf{Q}_{\ell,12} \mathbf{W}_{\ell,2}) \boldsymbol{\Sigma}_\ell^{-1}, \quad (\text{A.29})$$

$$\mathbf{V}_{\ell,2} = (\mathbf{Q}_{\ell,21} \mathbf{W}_{\ell,1} + \mathbf{Q}_{\ell,22} \mathbf{W}_{\ell,2}) \boldsymbol{\Sigma}_\ell^{-1}. \quad (\text{A.30})$$

Equations A.24, A.25, A.27 and A.28 may be combined as

$$\begin{bmatrix} \mathbf{S}_{\ell,y} \\ \mathbf{S}_{\ell,x} \\ \mathbf{U}_{\ell,y} \\ \mathbf{U}_{\ell,x} \end{bmatrix} = \begin{bmatrix} \mathbf{W}_{\ell,1} \mathbf{X}_{\ell,1} & \mathbf{W}_{\ell,1} \mathbf{X}_{\ell,2} \\ \mathbf{W}_{\ell,2} \mathbf{X}_{\ell,1} & \mathbf{W}_{\ell,2} \mathbf{X}_{\ell,2} \\ -\mathbf{V}_{\ell,1} \mathbf{X}_{\ell,1} & \mathbf{V}_{\ell,1} \mathbf{X}_{\ell,2} \\ -\mathbf{V}_{\ell,2} \mathbf{X}_{\ell,1} & \mathbf{V}_{\ell,2} \mathbf{X}_{\ell,2} \end{bmatrix} \begin{bmatrix} \mathbf{C}_\ell^+ \\ \mathbf{C}_\ell^- \end{bmatrix}. \quad (\text{A.31})$$

Similarly, it is easy to show that the spatial harmonics in the homogeneous layers may be expressed as

$$\begin{bmatrix} \mathbf{S}_{\ell,y} \\ \mathbf{S}_{\ell,x} \\ \mathbf{U}_{\ell,y} \\ \mathbf{U}_{\ell,x} \end{bmatrix} = \begin{bmatrix} \mathbf{X}'_{\ell,1} & \mathbf{0} & \mathbf{X}'_{\ell,2} & \mathbf{0} \\ \mathbf{0} & \mathbf{X}'_{\ell,1} & \mathbf{0} & \mathbf{X}'_{\ell,2} \\ \mathbf{j} \mathbf{k}_x \mathbf{k}_y \Gamma_\ell^{-1} \mathbf{X}'_{\ell,1} & \mathbf{j} \mathbf{G}_{\ell,2} \Gamma_\ell^{-1} \mathbf{X}'_{\ell,1} & -\mathbf{j} \mathbf{k}_x \mathbf{k}_y \Gamma_\ell^{-1} \mathbf{X}'_{\ell,2} & -\mathbf{j} \mathbf{G}_{\ell,2} \Gamma_\ell^{-1} \mathbf{X}'_{\ell,2} \\ -\mathbf{j} \mathbf{G}_{\ell,1} \Gamma_\ell^{-1} \mathbf{X}'_{\ell,1} & -\mathbf{j} \mathbf{k}_x \mathbf{k}_y \Gamma_\ell^{-1} \mathbf{X}'_{\ell,1} & \mathbf{j} \mathbf{G}_{\ell,1} \Gamma_\ell^{-1} \mathbf{X}'_{\ell,2} & \mathbf{j} \mathbf{k}_x \mathbf{k}_y \Gamma_\ell^{-1} \mathbf{X}'_{\ell,2} \end{bmatrix} \begin{bmatrix} \mathbf{C}_\ell^+ \\ \mathbf{C}_\ell^- \end{bmatrix}, \quad (\text{A.32})$$

in which Γ_ℓ is a diagonal matrix with diagonal elements.

$$\gamma_{\ell,mm} = \begin{cases} \left[n_\ell^2 - \left(\frac{k_{xm}}{k_0} \right)^2 - \left(\frac{k_{yn}}{k_0} \right)^2 \right]^{1/2}, & \left(\frac{k_{xm}}{k_0} \right)^2 + \left(\frac{k_{yn}}{k_0} \right)^2 < n_\ell^2 \\ \left[-n_\ell^2 + \left(\frac{k_{xm}}{k_0} \right)^2 + \left(\frac{k_{yn}}{k_0} \right)^2 \right]^{1/2}, & \left(\frac{k_{xm}}{k_0} \right)^2 + \left(\frac{k_{yn}}{k_0} \right)^2 > n_\ell^2 \end{cases} \quad (\text{A.33})$$

and $\mathbf{X}'_{\ell,1}, \mathbf{X}'_{\ell,2}$ are also diagonal matrices with diagonal elements $\exp(-k_0 \gamma_{\ell,mm} (z - Z_{\ell-1}))$ and $\exp(k_0 \gamma_{\ell,mm} (z - Z_\ell))$, respectively. Also

$$\mathbf{G}_{\ell,1} = \boldsymbol{\varepsilon}_{r,\ell} - \mathbf{k}_x^2, \quad (\text{A.34})$$

$$\mathbf{G}_{\ell,2} = \boldsymbol{\varepsilon}_{r,\ell} - \mathbf{k}_y^2. \quad (\text{A.35})$$

D. Boundary conditions

To compute the field values in the reflected and transmitted regions, the tangential electric and magnetic fields are matched at each boundary. As an example, consider the case shown in Figure A.1. The matrix expression for the incident beam at the first boundary, $z = 0$, which is a grating layer in Figure A.1, is

$$\begin{aligned} & \begin{bmatrix} u_x \delta_{m0} \delta_{n0} \\ u_y \delta_{m0} \delta_{n0} \\ \delta_{m0} \delta_{n0} (k_{y00} u_z - n_1 \cos \theta u_y) \\ \delta_{m0} \delta_{n0} (n_1 \cos \theta u_x - k_{x00} u_z) \end{bmatrix} + \begin{bmatrix} \mathbf{I} & \mathbf{0} \\ \mathbf{0} & \mathbf{I} \\ \frac{\mathbf{k}_x \mathbf{k}_y}{k_x^2 + k_y^2} & \frac{\mathbf{k}_z^2 + k_z^2}{k_y^2 + k_z^2} \\ \frac{\mathbf{k}_z}{k_x^2 + k_z^2} & \frac{\mathbf{k}_z}{k_x^2 + k_z^2} \\ -\frac{\mathbf{k}_x^2 + k_x^2}{k_z} & -\frac{\mathbf{k}_x \mathbf{k}_y}{k_z} \\ \frac{\mathbf{k}_z}{k_z} & \frac{\mathbf{k}_z}{k_z} \end{bmatrix} \begin{bmatrix} \mathbf{R}_x \\ \mathbf{R}_y \end{bmatrix}, \\ & = \begin{bmatrix} \mathbf{W}_{1,2} & \mathbf{W}_{1,2} \mathbf{X}_1 \\ \mathbf{W}_{1,1} & \mathbf{W}_{1,1} \mathbf{X}_1 \\ \mathbf{jV}_{1,2} & -\mathbf{jV}_{1,2} \mathbf{X}_1 \\ \mathbf{jV}_{1,1} & -\mathbf{jV}_{1,1} \mathbf{X}_1 \end{bmatrix} \begin{bmatrix} \mathbf{C}_1^+ \\ \mathbf{C}_1^- \end{bmatrix} \end{aligned} \quad (\text{A.36})$$

in which \mathbf{X}_1 is a diagonal matrix whose elements are $\exp(-k_0 \delta_{1,i} d_1)$, \mathbf{I} is the identity matrix, and

$\mathbf{k}_{\mathbf{I}z}$ is a diagonal matrix with elements equal to $k_{\mathbf{I}z,mm}/k_0$ and δ_{mm} denotes the Kronecker delta

function. $\begin{bmatrix} \mathbf{R}_x \\ \mathbf{R}_y \end{bmatrix}$ is a column vector formed by tangential components of electric field $\begin{bmatrix} \mathbf{E}_x \\ \mathbf{E}_y \end{bmatrix}$ in

Region I.

For the next boundary, $z = Z_1$, which is a transition from a grating layer to a homogeneous layer in Figure A.1, we have

$$\begin{aligned} & \begin{bmatrix} \mathbf{W}_{1,2}\mathbf{X}_1 & \mathbf{W}_{1,2} \\ \mathbf{W}_{1,1}\mathbf{X}_1 & \mathbf{W}_{1,1} \\ \mathbf{jV}_{1,2}\mathbf{X}_1 & -\mathbf{jV}_{1,2} \\ \mathbf{jV}_{1,1}\mathbf{X}_1 & -\mathbf{jV}_{1,1} \end{bmatrix} \begin{bmatrix} \mathbf{C}_1^+ \\ \mathbf{C}_1^- \end{bmatrix} \\ &= \begin{bmatrix} \mathbf{0} & \mathbf{I} \\ \mathbf{I} & \mathbf{0} \\ -\mathbf{jG}_{2,1}\Gamma_2^{-1} & -\mathbf{jk}_x\mathbf{k}_y\Gamma_2^{-1} \\ \mathbf{jk}_x\mathbf{k}_y\Gamma_2^{-1} & \mathbf{jG}_{2,2}\Gamma_2^{-1} \end{bmatrix} \begin{bmatrix} \mathbf{0} & \mathbf{X}'_2 \\ \mathbf{X}'_2 & \mathbf{0} \\ \mathbf{jG}_{2,1}\Gamma_2^{-1}\mathbf{X}'_2 & \mathbf{jk}_x\mathbf{k}_y\Gamma_2^{-1}\mathbf{X}'_2 \\ -\mathbf{jk}_x\mathbf{k}_y\Gamma_2^{-1}\mathbf{X}'_2 & -\mathbf{jG}_{2,2}\Gamma_2^{-1}\mathbf{X}'_2 \end{bmatrix} \begin{bmatrix} \mathbf{C}_2^+ \\ \mathbf{C}_2^- \end{bmatrix}, \end{aligned} \quad (\text{A.37})$$

in which \mathbf{X}'_2 is a diagonal matrix with elements $\exp(-k_0\gamma_{2,mn}d_2)$ and d_2 is the thickness of the homogeneous layer. At $z = Z_2$, the boundary represents a transition from a homogeneous layer back to a grating layer:

$$\begin{aligned} & \begin{bmatrix} \mathbf{0} & \mathbf{X}'_2 & \mathbf{0} & \mathbf{I} \\ \mathbf{X}'_2 & \mathbf{0} & \mathbf{I} & \mathbf{0} \\ -\mathbf{jG}_{2,1}\Gamma_2^{-1}\mathbf{X}'_2 & -\mathbf{jk}_x\mathbf{k}_y\Gamma_2^{-1}\mathbf{X}'_2 & \mathbf{jG}_{2,1}\Gamma_2^{-1} & \mathbf{jk}_x\mathbf{k}_y\Gamma_2^{-1} \\ \mathbf{jk}_x\mathbf{k}_y\Gamma_2^{-1}\mathbf{X}'_2 & \mathbf{jG}_{2,2}\Gamma_2^{-1}\mathbf{X}'_2 & -\mathbf{jk}_x\mathbf{k}_y\Gamma_2^{-1} & -\mathbf{jG}_{2,2}\Gamma_2^{-1} \end{bmatrix} \begin{bmatrix} \mathbf{C}_2^+ \\ \mathbf{C}_2^- \end{bmatrix} \\ &= \begin{bmatrix} \mathbf{W}_{3,2} & \mathbf{W}_{3,2}\mathbf{X}_3 \\ \mathbf{W}_{3,1} & \mathbf{W}_{3,1}\mathbf{X}_3 \\ \mathbf{jV}_{3,2} & -\mathbf{jV}_{3,2}\mathbf{X}_3 \\ \mathbf{jV}_{3,1} & -\mathbf{jV}_{3,1}\mathbf{X}_3 \end{bmatrix} \begin{bmatrix} \mathbf{C}_3^+ \\ \mathbf{C}_3^- \end{bmatrix}. \end{aligned} \quad (\text{A.38})$$

Continuing in the same manner to the last interface, $z = Z_L$, we have

$$\begin{bmatrix} \mathbf{W}_{3,2} \mathbf{X}_3 & \mathbf{W}_{3,2} \\ \mathbf{W}_{3,1} \mathbf{X}_3 & \mathbf{W}_{3,1} \\ \mathbf{jV}_{3,2} \mathbf{X}_3 & -\mathbf{jV}_{3,2} \\ \mathbf{jV}_{3,1} \mathbf{X}_3 & -\mathbf{jV}_{3,1} \end{bmatrix} \begin{bmatrix} \mathbf{C}_3^+ \\ \mathbf{C}_3^- \end{bmatrix} = \begin{bmatrix} \mathbf{I} & \mathbf{0} \\ \mathbf{0} & \mathbf{I} \\ -\frac{\mathbf{k}_x \mathbf{k}_y}{\mathbf{k}_{\text{III}z}} & -\frac{\mathbf{k}_y^2 + \mathbf{k}_{\text{III}z}^2}{\mathbf{k}_{\text{III}z}} \\ \frac{\mathbf{k}_x^2 + \mathbf{k}_{\text{III}z}^2}{\mathbf{k}_{\text{III}z}} & \frac{\mathbf{k}_x \mathbf{k}_y}{\mathbf{k}_{\text{III}z}} \end{bmatrix} \begin{bmatrix} \mathbf{T}_x \\ \mathbf{T}_y \end{bmatrix}, \quad (\text{A.39})$$

in which $\mathbf{k}_{\text{III}z}$ is a diagonal matrix with elements $k_{\text{III}z,mn}/k_0$ and $\begin{bmatrix} \mathbf{T}_x \\ \mathbf{T}_y \end{bmatrix}$ is a column vector

formed by tangential components of electric field $\begin{bmatrix} \mathbf{E}_x \\ \mathbf{E}_y \end{bmatrix}$ in Region III.

Note that regardless of whether a layer is homogeneous or a grating, a similar format can be seen for the matrix representing the field entering a layer:

$$\mathbf{M}_e = \begin{bmatrix} \mathbf{F}_{11} & \mathbf{F}_{12} \\ \mathbf{F}_{21} & \mathbf{F}_{22} \\ \mathbf{F}_{31} & \mathbf{F}_{32} \\ \mathbf{F}_{41} & \mathbf{F}_{42} \end{bmatrix} \begin{bmatrix} \mathbf{II} & \mathbf{0} \\ \mathbf{0} & \mathbf{X} \end{bmatrix} \begin{bmatrix} \mathbf{C}^+ \\ \mathbf{C}^- \end{bmatrix}, \quad (\text{A.40})$$

and for the field exiting a layer:

$$\mathbf{M}_x = \begin{bmatrix} \mathbf{F}_{11} & \mathbf{F}_{12} \\ \mathbf{F}_{21} & \mathbf{F}_{22} \\ \mathbf{F}_{31} & \mathbf{F}_{32} \\ \mathbf{F}_{41} & \mathbf{F}_{42} \end{bmatrix} \begin{bmatrix} \mathbf{X} & \mathbf{0} \\ \mathbf{0} & \mathbf{II} \end{bmatrix} \begin{bmatrix} \mathbf{C}^+ \\ \mathbf{C}^- \end{bmatrix}, \quad (\text{A.41})$$

in which \mathbf{F} is a general representation for the matrices of known coefficients (i.e., the eigenvectors), \mathbf{X} is a representation of the matrices of exponential components, and \mathbf{C} represents the unknown coefficients. \mathbf{II} is an identity matrix of dimension $2MN$.

The equations for the matched fields at each boundary can be solved simultaneously for

$\begin{bmatrix} \mathbf{R}_x \\ \mathbf{R}_y \end{bmatrix}$ and $\begin{bmatrix} \mathbf{T}_x \\ \mathbf{T}_y \end{bmatrix}$. However, this would be computationally inefficient for a large number of

layers. To reduce the size of the system of simultaneous equations, a standard transmittance

matrix approach can be applied to each successive layer in the structure. Beginning at the last

layer, the unknown coefficients for the layer can be determined in terms of $\begin{bmatrix} \mathbf{T}_x \\ \mathbf{T}_y \end{bmatrix}$:

$$\begin{bmatrix} \mathbf{C}_L^+ \\ \mathbf{C}_L^- \end{bmatrix} = \begin{bmatrix} \mathbf{F}_{L,11} \mathbf{X}_L & \mathbf{F}_{L,12} \\ \mathbf{F}_{L,21} \mathbf{X}_L & \mathbf{F}_{L,22} \\ \mathbf{F}_{L,31} \mathbf{X}_L & \mathbf{F}_{L,32} \\ \mathbf{F}_{L,41} \mathbf{X}_L & \mathbf{F}_{L,42} \end{bmatrix}^{-1} \begin{bmatrix} \mathbf{I} & \mathbf{0} \\ \mathbf{0} & \mathbf{I} \\ -\frac{\mathbf{k}_x \mathbf{k}_y}{\mathbf{k}_{IIIz}} & -\frac{\mathbf{k}_y^2 + \mathbf{k}_{IIIz}^2}{\mathbf{k}_{IIIz}} \\ \frac{\mathbf{k}_x^2 + \mathbf{k}_{IIIz}^2}{\mathbf{k}_{IIIz}} & \frac{\mathbf{k}_x \mathbf{k}_y}{\mathbf{k}_{IIIz}} \end{bmatrix} \begin{bmatrix} \mathbf{T}_x \\ \mathbf{T}_y \end{bmatrix}. \quad (\text{A.42})$$

Substituting Equation A.42 into the equation for the previous boundary gives

$$\begin{bmatrix} \mathbf{F}_{L-1,11} \mathbf{X}_{L-1} & \mathbf{F}_{L-1,12} \\ \mathbf{F}_{L-1,21} \mathbf{X}_{L-1} & \mathbf{F}_{L-1,22} \\ \mathbf{F}_{L-1,31} \mathbf{X}_{L-1} & \mathbf{F}_{L-1,32} \\ \mathbf{F}_{L-1,41} \mathbf{X}_{L-1} & \mathbf{F}_{L-1,42} \end{bmatrix} \begin{bmatrix} \mathbf{C}_{L-1}^+ \\ \mathbf{C}_{L-1}^- \end{bmatrix} = \begin{bmatrix} \mathbf{F}_{L,11} & \mathbf{F}_{L,12} \mathbf{X}_L \\ \mathbf{F}_{L,21} & \mathbf{F}_{L,22} \mathbf{X}_L \\ \mathbf{F}_{L,31} & \mathbf{F}_{L,32} \mathbf{X}_L \\ \mathbf{F}_{L,41} & \mathbf{F}_{L,42} \mathbf{X}_L \end{bmatrix} \begin{bmatrix} \mathbf{F}_{L,11} \mathbf{X}_L & \mathbf{F}_{L,12} \\ \mathbf{F}_{L,21} \mathbf{X}_L & \mathbf{F}_{L,22} \\ \mathbf{F}_{L,31} \mathbf{X}_L & \mathbf{F}_{L,32} \\ \mathbf{F}_{L,41} \mathbf{X}_L & \mathbf{F}_{L,42} \end{bmatrix}^{-1} \begin{bmatrix} \mathbf{I} & \mathbf{0} \\ \mathbf{0} & \mathbf{I} \\ -\frac{\mathbf{k}_x \mathbf{k}_y}{\mathbf{k}_{IIIz}} & -\frac{\mathbf{k}_y^2 + \mathbf{k}_{IIIz}^2}{\mathbf{k}_{IIIz}} \\ \frac{\mathbf{k}_x^2 + \mathbf{k}_{IIIz}^2}{\mathbf{k}_{IIIz}} & \frac{\mathbf{k}_x \mathbf{k}_y}{\mathbf{k}_{IIIz}} \end{bmatrix} \begin{bmatrix} \mathbf{T}_x \\ \mathbf{T}_y \end{bmatrix}. \quad (\text{A.43})$$

Continuing this procedure for canceling out the unknown coefficients \mathbf{C} 's, an expression representing the entire structure can be written as

$$\begin{bmatrix} u_x \delta_{m0} \delta_{n0} \\ u_y \delta_{m0} \delta_{n0} \\ \delta_{m0} \delta_{n0} (k_{y00} u_z - n_1 \cos \theta u_y) \\ \delta_{m0} \delta_{n0} (n_1 \cos \theta u_x - k_{x00} u_z) \end{bmatrix} + \begin{bmatrix} \mathbf{I} & \mathbf{0} \\ \mathbf{0} & \mathbf{I} \\ \frac{\mathbf{k}_x \mathbf{k}_y}{\mathbf{k}_{Iz}} & \frac{\mathbf{k}_y^2 + \mathbf{k}_{Iz}^2}{\mathbf{k}_{Iz}} \\ -\frac{\mathbf{k}_x^2 + \mathbf{k}_{Iz}^2}{\mathbf{k}_{Iz}} & \frac{\mathbf{k}_x \mathbf{k}_y}{\mathbf{k}_{Iz}} \end{bmatrix} \begin{bmatrix} \mathbf{R}_x \\ \mathbf{R}_y \end{bmatrix} = \prod_{\ell=1}^L \begin{bmatrix} \mathbf{F}_{\ell,11} & \mathbf{F}_{\ell,12} \mathbf{X}_\ell \\ \mathbf{F}_{\ell,21} & \mathbf{F}_{\ell,22} \mathbf{X}_\ell \\ \mathbf{F}_{\ell,31} & \mathbf{F}_{\ell,32} \mathbf{X}_\ell \\ \mathbf{F}_{\ell,41} & \mathbf{F}_{\ell,42} \mathbf{X}_\ell \end{bmatrix} \begin{bmatrix} \mathbf{F}_{\ell,11} \mathbf{X}_\ell & \mathbf{F}_{\ell,12} \\ \mathbf{F}_{\ell,21} \mathbf{X}_\ell & \mathbf{F}_{\ell,22} \\ \mathbf{F}_{\ell,31} \mathbf{X}_\ell & \mathbf{F}_{\ell,32} \\ \mathbf{F}_{\ell,41} \mathbf{X}_\ell & \mathbf{F}_{\ell,42} \end{bmatrix}^{-1} \begin{bmatrix} \mathbf{I} & \mathbf{0} \\ \mathbf{0} & \mathbf{I} \\ -\frac{\mathbf{k}_x \mathbf{k}_y}{\mathbf{k}_{IIIz}} & -\frac{\mathbf{k}_y^2 + \mathbf{k}_{IIIz}^2}{\mathbf{k}_{IIIz}} \\ \frac{\mathbf{k}_x^2 + \mathbf{k}_{IIIz}^2}{\mathbf{k}_{IIIz}} & \frac{\mathbf{k}_x \mathbf{k}_y}{\mathbf{k}_{IIIz}} \end{bmatrix} \begin{bmatrix} \mathbf{T}_x \\ \mathbf{T}_y \end{bmatrix}. \quad (\text{A.44})$$

Since the matrices representing each layer have been written using the generalized format, the ordering of grating and homogeneous layers may be arbitrary.

E. Extension of the enhanced transmittance matrix approach to 2-D gratings

As pointed by Moharam *et al.* [16], the standard transmittance matrix approach is not numerically stable. The source of the instability is the matrix inversion operation in Equation A.44. To show this, rewrite the right hand side of Equation A.44 as

$$\prod_{\ell=1}^L \begin{bmatrix} \mathbf{F}_{\ell,11} & \mathbf{F}_{\ell,12} \mathbf{X}_{\ell} \\ \mathbf{F}_{\ell,21} & \mathbf{F}_{\ell,22} \mathbf{X}_{\ell} \\ \mathbf{F}_{\ell,31} & \mathbf{F}_{\ell,32} \mathbf{X}_{\ell} \\ \mathbf{F}_{\ell,41} & \mathbf{F}_{\ell,42} \mathbf{X}_{\ell} \end{bmatrix} \begin{bmatrix} \mathbf{X}_{\ell} & \mathbf{0} \\ \mathbf{0} & \mathbf{\Pi} \end{bmatrix}^{-1} \begin{bmatrix} \mathbf{F}_{\ell,11} & \mathbf{F}_{\ell,12} \\ \mathbf{F}_{\ell,21} & \mathbf{F}_{\ell,22} \\ \mathbf{F}_{\ell,31} & \mathbf{F}_{\ell,32} \\ \mathbf{F}_{\ell,41} & \mathbf{F}_{\ell,42} \end{bmatrix}^{-1} \begin{bmatrix} \mathbf{I} & \mathbf{0} \\ \mathbf{0} & \mathbf{I} \\ -\frac{\mathbf{k}_x \mathbf{k}_y}{\mathbf{k}_{\text{III}z}} & -\frac{\mathbf{k}_y^2 + \mathbf{k}_{\text{III}z}^2}{\mathbf{k}_{\text{III}z}} \\ \frac{\mathbf{k}_x^2 + \mathbf{k}_{\text{III}z}^2}{\mathbf{k}_{\text{III}z}} & \frac{\mathbf{k}_x \mathbf{k}_y}{\mathbf{k}_{\text{III}z}} \end{bmatrix} \begin{bmatrix} \mathbf{T}_x \\ \mathbf{T}_y \end{bmatrix}. \quad (\text{A.45})$$

If one of the eigenvalues $\sigma_{\ell,i}$ is positive and large (growing wave), the corresponding diagonal elements of \mathbf{X}_{ℓ} , i.e., $\exp(-k_0 \sigma_{\ell,i} d_{\ell})$, will be virtually zero, making the whole matrix ill-conditioned. The inversion of an ill-conditioned matrix will cause a large numerical truncation error and therefore result in numerical instability.

To remove the instability problem associated with the standard transmittance matrix approach in the 1-D grating case, Moharam *et al.* [16] proposed an enhanced transmittance matrix approach. Here it is extended to 2-D gratings. For clarity, their notation is maintained.

First consider the matrices corresponding to the Lth layer in Equation A.44, by defining

$$\mathbf{f}_{L+1} = \begin{bmatrix} \mathbf{I} & \mathbf{0} \\ \mathbf{0} & \mathbf{I} \end{bmatrix}, \quad (\text{A.46})$$

$$\mathbf{g}_{L+1} = \begin{bmatrix} -\frac{\mathbf{k}_x \mathbf{k}_y}{\mathbf{k}_{\text{III}z}} & -\frac{\mathbf{k}_y^2 + \mathbf{k}_{\text{III}z}^2}{\mathbf{k}_{\text{III}z}} \\ \frac{\mathbf{k}_x^2 + \mathbf{k}_{\text{III}z}^2}{\mathbf{k}_{\text{III}z}} & \frac{\mathbf{k}_x \mathbf{k}_y}{\mathbf{k}_{\text{III}z}} \end{bmatrix}, \quad (\text{A.47})$$

$$\mathbf{T} = \begin{bmatrix} \mathbf{T}_x \\ \mathbf{T}_y \end{bmatrix}. \quad (\text{A.48})$$

These matrices can be rewritten by separating the matrix to be inverted as the product of two matrices

$$\begin{bmatrix} \mathbf{F}_{L,11} & \mathbf{F}_{L,12} \mathbf{X}_L \\ \mathbf{F}_{L,21} & \mathbf{F}_{L,22} \mathbf{X}_L \\ \mathbf{F}_{L,31} & \mathbf{F}_{L,32} \mathbf{X}_L \\ \mathbf{F}_{L,41} & \mathbf{F}_{L,42} \mathbf{X}_L \end{bmatrix} \begin{bmatrix} \mathbf{X}_L & \mathbf{0} \\ \mathbf{0} & \mathbf{II} \end{bmatrix}^{-1} \begin{bmatrix} \mathbf{F}_{L,11} & \mathbf{F}_{L,12} \\ \mathbf{F}_{L,21} & \mathbf{F}_{L,22} \\ \mathbf{F}_{L,31} & \mathbf{F}_{L,32} \\ \mathbf{F}_{L,41} & \mathbf{F}_{L,42} \end{bmatrix}^{-1} \begin{bmatrix} \mathbf{f}_{L+1} \\ \mathbf{g}_{L+1} \end{bmatrix} \mathbf{T}. \quad (\text{A.49})$$

As stated before, in Equation A.49, the matrix containing only the coefficients can be inverted without numerical difficulties. The numerical instability is from the inversion of the matrix containing \mathbf{X}_L . To avoid this, rewrite the last three matrices of Equation A.49 as

$$\begin{bmatrix} \mathbf{X}_L & \mathbf{0} \\ \mathbf{0} & \mathbf{II} \end{bmatrix}^{-1} \begin{bmatrix} \mathbf{a}_L \\ \mathbf{b}_L \end{bmatrix} \mathbf{T}, \quad (\text{A.50})$$

in which

$$\begin{bmatrix} \mathbf{a}_L \\ \mathbf{b}_L \end{bmatrix} = \begin{bmatrix} \mathbf{F}_{L,11} & \mathbf{F}_{L,12} \\ \mathbf{F}_{L,21} & \mathbf{F}_{L,22} \\ \mathbf{F}_{L,31} & \mathbf{F}_{L,32} \\ \mathbf{F}_{L,41} & \mathbf{F}_{L,42} \end{bmatrix}^{-1} \begin{bmatrix} \mathbf{f}_{L+1} \\ \mathbf{g}_{L+1} \end{bmatrix}. \quad (\text{A.51})$$

By making the substitution

$$\mathbf{T} = \mathbf{a}_L^{-1} \mathbf{X}_L \mathbf{T}_L, \quad (\text{A.52})$$

Equation A.50 can be further reduced to

$$\begin{bmatrix} \mathbf{II} \\ \mathbf{b}_L \mathbf{a}_L^{-1} \mathbf{X}_L \end{bmatrix} \mathbf{T}_L. \quad (\text{A.53})$$

Substituting Equation A.53 back into Equation A.49 and completing the multiplication, we obtain

$$\begin{bmatrix} \mathbf{f}_L \\ \mathbf{g}_L \end{bmatrix} \mathbf{T}_L, \quad (\text{A.54})$$

in which

$$\begin{bmatrix} \mathbf{f}_L \\ \mathbf{g}_L \end{bmatrix} = \begin{bmatrix} \mathbf{F}_{L,11} + \mathbf{F}_{L,12} \left(\mathbf{X}_L \mathbf{b}_L \mathbf{a}_L^{-1} \mathbf{X}_L \right) \\ \mathbf{F}_{L,21} + \mathbf{F}_{L,22} \left(\mathbf{X}_L \mathbf{b}_L \mathbf{a}_L^{-1} \mathbf{X}_L \right) \\ \mathbf{F}_{L,31} + \mathbf{F}_{L,32} \left(\mathbf{X}_L \mathbf{b}_L \mathbf{a}_L^{-1} \mathbf{X}_L \right) \\ \mathbf{F}_{L,41} + \mathbf{F}_{L,42} \left(\mathbf{X}_L \mathbf{b}_L \mathbf{a}_L^{-1} \mathbf{X}_L \right) \end{bmatrix}. \quad (\text{A.55})$$

This returns an expression for the last layer that is similar to the one initially found for the exiting interface. Applying the same procedure to the remaining layers results in a final equation for the whole grating stack:

$$\begin{bmatrix} u_x \delta_{m0} \delta_{n0} \\ u_y \delta_{m0} \delta_{n0} \\ \delta_{m0} \delta_{n0} (k_{y00} u_z - n_1 \cos \theta u_y) \\ \delta_{m0} \delta_{n0} (n_1 \cos \theta u_x - k_{x00} u_z) \end{bmatrix} + \begin{bmatrix} \mathbf{I} & \mathbf{0} \\ \mathbf{0} & \mathbf{I} \\ \frac{\mathbf{k}_x \mathbf{k}_y}{\mathbf{k}_{Lz}} & \frac{\mathbf{k}_y^2 + \mathbf{k}_{Lz}^2}{\mathbf{k}_{Lz}} \\ -\frac{\mathbf{k}_x^2 + \mathbf{k}_{Lz}^2}{\mathbf{k}_{Lz}} & -\frac{\mathbf{k}_x \mathbf{k}_y}{\mathbf{k}_{Lz}} \end{bmatrix} \begin{bmatrix} \mathbf{R}_x \\ \mathbf{R}_y \end{bmatrix} = \begin{bmatrix} \mathbf{f}_1 \\ \mathbf{g}_1 \end{bmatrix} \mathbf{T}_1. \quad (\text{A.56})$$

Equation A.56 can be solved for $\begin{bmatrix} \mathbf{R}_x \\ \mathbf{R}_y \end{bmatrix}$ and \mathbf{T}_1 with standard LU or QR decomposition without

any numerical difficulties. We can obtain $\begin{bmatrix} \mathbf{T}_x \\ \mathbf{T}_y \end{bmatrix}$ from

$$\mathbf{T} = \begin{bmatrix} \mathbf{T}_x \\ \mathbf{T}_y \end{bmatrix} = \mathbf{a}_L^{-1} \mathbf{X}_L \mathbf{a}_{L-1}^{-1} \mathbf{X}_{L-1} \cdots \mathbf{a}_2^{-1} \mathbf{X}_2 \mathbf{a}_1^{-1} \mathbf{X}_1 \mathbf{T}_1. \quad (\text{A.57})$$

After solving for $\begin{bmatrix} \mathbf{R}_x \\ \mathbf{R}_y \end{bmatrix}$ and $\begin{bmatrix} \mathbf{T}_x \\ \mathbf{T}_y \end{bmatrix}$, the R_z and T_z components can be obtained by

invoking

$$\vec{k}_I \cdot \vec{R} = 0, \quad (\text{A.58})$$

$$\vec{k}_{III} \cdot \vec{T} = 0. \quad (\text{A.59})$$

Thus, the whole diffraction problem of the stack of arbitrarily ordered 2-D grating and homogeneous layers is solved.

F. Diffraction efficiency

The diffraction efficiency (DE) of each reflected and transmitted order is defined as the z component of the time-averaged Poynting vector and is related to the electric field components by the following relations:

$$DE_{R,mm} = \operatorname{Re} \left(\frac{k_{Iz,mm}}{k_I \cos \theta} \right) |\vec{R}_{mm}|^2, \quad (\text{A.60})$$

$$DE_{T,mm} = \operatorname{Re} \left(\frac{k_{IIIz,mm}}{k_{III} \cos \theta} \right) |\vec{T}_{mm}|^2. \quad (\text{A.61})$$

APPENDIX B

**MATHEMATICAL MODIFICATIONS TO THREE-DIMENSIONAL RCWA
ALGORITHM FOR SRG-RCWA ALGORITHM**

In SRG-RCWA, the arbitrary sampling frequencies f_{sx} and f_{sy} along the x and y direction are used, instead of $1/\Lambda_x$ and $1/\Lambda_y$ in the standard 3-D RCWA. To utilize 3-D RCWA, Equations A.1-A.4 and A.10, A.11 must be modified as

$$\varepsilon_\ell(x, y) = \sum_{g,h} \varepsilon_{\ell,gh} \exp(j(2\pi g f_{sx} x + 2\pi h f_{sy} y)), \quad (\text{B.1})$$

$$\varepsilon_\ell^{-1}(x, y) = \sum_{g,h} A_{\ell,gh} \exp(j(2\pi g f_{sx} x + 2\pi h f_{sy} y)), \quad (\text{B.2})$$

$$\varepsilon_{\ell,gh} = \frac{1}{\Lambda_{sx}} \cdot \frac{1}{\Lambda_{sy}} \cdot \int_0^{\Lambda_{sx}} \int_0^{\Lambda_{sy}} \varepsilon_\ell(x, y) \cdot \exp(-j(2\pi g f_{sx} x + 2\pi h f_{sy} y)) \cdot dx dy \quad (\text{B.3})$$

$$A_{\ell,gh} = \frac{1}{\Lambda_{sx}} \cdot \frac{1}{\Lambda_{sy}} \cdot \int_0^{\Lambda_{sx}} \int_0^{\Lambda_{sy}} \varepsilon_\ell^{-1}(x, y) \cdot \exp(-j(2\pi g f_{sx} x + 2\pi h f_{sy} y)) \cdot dx dy, \quad (\text{B.4})$$

$$k_{xm} = k_0 [n_1 \sin \theta \cos \varphi - m(\lambda_0 f_{sx})], \text{ and} \quad (\text{B.5})$$

$$k_{yn} = k_0 [n_1 \sin \theta \sin \varphi - n(\lambda_0 f_{sy})]. \quad (\text{B.6})$$

where $\Lambda_{sx} = \frac{1}{f_{sx}}$ and $\Lambda_{sy} = \frac{1}{f_{sy}}$.

It should be pointed out that one can greatly improve the computational efficiency by using 1-D integration to get $\varepsilon_{\ell,gh}$ and $A_{\ell,gh}$ instead of 2-D integration (B.3, B.4),

$$\varepsilon_{\ell,g'} = \frac{1}{\Lambda} \int_0^\Lambda \varepsilon_\ell(x') \exp(-j \frac{2\pi}{\Lambda} g' x') dx', \quad (\text{B.7})$$

$$A_{\ell,g'} = \frac{1}{\Lambda} \int_0^\Lambda \varepsilon_\ell^{-1}(x') \exp(-j \frac{2\pi}{\Lambda} g' x') dx', \quad (\text{B.8})$$

where x' is the direction of the \vec{K} vector of the grating. It is critical to put these coefficients onto the correct positions of the E and A matrices. Also one can improve the computational efficiency by minimizing n_x and n_y (or maximizing f_x and f_y).

REFERENCES

- [1] S. Sinzinger and J. Jahns, *Microoptics*, (Wiley-Vch, New York, 1999).
- [2] T. P. Lee, *Current Trends in Integrated Optoelectronics*, (World Scientific, New Jersey, 1994).
- [3] M. C. Wu, "Micromachining for optical and optoelectronic systems," Proc. of the IEEE **85**, 1833-1856, (1997).
- [4] P. C. Deguzman, *Stacked Subwavelength Gratings for Imaging Polarimetry*, Ph.D. dissertation, (University of Alabama in Huntsville, 2000).
- [5] S. Lin and J. G. Fleming, "Creation of a 3-D silicon photonic crystal," OPN **9**, Dec., 35 (1998).
- [6] A. Chutinan and S. Noda, "Highly confined waveguides and waveguide bends in three-dimensional photonic crystal," Appl. Phys. Lett. **75**, 3739-3741 (1999).
- [7] M. G. Moharam and T. K. Gaylord, "Diffraction analysis of dielectric surface-relief gratings," J. Opt. Soc. Am. **72**, 1385-1392 (1982).
- [8] M. G. Moharam and T. K. Gaylord, "Rigorous coupled-wave analysis of metallic surface-relief gratings," J. Opt. Soc. Am. A **3**, 1780-1787 (1986).
- [9] D. W. Prather, M. S. Mirotznik, and J. N. Mait, "Boundary element method for vector modeling diffractive optical elements," in *Diffractive and Holographic Optics Technology II*, I. Cindrich and S. H. Lee, ed., SPIE **2404**, 28-39 (1995).
- [10] B. Lichtenberg and N. C. Gallagher, "Numerical modeling of diffractive devices using the finite element method," Opt. Eng. **33**, 3518-3526 (1994).
- [11] M. S. Mirotznik, D. W. Prather, J. N. Mait, W. A. Beck, S. Shi, and X. Gao, "Three-dimensional analysis of subwavelength diffractive optical elements with the finite-difference time-domain method," Appl. Opt. **39**, 2871-2880 (2000).
- [12] J. Turunen and F. Wyrowski, *Diffractive Optics for Industrial and Commercial Applications*, (Akademie Verlag, Berlin, 1997).
- [13] K. Yee, "Numerical solution of initial boundary value problems involving Maxwell's equations in isotropic media," IEEE Trans. Antennas Propagat. **AP-14**, 302-307 (1966).
- [14] D. E. Goldberg, *Genetic Algorithm in Search, Optimization, and Machine Learning*, (Addison Wesley, Massachusetts, 1989).
- [15] K. Krishnakumar, "Micro-genetic algorithm for stationary and non-stationary function optimization," SPIE **1196**, 289-296 (1989).

- [16] M.G. Moharam, D. A. Pommet, and E. B. Grann, "Stable implementation of the rigorous coupled-wave analysis for surface relief gratings: enhanced transmittance matrix approach," *J. Opt. Soc. Am. A* **12**, 1077-1086 (1995).
- [17] W. Veldkamp and T. J. McHugh, *Binary Optics*, (Scientific American, New York, 1992).
- [18] A. G. Weber, M. Schell, G. Fischbeck, and D. Bimberg, "Generation of single femtosecond pulses by hybrid model locking of a semiconductor laser," *IEEE J. Quantum Electron.* **28**, 2200-2207, (1992).
- [19] H. I. Smith, "A proposal for maskless, zone-plate-array nanolithography," *J. Vac. Sci. Technol. B* **14**, 4318-4322 (1996).
- [20] R. Kashyap, *Fiber Bragg grating*, (Academic Press, London, 1999).
- [21] D. W. Prather, *Analysis and Synthesis of Finite Aperiodic Diffractive Optical Elements Using Rigorous Electromagnetic Models*, Ph.D. dissertation, (University of Maryland, 1997).
- [22] G. Nordin, J. T. Meier, P. C. Deguzman, and M. Jones, "Diffractive optical element for Stokes vector measurement with a focal plane array," in *Polarization: Measurement, Analysis, and Remote Sensing II*, D. H. Goldstein, D. B. Chenault, Editors, SPIE **3754**, 169-177, (1999).
- [23] M. Born and E. Wolf, *Principles of Optics*, 6th ed., (Pergamon Press, London, 1980).
- [24] J. W. Goodman, *Introduction to Fourier Optics*, (McGraw-Hill Book Company, New York, 1968).
- [25] P. P. Banerjee and T. Poon, *Principles of Applied Optics*, (Aksen Associates, Inc., Boston, 1991).
- [26] E. Lalor, "Conditions for the validity of the angular spectrum of plane waves," *J. Opt. Soc. Am.* **58**, 1235-1237 (1968).
- [27] R. Neureuther and K. Zaki, "Numerical methods for the analysis of scattering from nonplanar and periodic structures," *Alta. Freq.* **38**, 282- 285 (1969).
- [28] N. Neviere, R. Petit, and M. Cadilhac, "About the theory of optical grating coupler-waveguide systems," *Opt. Commun.* **9**, 48-53 (1973).
- [29] R. Petit, *Electromagnetic Theory of Gratings*, (Springer-Verlag, Berlin, 1980).
- [30] D. Maystre, ed., *Selected Papers on Diffraction Gratings*, SPIE **MS83**, (SPIE, Bellingham, 1993).
- [31] M. G. Moharam and T. K. Gaylord, "Rigorous coupled-wave analysis of grating diffraction—E-mode polarization and losses," *J. Opt. Soc. Am.* **73**, 451-455 (1983).
- [32] M. G. Moharam and T. K. Gaylord, "Rigorous coupled-wave analysis of metallic surface-relief gratings," *J. Opt. Soc. Am. A* **3**, 1780-1787 (1986).
- [33] M. G. Moharam, "Coupled-wave analysis of two-dimensional gratings," in *Holographic Optics: Design and Applications*, I. Cindrich, ed., SPIE **883**, 8-11 (1988).

- [34] T. Tamir, H. C. Wang, and A. A. Oliner, "Wave propagation in sinusoidally stratified dielectric media," *IEEE Trans. Microwave Theory Tech.*, **MTT-12**, 323-335 (1964).
- [35] C. B. Burckhardt, "Diffraction of a plane wave at a sinusoidal stratified dielectric grating," *J. Opt. Soc. Am.* **56**, 1502-1509 (1966).
- [36] R. Magnusson and T. K. Gaylord, "Equivalence of multiwave couple-wave theory and modal theory for period-media diffraction," *J. Opt. Soc. Am.* **68**, 1777-1779 (1978).
- [37] J. N. Mait., "Understanding diffractive optic design in the scalar domain," *J. Opt. Soc. Am. A* **12**, 2145-2158 (1995).
- [38] W. T. Vetterling, S. A. Teukolsky, and B. P. Flannery, *Numerical Recipe in C – The Art of Scientific Computing*, (Cambridge University Press, New York, 1992).
- [39] S. Kirkpatrick, C. D. Gelatt, Jr., and M. P. Vecchi, "Optimization by simulated annealing," *Science* **220**, 671-680 (1983).
- [40] J. R. Fienup, "Iterative method applied to image reconstruction and to computer-generated holograms," *Opt. Eng.* **19**, 297-306 (1980).
- [41] H. W. Holloway and R. A. Ferrante, "Computer analysis of holographic systems by means of ray tracing," *Appl. Opt.* **20**, 2081-2084 (1981).
- [42] V. Soifer, V. Kotlyar, and L. Doskolovich, *Iterative Methods for Diffractive Optical Elements Computation*, (Taylor & Francis Press, London, 1997).
- [43] O. Bryngdahl and F. Wyrowski, "Digital holography — computer-generated holograms," in *Progress in Optics XXVIII*, E. Wolf, ed., 1-86 (North-Holland, New York, 1990).
- [44] R. W. Gerchberg and W. O. Saxton, "A practical algorithm for the determination of phase from image and diffraction plane pictures," *Optik*, **35**, 237-246 (1971).
- [45] N. C. Gallagher and B. Liu, "Method for computing kinoforms that reduces image reconstruction error," *Appl. Opt.* **12**, 2328-2335 (1973).
- [46] F. Wyrowski, "Iterative quantization of digital amplitude holograms," *Appl. Opt.* **31**, 2253-2258 (1989).
- [47] F. Wyrowski, "Diffractive optical elements: iterative calculation of quantized, blazed phase structures," *J. Opt. Soc. Am. A* **7**, 961-969 (1990).
- [48] R. Dorsch, A. W. Lohmann, and S. Sinzinger, "Fresnel ping-pong algorithm for two-plane computer-generated hologram display," *Appl. Opt.* **33**, 869-875 (1994).
- [49] S. Mellin, *Design and Analysis of Finite Aperture Diffractive Optical Elements*, Ph.D. dissertation, (University of Alabama in Huntsville, in publication).
- [50] E. G. Johnson, *Design and Analysis of Single and Cascaded Diffractive Optical Elements*, Ph.D. dissertation, (University of Alabama in Huntsville, 1996).
- [51] Z. Zhou and T. J. Drabik, "Optimized binary, phase-only, diffractive optical element with subwavelength features for 1.55 μm ," *J. Opt. Soc. A* **12**, 1104-1112 (1995).

- [52] E. Noponen and Jari Turunen, "Eigenmode method for electromagnetic synthesis of diffractive elements with three-dimensional profiles," *J. Opt. Soc. Am. A* **11**, 2494-2502 (1994).
- [53] W. Prather, J. N. Mait, M. S. Mirotznik, and J. P. Collins, "Vector-based synthesis of finite aperiodic subwavelength diffractive optical elements," *J. Opt. Soc. Am. A* **15**, 1599-1607 (1998).
- [54] D. Chambers, *Stratified Volume Diffractive Optical Elements*, Ph.D. dissertation, (University of Alabama in Huntsville, 2000).
- [55] R. B. Hwang and S. T. Peng, "Performance evaluation of a bigrating as a beam splitter," *App. Opt.* **36**, 2011-2018 (1997).
- [56] G. P. Nordin and P. C. Deguzman, "Broadband form birefringent quarter-wave plate for the mid-Infrared wavelength region," *Optics Express* **5**, 163-168, (1999).
- [57] G. P. Nordin, J. T. Meier, P. C. Deguzman, and M. W. Jones, "Micropolarizer array for infrared imaging polarimetry," *J. Opt. Soc. Am. A* **16**, 1168-1174 (1999).
- [58] M. G. Moharam and T. K. Gaylord, "Three-dimensional vector coupled-wave analysis of planar-grating diffraction," *J. Opt. Soc. Am.* **73**, 1105-1112 (1983).
- [59] S. T. Han, Y. L. Tsao, R. M. Walser, and M. F. Becker, "Electromagnetic scattering of two-dimensional surface-relief dielectric gratings," *App. Opt.* **31**, 2343-2352 (1992).
- [60] R. Brauer and O. Bryngdahl, "Electromagnetic diffraction analysis of two-dimensional gratings," *Opt. Commun.* **100**, 1-5 (1993).
- [61] L. Li, "Formulation and comparison of two recursive matrix algorithms for modeling layered diffraction gratings," *J. Opt. Soc. Am. A* **13**, (1996).
- [62] S. T. Han, Y. L. Tsao, R. M. Walser, and M. F. Becker, "Electromagnetic scattering of two-dimensional surface-relief dielectric gratings," *App. Opt.* **31**, 2343-2352 (1992).
- [63] N. Chateau and J. Hugonin, "Algorithm for the rigorous coupled-wave analysis of grating diffraction," *J. Opt. Soc. Am. A* **11**, 1321-1331 (1994).
- [64] S. Peng and G. M. Morris, "Efficient implementation of rigorous coupled-wave analysis for surface-relief gratings," *J. Opt. Soc. Am. A* **12**, 1087-1096 (1995).
- [65] P. Lalanne, "Improved formulation of the coupled-wave method for two-dimensional gratings," *J. Opt. Soc. Am. A* **14**, 1592-1598 (1997).
- [66] E. Noponen and J. Turunen, "Eigenmode method for electromagnetic synthesis of diffractive elements with three-dimensional profiles," *J. Opt. Soc. Am. A* **11**, 2494-2502 (1994).
- [67] J. J. Greffet, C. Baylard, and P. Versaevel, "Diffraction of electromagnetic waves by crossed gratings: A serious solution," *Opt. Lett.* **17**, 1740-1742 (1992).
- [68] L. Li, "New formulation of the Fourier modal method for crossed surface-relief gratings," *J. Opt. Soc. Am. A* **14**, 2758-2767 (1997).

- [69] K. Hirayama, E. N. Glytsis, T. K. Gaylord, and D. W. Wilson, "Rigorous electromagnetic analysis of diffractive cylindrical lenses," *J. Opt. Soc. Am. A* **13**, 2219-2231 (1996).
- [70] A. Taflove, *Computational Electrodynamics: The Finite-Difference Time-Domain Method*, (Artech House, Massachusetts, 1995).
- [71] A. Taflove, Eds. *Advances in Computational Electrodynamics: The Finite-Difference Time Domain Method*, (Artech House, Massachusetts, 1998).
- [72] D. H. Hochmuth and E. G. Johnson, "Finite Difference Time Domain Analysis of Chirped Dielectric Gratings," Conf. On Binary Optics Huntsville, Alabama, 107-110 (1993).
- [73] J. B. Judkins and R. W. Ziolkowski, "Finite-difference time-domain modeling of nonperfectly conducting metallic thin-film gratings," *J. Opt. Soc. Am. A* **12**, 1974-1983 (1995).
- [74] D. W. Prather and S. Shi, "Formulation and application of finite-difference time-domain method for the analysis of axially-symmetric DOEs," *J. Opt. Soc. Am. A* **16**, 1131-1142 (1999).
- [75] C. A. Balanis, *Advanced Engineering Electromagnetics*, (John Wiley & Sons, New York, 1989).
- [76] A. Bayliss and E. Turkel, "Radiation boundary conditions for wave-like equations," *Comm. Pur Appl. Math.* **23**, 707-725 (1980).
- [77] G. Mur, "Absorbing boundary conditions for the finite-difference approximation of the time-domain electromagnetic field equations," *IEEE Trans. Electromagnetic Compatibility* **23**, 377-382 (1981).
- [78] Z. P. Liao, H. L. Wong, B. P. Yang, and Y. F. Yuan, "A transmitting boundary for transient wave analyses," *Scientia Sincia (series A)*, **XXVII**, 1063-1076, (1984).
- [79] J. P. Berenger, "A perfectly matched layer for the absorption of electromagnetic waves," *J. Comput. Phys.* **114**, 185-200 (1994).
- [80] K. R. Umashankar and A. Taflove, "A novel method to analyze electromagnetic scattering of complex object," *IEEE Trans., Electromagnetic Compatibility* **24**, 397-405 (1982).
- [81] A. Taflove and K. R. Umashanker, "Radar cross section of general three-dimensional structures," *IEEE Trans. Electromagnetic Compatibility* **25**, 433-440 (1983).
- [82] G. S. Smith, *An Introduction to Classical Electromagnetic Radiation*, (Cambridge Univ. Press, New York, 1997).
- [83] J. Turunen, A. Vasara, and J. Westerholm, "Kinform phase relief synthesis: A stochastic method," *Opt. Eng.* **28**, 629-637 (1989).
- [84] B. K. Jennison, J. P. Allebach, and D. W. Sweeney, "Iterative approaches to computer-generated holography," *Opt. Eng.* **28**, 1162-1176 (1989).
- [85] S. Kirkpatrick, C. D. Gelatt, Jr., and M. P. Vecchi, "Optimization by simulated annealing," *Science* **220**, 671-681 (1983).

- [86] E. G. Johnson and M. A. G. Abushagur, "Microgenetic-algorithm optimization method applied to dielectric gratings," *J. Opt. Soc. Am. A* **12**, 1152-1160 (1995).
- [87] D. Brown and A. Kathman, "Multi-element diffractive optical designs," *SPIE* **2404**, 18-27 (1995).
- [88] G. Zhou, Y. Chen, Z. Wang, and H. Song, "Genetic local search algorithm for optimization design of diffractive optical elements," *Appl. Opt.* **38**, 4281-4290 (1999).
- [89] J. H. Holland, *Adaptation in Natural and Artificial System*, (University of Michigan Press, Michigan, 1975).
- [90] K. Krishnakumar, "Micro-genetic algorithm for stationary and non-stationary function optimization," *SPIE* **1196**, 289-296 (1989).
- [91] Z. Michalewicz, *Genetic Algorithm + Data Structures + Evolution Programs*, (Springer-Verlag, Berlin, 1992).
- [92] L. Davis, *Handbook of Genetic Algorithms*, (Van Nostrand Reinhold, New York, 1991).
- [93] M. Mitchell, *An Introduction to Genetic Algorithms*, (The MIT Press, Massachusetts, 1997).
- [94] A. H. Wright, "Genetic algorithms for real parameter optimization," in *Foundations of Genetic Algorithms*, G. Rawlins, Eds., 205-218, (Morgan Kaufmann Publishers, California, 1991).
- [95] K. A. De Jong, *An Analysis of the Behavior of a Class of Genetic Adaptive Systems*, Ph. D. dissertation, (University of Michigan, Michigan, 1975).
- [96] W. Prather, M. S. Mirotznik, and J. N. Mait, "Design of subwavelength diffractive optical elements using a hybrid Finite Element-Boundary Element method," *SPIE* **2689**, 14-23 (1996).
- [97] G. Granet, "Reformulation of the lamellar grating problem through the concept of adaptive spatial resolution," *J. Opt. Soc. Am. A* **16**, 2510-2516 (1999).